Advancing Nanophotonic Devices for Biomolecular Analysis: Force Spectroscopy and Nanopositioning of Single Molecules in Zero-Mode Waveguides

Stephan F. Heucke

Dissertation
an der Fakultät für Physik
der Ludwig-Maximilians-Universität
München

vorgelegt von
Stephan F. Heucke
aus München

München, den 23.04.2013

Erstgutachter:	Prof. Hermann E. Gaub
Zweitgutachter:	Prof. Philip Tinnefeld
Tag der mündlichen Prüfung:	11.06.2013

Abstract

The work presented in this thesis joins two powerful methods of nanobiosciences: Nanophotonic devices with their sensitivity in single-molecule fluorescence techniques, on the one hand, and scanning-probe microscopy with its angstrom-precision and piconewton force-sensitivity, on the other hand. Here, their interplay is investigated and novel combined techniques are developed. In addition, the new findings are already employed in successful studies proving the methodological benefit of the joint techniques to unsolved problems in the nanobiosciences. An outline is given here:

- Mechanisms involving force-activated enzymes are of great biological and medical importance. Unfortunately, the rate dynamics of these enzymes cannot be measured with conventional ensemble techniques, as these enzymes are inactive if there is no mechanical stress. Therefore they require mechanical triggering to be activated. A straightforward and highly desired alternative approach to investigate these enzymes is to apply single molecule force spectroscopy to activate the enzymes and fluorescence correlation spectroscopy to simultaneously quantify the binding dynamics of labeled ligands. However, this concept has not yet been realized, as conventional, diffraction limited optics forbid single-molecule resolution at the high ligand concentrations necessary. In the course of this thesis, a new methodology is developed to solve this problem: Nanophotonic devices called zero-mode waveguides (ZMWs) are combined with atomic force microscopy (AFM) based force spectroscopy to raise the ligand concentration limit by three orders of magnitude. In a proof-of-principle study, autoinhibited titin kinase is force-activated at the bottom of a zero-mode waveguide while a possible binding event of fluorescently labeled adenosine triphosphate is optically monitored.

- Metal-based photonic devices used for single-molecule fluorescence detection, like such ZMWs, have already found important applications (e.g. in genome sequencing) but usually suffer from strong signal inhomogeneities. This is due to metal-induced fluorescence quenching and enhancement which typically occur within wavelength distance from the metal. Thus they cannot easily be analyzed with conventional optics. In this work, the recently developed single-molecule cut-and-paste technique is combined with live optical superresolution microscopy to non-invasively probe the electrodynamic environment of such metallic nanostructures with the precision of an AFM: Single fluorescent dyes are anchored in ZMWs with a spatial accuracy better than 20 nm. By comparing their fluorescence lifetimes and intensities with those of single stochastically immobilized dyes the electrodynamic environment of ZMWs is characterized as strongly heterogeneous, and their very center is identified as prominent hotspot. This proofs the benefit of the newly developed technique as it can also be used to load ZMWs with single enzymes, thus resulting in single occupation as well as homogeneous and enhanced signal intensities.

- In a preceding study, the optical properties of switchable metamaterials are investigated using shear-force based THz-near-field microscopy. These structures are artificially designed to have specific optical properties and are applicable for biomolecular assays. The presented results refute the previous explanation of a secondary mode in the metamaterial and, instead, reveal the underlying of unexpected collective oscillations. At the same time, high local field concentrations are mapped. The whereabouts of these hotspots are of great interest for potential metamaterial-based bioassays.

In particular, the realization of a nanometer-precise robotic arm able to load nanoscopic observation chambers with single biomolecules for advanced optical analysis demonstrates the striking abilities and perspectives of combining scanning-probe microscopy and nanophotonic devices.

Zusammenfassung

Nanophotonische Bauelemente mit ihrer extrem hohen Sensitivität in Einzelmolekül-Fluoreszenzmessungen und Rasterkraftmikroskopie mit ihrer Angström-Positionsgenauigkeit und Piconewton-Kraftauflösung gehören zu den leistungsstärksten Methoden der Nanobiowissenschaften. In der vorliegenden Arbeit werden diese Techniken zusammengeführt. Dies resultiert einem präziseren Verständnis der nanophotonischen Elemente und erlaubt darauf aufbauend neue kombinierte Techniken zu entwickeln. Der Nutzen dieser Techniken bei der Lösung offener Fragen in den Nanobiowissenschaften wird in den durchgeführten Studien verdeutlicht. Ein kurzer Überblick über die zahlreichen Ergebnisse der Arbeit wird im Folgenden gegeben:

- Kraftaktivierte Enzyme und die mit ihnen verbundenen Mechanismen sind in der Biologie und Medizin von großer Bedeutung. Leider können ihre Enzymdynamiken jedoch nicht mit konventionellen Ensembletechniken untersucht werden, weil diese Enzyme ohne mechanische Belastung inaktiv sind und zur Aktivierung eine mechanische Kraft benötigen. Eine naheliegende Untersuchungsmethode, die auf diese Probleme eingeht, ist die Kombination aus Aktivierung mittels Einzelmolekül-Kraftspektroskopie und gleichzeitiger Quantisierung der Bindungsdynamiken fluoreszenzmarkierter Liganden mit Hilfe von Fluoreszenzkorrelationsspektroskopie. Dieses Konzept konnte jedoch bisher nicht realisiert werden, da bei den benötigten Ligandenkonzentrationen eine Einzelmolekülauflösung mit konventioneller, beugungsbegrenzter Optik nicht möglich ist. In dieser Arbeit wird eine neue Methode entwickelt, die dieses Problem löst: Durch die Kombination von nanophotonischen Bauelemente, genannt *Zero-Mode Waveguides* (ZMW), mit AFM-basierter Kraftspektroskopie wird die obige Konzentrationsobergrenze der Liganden um drei Größenordnungen angehoben. In einer Studie zum Nachweis des Wirkungsprinzips konnten erstmals autoinhibierte Titinkinase-Enzyme am Boden von ZMWs kraftaktiviert und gleichzeitig ein wahrscheinliches Bindungsereignis von markiertem Adenosintriphosphat optisch detektiert werden.

- Photonische Bauelemente aus Metall, wie diese ZMWs, die in der Einzelmolekül-Fluoreszenzdetektion eingesetzt werden, haben bereits wichtige technische Anwendungen gefunden (z. B. in der Gensequenzierung). Eine ihrer grundsätzlichen Schwächen ist jedoch die breite Signalstärkeverteilung. Diese wird auf metallinduzierte Fluoreszenzschwächung bzw. –erhöhung zurückgeführt. Weil diese Effekte hauptsächlich im Bereich einer Wellenlänge von den Metallstrukturen entfernt auftreten, konnten sie bisher nicht mit konventionellen optischen Verfahren untersucht werden. Daher wird hier die erst kürzlich entwickelte Single-Molecule Cut-and-Paste Technik mit Superauflösungsmikroskopie kombiniert, um die elektrodynamische Umgebung solcher metallischer Nanostrukturen nicht-invasiv mit der Präzision des AFM zu sondieren: Einzelne Farbstoffe werden hierfür mit einer Genauigkeit von mehr als 20 nm in ZMWs verankert. Durch den Vergleich ihrer Fluoreszenzlebensdauern und Signalstärken mit denen stochastisch verteilter Farbstoffe konnte das elektrodynamische Umfeld in ZMWs charakterisiert und deren Zentrum als sogenannter *Hotspot* identifiziert werden. Der Nutzen der entwickelten Technik geht weit über die Charakterisierung hinaus, da sie auch angewandt werden kann, um einzelne Enzyme in den *Hotspots* abzusetzen und dabei homogene Signalverteilungen mit optimalem Signal/Rauschen zu erreichen.

- In einer vorangestellten Studie werden die optischen Eigenschaften eines Metamaterials mit Hilfe von Terahertz-Nahfeldmikroskopie untersucht. Diese

Materialien mit künstlichen optischen Eigenschaften finden auch Anwendung in biomolekularen Nachweisverfahren. Die gewonnenen Messergebnisse widerlegen die bisherige Interpretation einer sekundären Schwingungsmode und weisen stattdessen auf unerwartete kollektive Schwingungen hin. Gleichzeitig zeigt die gemessene Verteilung der lokalen Feldkonzentrationen sogenannte *Hotspots* auf, die für mögliche Anwendung von Metamaterialien wichtig sind.

Insbesondere die Realisierung eines nanometergenauen Roboterarms, der nanoskopische Observationskammern mit einzelnen Biomolekülen bestücken kann, um verbesserte optische Analyseverfahren durchzuführen, zeigt eine Vielzahl von Möglichkeiten und Aussichten auf, die sich durch die Kombination von Rasterkraftmikroskopie und nanophotonischen Bauelementen ergeben.

Contents

1 Introduction

Throughout the history of natural science, a prominent frontier is constantly found at the small end of things: Human interest in nature basically started at the meter scale with our muscles and eyes as sensitive tools for analysis and manipulation. This frontier soon moved towards the millimeter and upper microscale where the invention of lenses and fine mechanical instruments raised questions and could be used to deliver answers. In the past century, the microscale was eventually “conquered” by scientists which resulted in and was assisted by, the digital revolution. In the following, computer-based techniques such as electron-beam, atomic force or single-molecule fluorescence microscopy could be optimized and pushed this frontier to where it is today: the nanometer scale. This, can today be seen, regardless of the particular field, in the number of journals, sub-journals and publications decorated with the term “nano”.

Nanobiosciences and their Impact

Bioscience at the nanoscale, here referred to as "nanobiosciences", has evolved as an especially interesting field within the nanosciences - particularly for physicists:

Here, physicists have the opportunity to investigate the interesting physics of e.g. force-activated biomolecules [1], self assembling DNA [2] or proteins' course of motion [3]. At the same time, they can use their findings and developed techniques in bottom-up approaches to draw conclusions reaching far into biology. The main challenge for any researcher, however, is the fact that such studies demand not only a deep understanding of physics but also a broad knowledge and understanding of recent findings in chemistry and biology as well as close interdisciplinary collaborations with colleagues in these fields.

Despite these challenges, the nanobiosciences have already helped to develop novel materials such as spider silk [4, 5], medically promising drug delivery methods [6], or biomolecular analysis tools [7, 8].

One particular interesting application of nanobiotechnology is the realization of fast and accurate whole genome sequencing. Here, two of the three dominating technological approaches [9] are based on nanobiotechnology, one using biological nanopores [10] and the other employing nanophotonic devices called zero-mode waveguides (ZMW, see Figure 1) [11]. The third approach is based on CMOS-technology [12] and is likely to be eventually downscaled to nanometer dimensions in order to increase its packing density.

The capability to read whole genomes quickly, has strong potential impact in epidemics. In a 2010 cholera outbreak in the post-earthquake Haiti, the geographic origin of the responsible strain was investigated by using ZMW-based sequencing [13]. In May 2011, the same technology could characterize the enteroaggregative E. coli strain that caused a severe diarrhea outbreak in Germany [14]. In both cases, sequencing of the pathogenic

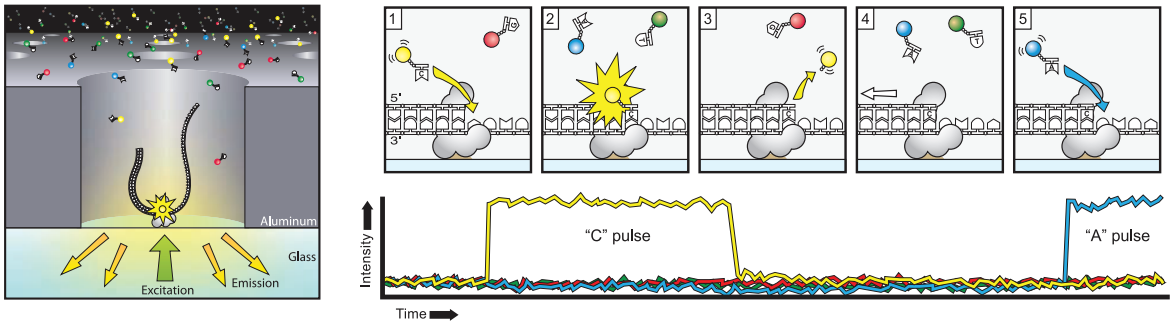

Figure 1 Nanophotonic devices allow fast and cheap sequencing of whole genomes: A polymerase immobilized at the bottom of a zero-mode waveguide is observed in a fluorescence microscope. As the polymerase synthesizes a DNA copy, it incorporates fluorescently labeled nucleotides. Each type of nucleotide (adenosine, cytidine, guanosine and thymidine) is labeled with a different color, so the detected color sequence over time represents the underlying DNA base sequence. Zero-mode waveguides are necessary to form the small observation volume necessary to resolve single incorporation events despite the high concentration of fluorophores. Reprinted with permission from ref. [11]. Copyright 2009 AAAS.

agents did not lead to any direct measures because large pathogen genome libraries allowing their identification are lacking as of today. The US Food and Drug Administration is currently using ZMW-based sequencing in its "100k Pathogen Genome Project" to build a public access data base with the genomes of a hundred thousand of the most lethal pathogens responsible for food-born illnesses [15]. Such libraries will accelerate the medical response upon sequencing based pathogen-identification and help to reduce significantly the medical and economic risks of epidemics.

These third generation whole genome sequencing methods, made possible by the latest findings in nanobiosciences and -technology, are not just fast but also commercially accessible at low costs. This will, in the near future, lead to a routine genome sequencing of human individuals [9] e.g. for diagnosis purposes in hospitals. The capability to compare one's individual genome with data banks as developed by the currently running Personal Genome Project [16], which also includes information on phenotype and medical profiles, probably will have the utmost social impact related to nanobiosciences [17].

Scientific Scope of this Thesis

Despite these scientific insights and technological outcomes, there are still many open questions in the nanobiosciences.

As described in the opening paragraph of this introduction, a symbiosis of novel scientific findings and technological advances always has been a strong driving force in scientific progress. This is true also in the nanobiosciences where, for example, the green fluorescent protein is both a result of biomolecular research as well as an important label in single-molecule fluorescence microscopy which, again is used for biomolecular research. As another example, the above mentioned ZMWs first were an object of studies on extraordinary transmission [18] before they were used as nanophotonic devices for DNA-sequencing [11]. As a final example, nanotechnology allowing the fabrication of nanoscopic cantilever tips and the precise positioning of piezoelectric crystals has enabled the measuring of biomolecular forces between e.g. ligands and receptors [19].

These examples also represent three of the most important research tools in nanobiosciences: single-molecule fluorescence, nanophotonic devices and atomic force

microscopy (AFM). On basis of the hypothesis that research in the nanobiosciences will most strongly profit from the development and optimization of its research techniques, this leads to the scientific question of this thesis:

How can the use of nanophotonic devices be advanced for biomolecular analysis in fundamental research?

Nanophotonic devices include e.g. near-field scanning optical microscopy (NSOM) tips [20], gold nanoparticles [21], localized surface plasmon resonance based biosensors [22] or the above mentioned zero-mode waveguides. As to these examples, ZMW-technology stands out as its development has been, boosted by the race for a billion dollar sequencing market, but at the same time the relatively elaborate ZMW fabrication and handling has limited their use beyond sequencing. So, fundamental research is likely to profit from this fast development of ZMWs - if they can be advanced in their use.

With this background, the above question will be focused on the possibilities of combining an atomic force microscope with zero-mode waveguides. It will be investigated how AFM and its ability to serve as molecular tweezers, like in the recently developed method of single-molecule cut-and-paste (SMC&P) [23], can be employed to improve ZMWs in their application for massively parallel optical assays (see Figure 2 for conceptual schematics). In an approach from the opposite direction, the question will be answered how ZMWs can enable previously impossible AFM-based force spectroscopy of enzymes in combination with simultaneous fluorescence correlation spectroscopy of single ligands binding under natural conditions. So far, only commercial imaging AFMs have been used as tool to probe, for example, the surface functionalization in ZMWs [24]. So, the compatibility of an AFM's potential to probe biomolecules or to position molecules in ZMWs is not a priori clear and will be characterized hereunder.

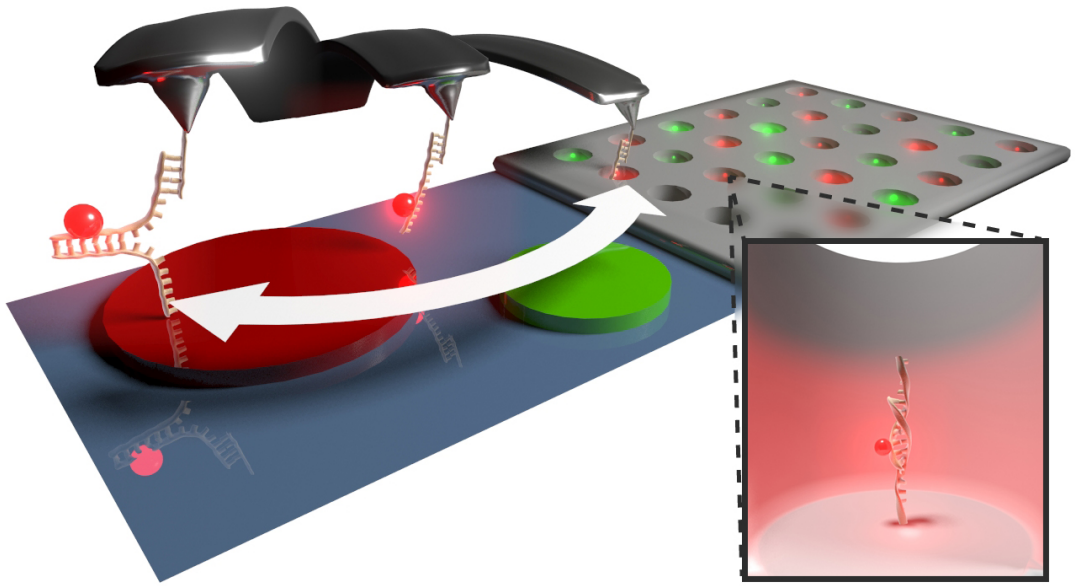

Figure 2 Schematics of single-molecule cut-and-paste in zero-mode waveguides: One concept of this thesis employs an AFM cantilever to place single-molecules in the center of zero-mode waveguides. Here, short strands of fluorescently labeled DNA are "picked up" in macroscopic depot areas and positioned in the nanometric apertures. The strands can be used for anchoring enzymes or for probing the local electrodynamic environment in waveguides. Image by C. Hohmann, Nanosystems Initiative Munich (NIM).

In a preliminary study, this thesis will also investigate the mode structure of THz-metamaterials using shear-force based THz near-field microscopy. Metamaterials are not primarily biophotonic nanostructures but planar or three-dimensional arrays of microscopic split-ring resonators designed to have artificial optical properties. However, their applicability for biophotonic assays has been shown and the results presented here hold to a great extent also for nanoscopic metamaterials. Especially with the ability to design their optical response, metamaterials might have great prospect as biophotonic devices and so the ability to map the whereabouts of their hot-spots could play a key-role in the future.

Structural Overview

As this is a cumulative thesis with three individual manuscripts as its core content, the thesis' structure is chosen accordingly: First, the theoretical and experimental background of this thesis, single-molecule fluorescence, zero-mode waveguides and metamaterials, will be reviewed. In the main part of this thesis the findings are presented in three chapters, each featuring one research article. In the beginning of each article chapter, a paragraph builds a bridge to the overall framework of the thesis, explains the motivation of the specific study and emphasizes how the presented article is put into context. Then, the respective article is briefly summarized and reprinted. The third manuscript in this thesis is printed together with its supplementary information, as it includes protocols and descriptions of novel methods. Due to this compact structure, the presentation of results and their discussion is left to the articles thus redundancies from additional individual discussions. Finally, in the closing chapter of this thesis, conclusions and outlooks are made for all articles with respect to the scientific question of this thesis.

2 Theoretical and Experimental Background

2.1 Single-Molecule Fluorescence

The advantage of bottom-up research approaches lie in the simplicity of their systems. In single-molecule fluorescence experiments this principle is taken to its extreme. Here, the recorded signal stems from single fluorescent molecules whose individual unsynchronized behaviors are observed. This reveals insights that would otherwise be hidden in ensemble experiments.

Principles of Fluorescence

Fluorescence and phosphorescence represent the two kinds of photoluminescence which is defined as the emission of a photon by a substance as a result of the previous absorption of a photon.

The mechanisms of photoluminescence are best described with the help of a Jablonski diagram (see Figure 3) [25, 26]. It depicts the photophysics of a fluorescent molecule in a three-electronic-state model: Following the absorption of a photon, the molecule is excited from its ground state S_0 into a vibrational level of its first excited singlet-state S_1. After rapid, non-radiative conversion to the lowest vibrational level of S_1, molecule specific rates determine whether the fluorophore undergoes fluorescent, phosphorescent or even non-radiative relaxation back to S_0.

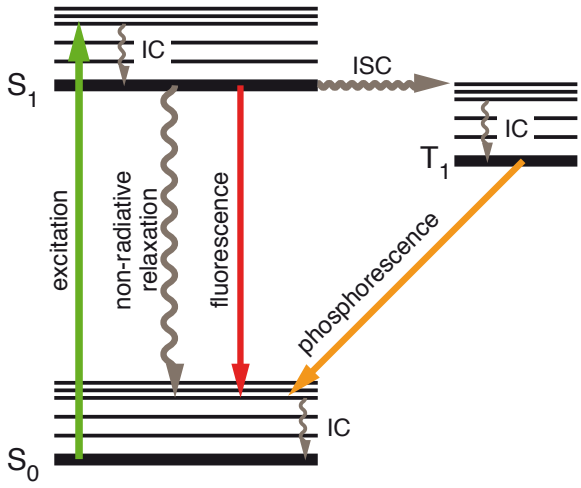

Figure 3 Jablonski diagram: The electronic states and conversion rates of a fluorescent molecule are shown in a simplified model (IC: internal conversion, ISC: inter-system crossing, T_1: first excited triplet-state).

In the framework of this thesis, the two important fluorescence parameters are the fluorophore's quantum yield Q and its fluorescence lifetime τ:

$$Q = \frac{\Gamma_r}{\Gamma_r + \Gamma_{nonr}} \quad (1)$$

$$\tau = \frac{1}{\Gamma_r + \Gamma_{nonr}} \quad (2)$$

Here, Γ_r is the rate of all deexcitation processes involving the emission of a photon (fluorescence and phosphorescence) and Γ_{nonr} is the rate of all non-radiative deexcitation processes. Note that in this terminology fluorescence, phosphorescence and non-radiative decays all contribute equally to the fluorescence lifetime.

Although these rates primarily depend on the choice of fluorescent dye, they can be influenced by external factors. Non-radiative energy transfer in collisions with molecular oxygen, for example, will increase Γ_{nonr} [26]. As this process leads to a decrease in quantum yield and an overall decrease of fluorescence intensity, it is considered a quenching process. On the other hand, processes increasing the fluorescence intensity are called enhancement processes. One of these occurs in the presence of reducing and oxidizing agents that depopulate the long-lasting triplet-state [27].

The redshift occurring in fluorescence allows the spectral filtering of excitation and emission light. This basic principle brings about the high signal-to-noise ratios (S/N) needed to resolve single molecules. Additionally, high excitation intensities can increase the S/N even further, but this is set to a limit by fluorescence photobleaching. Photobleaching is a stochastic process in which the excited dye undergoes irreversible chemical alterations and permanently stops fluorescing.

Single-molecule fluorescence techniques typically stand out by their minimal invasiveness, real-time observation and applicability in vivo as well as in vitro. They allow the investigation of e.g. enzyme dynamics [28], ribosomal catalysis of RNA [29] or protein folding [30].

2.2 Zero-Mode Waveguides

Zero-mode waveguides are the main nanophotonic devices investigated for biological application in this thesis. They were introduced by Levene et al. in a 2002 issue of Science [31]. In the same issue the article was highlighted as it reports „a method that enables the single-molecule detection of even weaker, transient interactions between proteins, between proteins and nucleic acids, and between enzymes and substrates. By circumventing the diffraction limit of light [it] can detect individual molecules at much higher (micromolar) concentrations than previously possible“ [32].

In this chapter the fundamentals of ZMWs and their most prominent applications are introduced with regards to the findings of this thesis. A broader review on ZMWs is found in ref. [33].

Basic Principle of ZMWs

The principle mechanism of ZMWs is relatively straightforward: An optically dense metal film, evaporated onto a glass cover slip, is perforated with nanoscopic cylindrical holes. Since these holes have diameters below a wavelength-dependent cut-off value, no propagating light modes can exist inside the holes that could allow transmission of light – hence their name: zero-mode waveguides. Thus, when illuminated with monochromatic laser light through the glass cover slip, the metal cladding with the ZMWs reflects all incident light and the upper hemisphere of the metal film remains in the dark. However, due to the wave-like character of electromagnetic fields, the incident light does not abruptly reflect at the glass-hole-interface but penetrates several nanometers into the nanohole as evanescent field [31].

Now, since the waveguide and the upper hemisphere of the whole sample can be filled with buffer medium, the ZMW is accessible for diffusing molecules and the evanescent field at the bottom can be used as observation volume for fluorescence correlation spectroscopy (FCS, for a review see ref. [34]). For one ZMW excitation and observation is usually realized in confocal microscopy configuration [35], however, if several ZMWs are to be observed in parallel epi-illumination [36], multiple-confocal [37] or total internal reflection fluorescence (TIRF) excitation are possible. In all cases, fluorescence emission form the ZMW is collected through the same objective used for excitation (see Figure 4).

The observation volume at the bottom of the ZMW is at the order of zeptoliters, and therefore, three orders of magnitude smaller than a diffraction limited laser focus. It is also smaller than all non-diffraction-limited FCS alternatives as e.g. TIRF-FCS [38], NSOM [39] or stimulated-emission-depletion (STED) [40] (see Figure 4). Thus ZMWs allow FCS at previously inaccessible label concentrations. For biological FCS applications, high label concentrations are especially important as many biomolecular interactions occur with relatively low affinities. This is emphasized by the distribution of all Michaelis-Menten values in the BRENDA enzyme database (see Figure 5).

With a perfect conductor as cladding material, the cut-off diameter d_c is given by

$$d_c = 0.586\lambda_M \qquad (3)$$

where λ_M is the wavelength of the incident light in the medium of the material filling the

ZMW (usually aqueous buffer) [31]. In analogy, λ_c is defined as the cut-off wavelength: For a given aperture diameter incident light with a wavelength longer than λ_c will decay within the waveguide. In real metals, however, surface plasmon effects and the skin depth of the metal result in a continuous transition between the propagating and evanescent regimes [41].

One important issue arising in ZMW experiments arises from the way how the molecule of interest, typically an enzyme, is immobilized in the aperture. This is done by a pull-down of molecules diffusing in the buffer and by subsequent washing of unbound molecules. With this method, the number of molecules per aperture and their position within the waveguide is governed by statistics.

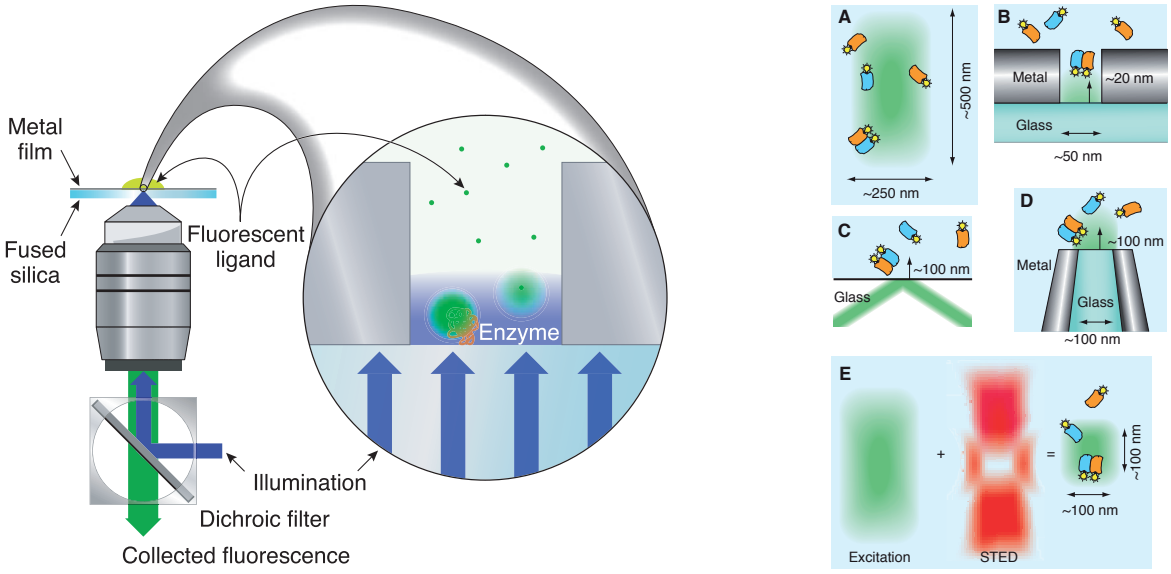

Figure 4 Zero-mode waveguide setup in comparison to other techniques: Left: Used as sample in a conventional fluorescence microscope, a ZMW separates the bulk of fluorescently labeled ligands from the excitation light. Only at the ZMW's bottom a small observation volume is created. Fluorescence from ligands interacting with enzymes here, is then collected. Right: The observation volume in ZMWs is smaller than that of any other non-diffraction limited technique such as e.g. C) TRIF-FCS, D) NSOM or E) STED. Reprinted with permission from ref. [31] and [32]. Copyright AAAS 2003.

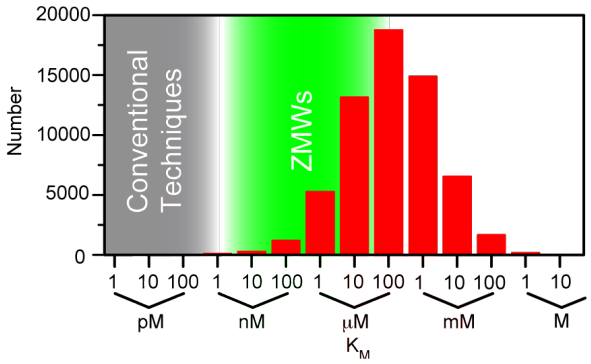

Figure 5 Complete statistics of Michaelis-Menten values in the BRENDA enzyme data base: Histogram of Michaelis-Menten constants (KM) for 62,000 enzymes taken from the Brenda Database (http://www.brenda-enzymes.info). It emphasizes how conventional fluorescence techniques fail to observe single-enzyme kinetics at natural concentrations of labeled substrates. The use of zero-mode waveguides, however, allows experiments at label concentrations up to 100 μM. Reprinted with permission from ref. [42]. Copyright 2013 Inderscience.

Fluorescence Properties in ZMWs

A molecule's fluorescence properties can be strongly altered not only by interactions with other molecules (see chapter 2.1) but also by the presence of metal [26]. Here, two major processes are involved: First, the excitation rate can be strongly increased through local field enhancements and thus leading to an overall enhancement of fluorescence intensity [43]. Secondly, non-radiative energy transfer to the metal can increase Γ_{nonr} and thus decrease the quantum yield and quench the fluorophores intensity [44].

Metallic enhancement and quenching has been extensively studied, experimentally and theoretically, for the classic scenario of a fluorophore in front of a planar metallic surface where the distance between metal and fluorophore dominates their interaction [44-49]. More recently, fluorescence of dyes close to metallic nanoparticles has received marked attention [43, 50, 51]. Here, the size, the material and the shape of the nanoparticle govern its optical response and thus its influence on fluorophores. It was shown that careful engineering of the fluorophore-particle interaction can achieve fluorescence enhancements of almost two orders of magnitude [21].

For actual ZMWs, the metallic influence on fluorophores has been well studied by FCS [52, 53]. Here, reduced fluorescence lifetimes and an overall fluorescence enhancement were reported. But because these FCS measurements recorded the fluorescence intensity and lifetime of diffusing fluorophores, they represent spatial ensemble measurement and do not give any information on local differences of fluorescence properties in ZMWs.

Such local differences, however, are of great interest for most ZMW applications, since fluorescence signals usually stem from labels temporarily binding to an enzyme that is immobilized at a fixed position.

Fabrication of ZMWs

There are three main methods for ZMW fabrication:

Using a focused ion-beam (FIB), ZMW can be milled directly into blanks consisting of glass cover slips with the metal film already evaporated on them [52]. This method requires the least number of equipments and fabrication steps. However, the Gaussian shape of the focused-ion-beam does not allow to mill steep sidewalls and, at the same time, avoid milling into the glass substrate. So FIB-milled ZMWs generally extend a couple of nanometers into the glass and their shape and depth is not very reproducible. Obviously this also results in an increase in observation volume and in a variation of the electrodynamic properties, which are expected to be closely related to the geometry of the ZMW. Whereas for some ZMW applications these disadvantages are acceptable for basic research, where comparable ZMW geometries are a minimal prerequisite, the FIB fabrication method is not applicable. Additional negative effects such as increased corrosion and altered chemical properties stemming from FIB remains in the ZMWs are discussed in publication P2.

Compared to FIB-milling, the second method employing reactive-ion-etching and nanolithography is more elaborate: Blanks as described above, are coated with a positive tone photoresist which is perforated with circular holes by electron beam exposure and by consecutive development. Finally, reactive ion etching selectively and anisotropically etches away the aluminum through the resist holes, and waveguides remain after the resist has been dissolved. For details, see ref. [24, 31, 54].

The latest fabrication method was introduced by Foquet et al. in 2008 [55]. The basic steps of the process are depicted in Figure 6: First, e-beam lithography with a negative tone photoresist is used to pattern resist pillars on a previously cleaned glass cover slip. Next, the glass cover slip and the pillars are evaporated with the metal film. Finally the metal caps on top of the pillars are broken off in an ultrasonic solvent bath and the underlying resist is dissolved, leaving behind the ZMWs. This method uses the pillars as a shadow mask, so - implying a conical shape of the pillar with decreasing widths towards its base (see Figure 6) – the apertures will have nearly vertical sidewalls and an unaltered glass bottom.

In the proof-of-principle force spectroscopy experiments presented in chapter 4 FIB-milled ZMWs were used, as the observation volume's exact size and shape was not essential here. Their detailed fabrication is described in the associated publication P2. For the spectroscopic investigation in chapter 5, however, ZMWs of reproducible quality and with a cylindrical profile were necessary to allow comparison of different size ZMWs and with experimental results from other studies. Here, ZMWs made with negative e-beam lithography were used. A detailed protocol of their fabrication is found in the supplement of publication P3. This recipe had to be established in the framework of this thesis, as the photoresist used in the one and only previously published procedure was not available from the manufacturer anymore.

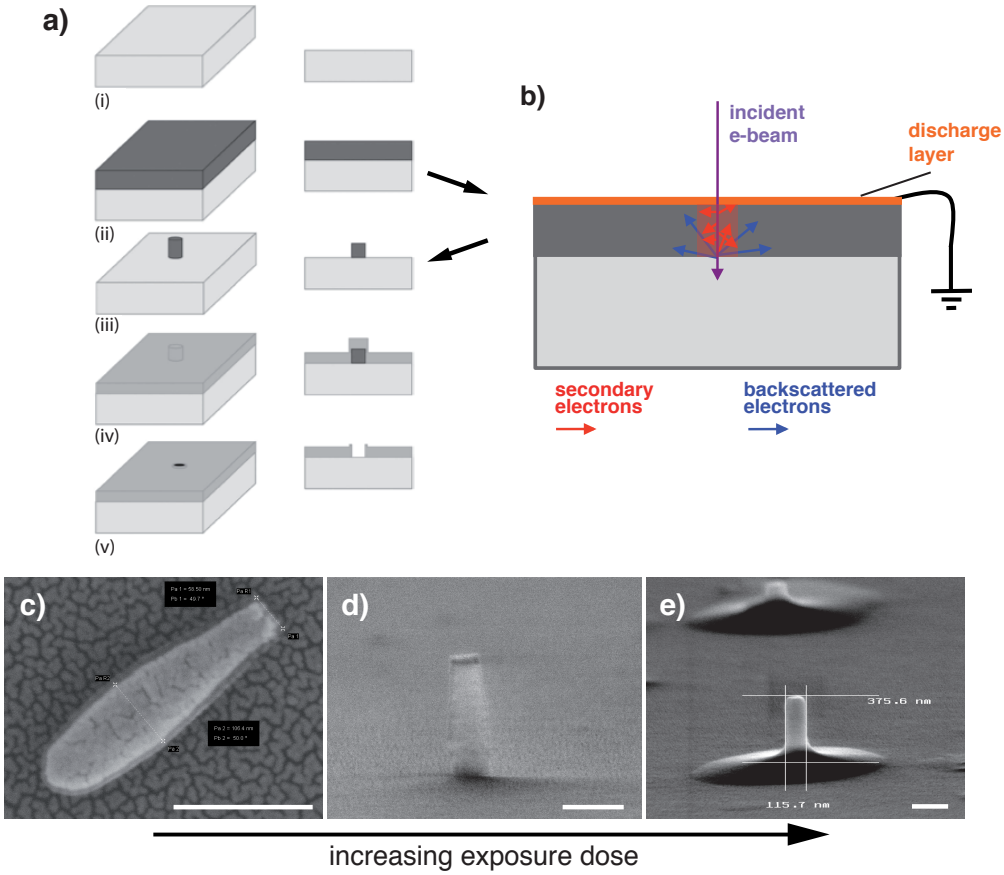

Figure 6: E-beam lithography of ZMWs: a) A sample in the making is depicted after the major fabrication steps: (i) cleaning of the glass substrate, (ii) photoresist coating, (iii) exposure, post-exposure bake and development, (iv) metal evaporation, (v) ultrasonic lift-off. **b)** The resist is exposed by primary electrons of the incident e-beam as well as backscattered and secondary electrons. **c) - e)** Electron microscopy images of ZMW-precursor pillars (white bar is 200 nm). Only the correct dose and post-exposure bake temperature will result in steady pillars with straight edges as in d). For details of the fabrication process see SI of publication P3. a) Was reprinted with permission from ref. [55]. Copyright American Institute of Physics 2008.

It is worth mentioning here, that most parameters and sometimes even whole steps of a lithography recipe are specific to a certain resist. This is especially true using the e-beam exposure which requires one additional sensitive step not considered in standard lithography: The substrate for ZMWs is non-conducting glass instead of semi-conducting silicon. So, an additional conductive discharge layer is required to avoid a local built-up of charges from e-beam exposure leading to a distortion of the written lithography pattern. This layer consists of a thin metal film evaporated onto the resist right before exposure. Unfortunately, most photoresists are also sensitive to the heat radiation during metal evaporation, but a pre-exposure cross-linking of the resist is to be avoided. Whereas a 10 nm gold film is used in the original recipe, the evaporation of gold, aluminum and chromium unacceptably altered the photoresist used in this thesis only evaporation of silver, which has a lower evaporation temperature, showed no negative effects.

Functionalization of ZMWs

As previously discussed, a restriction of possible anchor points to the center of the ZMWs is favorable for spectroscopic reasons but has not yet been reported in the literature. However, in order to restrict binding to the glass bottom and to reduce metal-ligand interactions, the metal cladding including the apertures' sidewalls can be passivated by polyvinylphosphonic-acid (PVPA). The binding of this polymer is chemically selective as it forms permanent covalent bonds with aluminum oxide surfaces but hydrolyzes from silicon-oxide surfaces such as glass [56]. A detailed protocol of the passivation process is found in ref. [56] and the supplement of publication P3.

To specifically immobilize proteins to the glass bottom via avidin-binding, biotinylated bovine serum albumin (BSA) has been employed [57]. Alternatively, biotinylated polyethylene glycol (PEG) can be covalently attached to the glass surface via silane chemistry [56].

To pattern the depot and target sites for SMC&P in ZMWs, a surface-functionalization was established, which combines PVPA-passivation and PEG-biotin immobilization with a microfluidic system or the application of a micros spotter. The detailed protocols for both methods are found in the supplement of publication P3. They include only minimal use of chloride containing buffers, as chloride ions are known to promote corrosion (see [56] and publication P2.)

SMRT Genome Sequencing

The fast and highly parallel read out, together with their relatively easy handling, makes ZMWs an ideal tool for commercialized nanophotonic devices. This obviously was already clear to Levene et al in 2002, as they showed in their principal paper that incorporation of single bases is observable with ZMWs, thus hinting towards the billion dollar DNA sequencing market. In fact, already two years later, in 2004, some of the co-authors founded a company which, today, is one of the leading companies in DNA-sequencing, i.e. Pacific Biosciences [9].

This short introduction of their primary technology of SMRT-sequencing, however, should not just be seen as mere historical or economical side note within this thesis. Much more it shows how a highly funded R&D department can become the driving force in fundamental research as it led to improved fabrication [55], passivation and functionalization of ZMWs [56]:

SMRT sequencing stands for single-molecule real-time sequencing [11]. It optically detects the incorporation of labeled nucleotides during the DNA synthesis from template-strands by a polymerase fixed at the ZMWs bottom (see Figure 1). As the four different nucleotides are labeled with different color dyes the spectral signatures of the photon burst during incorporation indirectly reveal the sequence of the DNA-template in a prism based read-out configuration [37]. Due to the small observation volume in ZMWs, the bases can be presented in micromolar concentrations without loosing single-molecule resolution. Because for most polymerases the equilibrium dissociation constants of nucleotides are in the high (micromolar) regime, these concentrations not only allow fast polymerase synthesis speeds and data acquisition rates but they also reduce malfunctions of the polymerase [31, 58].

The relatively long read lengths of SMRT sequencing together with its unique epigenetic sequencing abilities [59] are the advantages over other techniques. However, SMRT sequencing has not unfolded its whole potential. As can be seen in the supplementary movie of ref. [11], only a fraction of the ZMWs in a sample produce readable sequencing data. This is most likely due to Poissonian limited single-occupation of the waveguides [56].

ZMWs in Fundamental Research

Although ZMWs have not yet become the golden standard in fundamental research, the existing studies are proof for ZMWs' wide range of applications and their high impact potential beyond DNA-sequencing:

ZMWs were employed to optically investigate the kinetics of oligomerizing repressor proteins [60] as well for a study on protein-protein interaction dynamics [57]. Also, supported lipid bilayers were formed in ZMWs, thus opening the possibility to study membrane imbedded receptors and proteins at physiological concentrations [36]. A year later, Moran-Mirabal et al. succeeded to invaginate the plasma membrane of living cells into ZMWs and to measure the diffusion of different labels incorporated therein [61]. In a final example of employing ZMWs, the translation dynamics of single ribosomes could be optically resolved at codon resolution thus allowing the investigation of mechanism and regulation of translation [62].

2.3 Metamaterials

Veselago was the first to theoretically investigate the interesting optical properties of materials with simultaneous negative permittivity and permeability, the so called negative index media [63]. He proposed that light propagation in these media is very counterintuitive but does not violate the laws of physics: According to Maxwell's equations, electric field $\vec{E}$, magnetic field $\vec{B}$ and wave vector $\vec{k}$ form a "left-handed" set of vectors in these negative index media, as opposed to the natural "right-handed" orientation. For an electromagnetic wave this means that the direction of the phase velocity points "backwards", i.e. in the opposite direction of energy flux given by the pointing vector (see Figure 7).

Veselago already pointed out that this allows interesting applications. The unnatural refraction behavior (away and not towards the normal) of light incident on negative index material, for example, allows the fabrication of lenses with totally new but useful properties. However, his studies were purely hypothetical, as negative index materials do not occur in nature (see Figure 7). This topic lost attention for another 30 years until, in 1999 Pendry suggested to fabricate negative index media from "artificial atoms" consisting of conductive subwavelength sized loops and wires [64]. Following this approach, Smith et al. experimentally realized the first negative index material called metamaterial, only one year later [65, 66].

Basic Principle of Metamaterials

The basic principle of negative index metamaterials is relatively straight forward and best explained with the pioneering structure introduced by Pendry and Smith (for detailed reviews see [67, 68]):

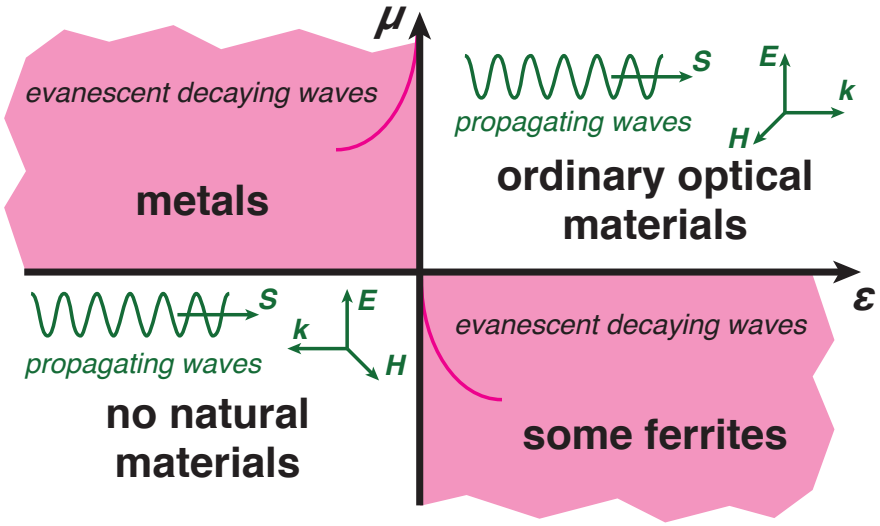

Figure 7 Classifying materials by their electric and magnetic properties: While materials with negative permittivity ε occur in nature, a negative permeability μ is rare and materials with simultaneously negative ε and μ do not exist at all. While waves decay evanescently in materials of the pink quadrants, propagating waves are allowed in materials which experience permittivity ε and permeability μ of the same sign. Note, that E, H and k form a left-handed vector system for simultaneous negative ε and μ. Adapted from ref. [68].

It consists of a periodic three-dimensional cubic lattice whose unit cells are thin metallic split ring resonators (SRR). As the unit cells have only a low filling fraction of opaque metal and their dimensions are chosen to be much smaller than the wavelength of an incident light, the material's optical properties are that of an “effective medium”. So they are governed by the structural response of the unit cells rather than by their material composition.

Now, this structural response is dominated by the SRRs whose inductance and capacitance are designed to result in a strong magnetic resonance just below the frequency of the incident light for which the negative index is desired. According to the Drude-Lorentz model for light-matter interaction, the permeability will go to negative values for a small frequency band at the high-frequency side of the resonance [67, 69]. Given a strong enough resonance, this negative permeability from the SRRs will dominate the effective permeability of the metamaterial’s response at these frequencies slightly above the resonance.

To achieve a negative refractive index, thin metallic wires are spun on the backside of the SRRs. These wires are designed to be independent from the SRRs and exhibit a purely plasmon resonance [70] at a lower near-by frequency. A careful design of both kinds of resonators thus results in two overlapping bands of negative effective permittivity and negative permeability (see Figure 8).

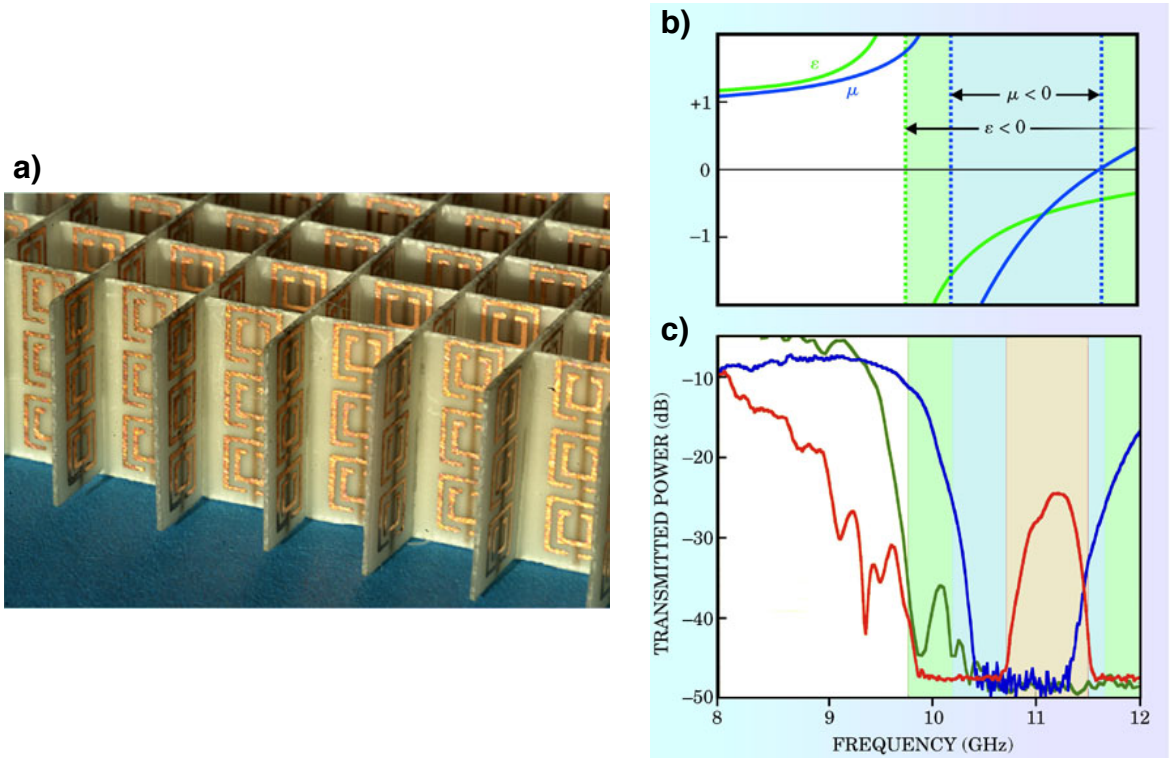

Figure 8 Principle of metamaterials: a) A metamaterial array operating in the microwave regime. Its unit cells consist of a double split-ring resonator with a wire spun behind. **b)** The purely electric resonance of the wire and the purely magnetic resonance of the split-rings result in regions with negative ε and μ, respectively (green and blue bars). **c)** The predicted transmitted power spectrum of a metamaterial consisting solely from bars (green), split-rings (blue) or the combined structure (red) shows transmission for simultaneously negative ε and μ in the latter case only. Reprinted with permission from ref. [67]. Copyright American Institute of Physics 2003.

Whereas the term metamaterial was originally introduced by Smith et al. [65] for artificial negative index media, its use expanded to include a multitude of artificial design structures which are tailored to exhibit specific optical properties. However, their relative size remains a characteristic boundary of metamaterials: Only with unit cells smaller than the Bragg limit (half the wavelength), a material will exhibit effective medium properties, thus being considered as metamaterial. Artificial optical materials greater than the Bragg limit are called photonic crystals.

Important metamaterial subcategories are magnetic metamaterials which exhibit only a negative permeability [71], electric metamaterials which exhibit a purely dielectric negative response [72], and chiral metamaterials exhibiting circular dichroism [73, 74].

Metamaterial Applications

The strongest driving force in metamaterial research has been the goal of realizing a "superlense" from negative index material, that would allow resolution beyond the diffraction limit [63, 75]. Although there have been successful experimental approaches to beat the diffraction limit with a metamaterial [76, 77], a breakthrough for visible frequencies has not yet been achieved.

Probably the second most promising metamaterial application is cloaking. This concept uses metamaterials to guide light around an object in such a way that presence of neither the object nor the metamaterial is visible in the far field [78, 79].

In a different approach, Chen et al. developed a switchable metamaterial that is used as amplitude modulator in the THz gap [80] – a bandwidth where optical devices are rare, as many common materials do not respond in this frequency range. The switchable metamaterial is fabricated on a GaAs substrate and consists of metallic split ring resonators (SRRs) with one split-gap capacitance and two inductive loops whose magnetic field components cancel out in the far-field. The SRRs are electrically connected and form a Schottky contact with the electron gas of an n-doped layer in the GaAs. Only with an applied bias, the depletion zone of the Schottky contact widens enough to stop a short-circuiting of the capacitance. Without an applied bias the metamaterial will have no response.

Liquid-phase metamaterials called "metafluids" offer the tailoring of optical properties in fluids. This possibility was opened up in a collaboration with the Liedl group at Ludwig-Maximilians-Universität Munich. They fabricated a metamaterial made from DNA-origami and gold nanoparticles [73] tailored to show circular dichroism. With this, the study also revolutionized metamaterial fabrication as they made use of DNA self-assembly. Especially for nanometer length scale metamaterials required for the visible regime, DNA self-assembly is a very convenient technique compared to e.g. elaborate 3D nanolithography or focused ion-beam milling [81].

Most important in the scope of this thesis, metamaterials are promising photonic devices for bioassays, as well: Their strong resonance response allows the detection of small changes in the local dielectric environment – induced by e.g. small amounts of protein. Lee at al showed this by detecting biotin binding to the SRRs of a metamaterial through a significant shift in resonance frequency [82]. Biophotonic assays based on resonance shifts have brought a great impact in laboratories in form of surface plasmon resonance biosensors [7]. Their benefits are: Quick and high-sensitivity signal response, label-free detection and small sample quantity requirements. Metamaterial based bioassays

have the potential to compete with these properties and additionally allow a tailored design of operating wavelength.

3 Coupled Oscillations in Terahertz Metamaterials

In most cases, small regions with high electric field concentrations, called hot-spots, play a superior role in nanophotonic devices, as these regions usually generate the strongest signals. Thus, knowing the local field distributions is essential for optimized designs of biophotonic assays.

Metamaterials used as biophotonic devices for the label-free detection of small amounts of protein were introduced in chapter 2.3. As the modes in metamaterials are usually resolved only in finite element simulations, experimentally probing the electrodynamic distributions within the metamaterial structure unambiguously locate their hot-spots. This knowledge can then be used to increase performance and applicability of metamaterial-based bioassays.

The publication presented in this chapter describes how the mode structure of a switchable microscale metamaterial is investigated by using THz near-field microscopy. It is shown that a mode formerly denoted to a “Mie resonance” in fact results from a collective oscillation with a resonance which is governed by the periodicity of resonators rather than by the properties of the resonators themselves. This effect was initially interpreted as surface plasmon resonance. But subsequent experiments refute this interpretation – at least in the classic picture of the surface plasmon. Consequently, the question of the physical origin of this mode remains open.

It should be kept in mind that, due to the scalability of Maxwell’s equations, the findings presented here, hold to a great extent also for nanoscale metamaterials which operate in the important visible regime, but which are much harder to fabricate and to probe locally.

3.1 Summary of Associated Publication P1

The switchable, purely electric metamaterial investigated here, was introduced in ref. [80] and chapter 2.3. It has two resonances in far-field transmission spectra: one at 0.7 THz which was identified as fundamental LC-resonance of the SRRs, and a second resonance at 1.6 THz which, so far, has been denoted to a Mie-type mode in the SRRs' side arms [71, 80].

In publication P1, a single SRRs of the metamaterial is imaged with 1 μm resolution using THz near-field microscopy [83, 84]. The signal in this technique is proportional to the capacitive coupling of THz near-field between a scanning probe and the underlying material [83]. Here, however, the metamaterial's short-circuiting Schottky bias is modulated during the scan and the differential signal is recorded. Thus, only a coupling to the structure's modulated response - the metamaterial's resonances - gives contrast, while coupling related to simple material properties of the metallic structure cancel out. In additional experiments, transmission spectra of metamaterials with varying periodicity are simulated and measured in experiment.

The results show, spatially and spectrally, that both resonances are excited at the capacitor. Regarding the transmission spectra of different array periodicities, a shift of the secondary resonance is observed while the fundamental resonance remains constant.

Both results are not surprising for the fundamental resonance that has been described as purely LC-dependant, and whose mode's maximum amplitude of charge density oscillation at the split gap is expected to result in the strongest capacitive coupling. However, these results strongly disagree with the Mie-mode interpretation of the second resonance. In this picture, a maximum coupling at the side arm endings would be expected, where we detected no significant coupling. Instead, we found a clear spectral response of this resonance at the capacitor. Also, a charge oscillation in the side arms would exclusively depend on their length but not on array periodicity.

The findings in publication P1 let us conclude that the second resonance is neither a Mie-type resonance nor a second harmonic oscillation [85], as the latter would not shift independently from its fundamental resonance. Instead, the dependence on the unit cell distance of the metamaterial arrays hints towards an in-plane coupling and thus to collective oscillations being the underlying mechanism. As periodicity and permittivity of the substrate are matching the excitation conditions for a surface plasmon resonance, this is proposed in publication P1 as underlying physical mechanism.

3.2 Associated Publication P1

Surface Plasmons in terahertz metamaterials

by

Guillermo Acuna, Stephan F. Heucke, Florian Kuchler, Hou-Tong Chen, Antoinette J. Taylor and Roland Kersting

published in

Optics Express, 16 (23): 18745–18751, 2008
DOI: 10.1364/OE.16.018745

Surface plasmons in terahertz metamaterials

G. Acuna[1], S. F. Heucke[1], F. Kuchler[1], H.-T. Chen[2], A. J. Taylor[2], and R. Kersting[1]

[1]*Photonics and Optoelectronics Group & Center for NanoScience, University of Munich, 80799 Munich, Germany*

[2]*Los Alamos National Laboratory, MPA-CINT, MS K771, Los Alamos, New Mexico 87545, USA*

guillermo.acuna@physik.uni-muenchen.de

http://www.thz.physik.uni-muenchen.de

Abstract: We characterize terahertz metamaterials by applying aperture-less near-field microscopy with a bandwidth that covers the entire spectral response of the structures. The observations agree with the interpretation of the fundamental mode of the metamaterial. But the high frequency resonance shows properties that deviate from the common interpretation. We show that the high frequency response is governed by surface plasmon excitations, which have a comparable oscillator strength as the fundamental mode.

OCIS codes: (180.4243) Near-field microscopy; (300.6495) Spectroscopy, terahertz; (160.3918) Metamaterials

References and links

1. J. Pendry and D. R. Smith, "Reversing light with negative refraction," Phys. Today **57**, 37-43 (2004).
2. V. M. Shalaev, "Optical negative-index metamaterials," Nat. Photonics **1**, 41-48 (2007).
3. J. B. Pendry, A. J. Holden, D. J. Robbins, and W. Stewart, "Magnetism from conductors and enhanced nonlinear phenomena," IEEE Trans. Microwave Theory Tech. **47**, 2075-2084 (1999).
4. G. Mie, "Beiträge zur Optik trüber Medien, speziell kolloidaler Metallösungen," Ann. Phys. **25**, 377-445 (1908).
5. C. Enkrich, M. Wegener, S. Linden, S. Burger, L. Zschiedrich, F. Schmidt, J. F. Zhou, T. Koschny, and C. M. Soukoulis, "Magnetic metamaterials at telecommunication and visible frequencies," Phys. Rev. Lett. **95**, 203901 (2005).
6. H. Raether, *Surface plasmons on smooth and rough surfaces and on gratings* (Springer tracts in modern physics, 1998).
7. E. Shamonina and L. Solymar, "Magneto-inductive waves supported by metamaterial elements: components for a one-dimensional waveguide," J. Phys. D **37**, 362-367 (2004).
8. H. Liu, D. A. Genov, D. M. Wu, Y. M. Liu, J. M. Steele, C. Sun, S. N. Zhu, and X. Zhang, "Magnetic plasmon propagation along a chain of connected subwavelength resonators at infrared frequencies," Phys. Rev. Lett. **97**, 243902 (5 pages) (2006).
9. H.-T. Chen, W. J. Padilla, J. M. O. Zide, A. C. Gossard, A. J. Taylor, and R. D. Averitt, "Active terahertz metamaterial devices," Nature (London) **444**, 597-600 (2006).
10. T. Zentgraf, J. Dorfmüller, C. Rockstuhl, C. E. R. Vogelsang, K. Kern, T. Pertsch, F. Lederer, and H. Giessen, "Amplitude- and phase-resolved optical near fields of split-ring-resonator-based metamaterials," Opt. Lett. **33**, 848-850 (2008).
11. H.-T. Chen, R. Kersting, and G. C. Cho, "Terahertz imaging with nanometer resolution," Appl. Phys. Lett **83**, 3009-3012 (2003).
12. F. Buersgens, G. Acuna, C. H. Lang, S. I. Potrebic, S. Manus, and R. Kersting, "Shear force control for a THz near field microscope," Rev. Sci. Instrum. **78**, 113701 (2007).

#101635 - $15.00 USD Received 16 Sep 2008; revised 23 Oct 2008; accepted 23 Oct 2008; published 29 Oct 2008

13. H.-T. Chen, S. Kraatz, G. C. Cho, and R. Kersting, "Identification of a resonant imaging process in apertureless near-field microscopy," Phys. Rev. Lett. **93**, 267401 (2004).
14. M. Abashin, U. Levy, K. Ikeda, and Y. Fainman, "Effects produced by metal-coated near-field probes on the performance of silicon waveguides and resonators," Opt. Lett. **32**, 2602-2604 (2007).
15. G. Acuna, F. Buersgens, C. H. Lang, M. Handloser, A. Guggenmos and R. Kersting, "Interdigitated terahertz emitters," Elec. Lett. **44**, 229-231 (2008).
16. W. J. Padilla, A. J. Taylor, C. Highstrete, M. Lee, and R. D. Averitt, "Dynamical electric and magnetic metamaterial response at terahertz frequencies," Phys. Rev. Lett. **96**, 107401 (2006).
17. R. Singh, E. Smirnova, A. J. Taylor, J. F. O'Hara, and W. Zhang, "Optically thin terahertz metamaterials," Opt. Express **16**, 6537-6543 (2008).
18. A. K. Azad, A. J. Taylor, E. Smirnova, and J. F. O'Hara, "Characterization and analysis of terahertz metamaterials based on rectangular split-ring resonators," Appl. Phys. Lett. **92**, 011119 (2008).

1. Introduction

Metamaterials offer outstanding opportunities for designing the electromagnetic properties of matter [1, 2]. Their response to light is determined by the structure embossed into the material rather than by its composition. The most common approach for tailoring electrical and magnetic properties of the metamaterials is to design metallic resonators and arrange them in periodic patterns [3]. Obviously, the unit cells of such patterns have to be smaller than the light's wavelength if a spatially homogeneous response in the far-field is desired. The primary resonances of both, the dielectric permittivity and the magnetic susceptibility are determined by the geometric properties of the elements within the unit cells. Examples are *LC*-resonances of circuits comprising inductances and capacitances or Mie resonances within the individual microscopic elements [4, 5]. Besides these modes the periodicity of the structures itself may lead to further excitations with distinct resonances. Periodic patterns are known to support collective excitations such as dielectric plasmon polaritons [6] and magneto plasmon polaritons [7, 8]. These collective excitations can reach oscillator strengths, which are comparable to that of the elements within the unit cell. In this work we identify the modes of metamaterials using THz microscopy with extreme subwavelength resolution. Our experimental data show, that one mode, which is commonly attributed to a Mie resonance, in fact results from surface plasmon excitations. It is assumed that surface plasmon resonances are a generic property of virtually all metamaterials, because the only requirement for the excitation of these surface waves is the periodicity of the metal structure.

2. Method

The experiments were performed on metamaterials that allow for switching the dielectric resonances by electronic means [9]. The schematic in Fig. 1(a) shows a typical structure and summarizes the most important dimensions. The array of electric split-ring resonators is fabricated on a GaAs substrate with a 1 μm thick n-doped epitaxial layer. Further details of the structure can be found in Ref. [9]. Electronic control over the optical properties is achieved by switching the width of the depletion zone underneath the surface of the structure. The metallic structure forms a Schottky contact to the electron gas in the GaAs as shown in Fig. 1(b). Without applied bias, mobile electrons are close to the metallic structure, and short-circuit the element's central capacitor. When a positive bias is applied, the increased depletion width prevents short-circuiting and the structure reveals a resonance given by the capacitances and inductances of the loops. Far-field transmission data show two resonances when the polarization of the exciting field is oriented as illustrated in Fig. 1(c). The resonance $f_A = 0.7$ THz is due to the fundamental mode, which oscillates between the terminals of the capacitor (mode α in the inset of Fig 1(c)). The resonance $f_B = 1.6$ THz agrees with numerical calculations of a Mie-type mode at the side of the element (mode β in Fig. 1(c)). In the following, we show that the resonance

#101635 - $15.00 USD Received 16 Sep 2008; revised 23 Oct 2008; accepted 23 Oct 2008; published 29 Oct 2008

at this frequency in fact results from the collective excitation of the elements. The oscillator strength of this collective mode exceeds that of the Mie resonance and dominates the spectral response in this frequency range.

The advance of near-field microscopy makes it possible to resolve the modes along the elements of a metamaterial [10]. In this study, we apply apertureless terahertz near-field microscopy with a spatial resolution of about 1 μm [11]. Further details of our technique and the electro-optic detection can be found in [12]. Figure 2(a) illustrates the microscope head. The incident THz pulses are concentrated by the tungsten probe to a spot size of about 1 μm underneath the tip. This spot size is comparable to the lateral resolution of the microscope. It should be emphasized that the image contrast in apertureless THz microscopy is proportional to the capacitive coupling of the near-field into the structure underneath [13]. Thus, the spot size also defines the area where the metamaterial is locally excited by the near-field. This differs from apertureless techniques operated in the near infrared and visible, where non-metallic probes pick up field energy and emit it into the far-field [10, 14]. One outstanding strength of apertureless THz microscopy is its band width. With our recently developed THz emitter [15], it extends over more than 2 octaves from 0.5 THz to about 2.5 THz and covers the entire response spectrum of the metamaterials investigated. This property allows for the spectral characterization of the local response, which is the main merit of this work.

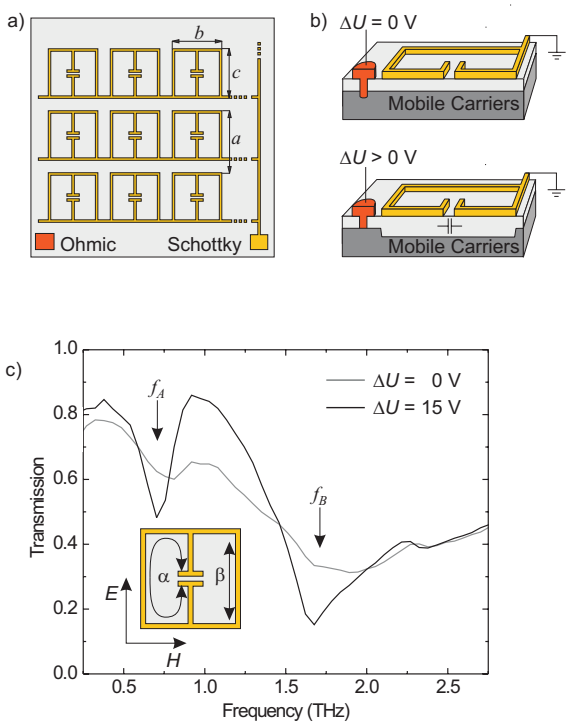

Fig. 1. (a) Top view onto the metamaterial, which consists of a metallic structure fabricated on n-doped GaAs, with $a = 50$ μm and $b = c = 36$ μm. (b) Cross section through the device. Application of a bias between ohmic contact and Schottky contact enlarges the depletion zone, which prevents short-circuiting of the capacitor. (c) Far-field transmission spectra for two different biases. The inset illustrates the polarization of the incident light and two possible modes within one element.

#101635 - $15.00 USD Received 16 Sep 2008; revised 23 Oct 2008; accepted 23 Oct 2008; published 29 Oct 2008

3. Results

Figure 2(b) shows the THz image of one element. All details of the metallic structure are resolved with an image contrast of about 3%. Further insight into the spatial distribution of modes is obtained by differential THz imaging. The differential signal is recorded while the metamaterial is electronically switched between the on- and off-state. This image shows an enhanced contrast close to the central capacitor, while other regions of the device show no measurable signal. We interpret the data in terms of the capacitive coupling between scanning probe and structure. The capacitive coupling is most efficient at the anti-nodes of the resonator, which are located at the capacitor. Here, the fundamental mode α is excited. Following this interpretation, the excitation of mode β should be visible at the edges of the structure. In contrast, no significant signal is recorded here, as Fig. 2(c) shows. From this unexpected fact we conclude that the Mie-type mode β has an oscillator strength, which is much smaller than that of the fundamental mode α. Apparently, the strong resonance at f_B (see Fig. 1(c)) results from another mechanism, which couples much more efficiently to radiation.

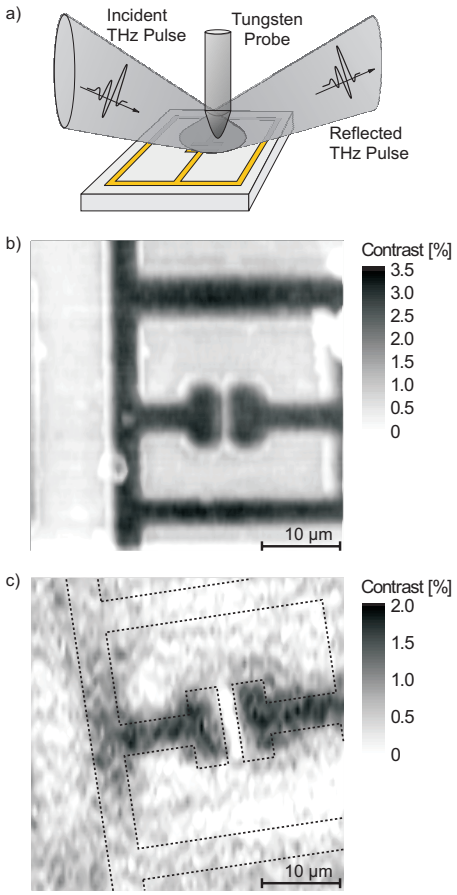

Fig. 2. (a) Schematic of the apertureless THz microscope. The tungsten probe concentrates the incident radiation to the area underneath the tip. (b) Terahertz near-field image of one unit cell. The lateral resolution is about 1 μm. (c) Differential image obtained by switching the structure on and off. The dotted lines illustrate the position of the element.

#101635 - $15.00 USD Received 16 Sep 2008; revised 23 Oct 2008; accepted 23 Oct 2008; published 29 Oct 2008

In the following, we will show that the resonance at $f_B = 1.6$ THz results from the collective response of the entire metamaterial. The extreme bandwidth of apertureless THz microscopy allows for recording the entire spectral response at distinct positions of the structure, as shown in Fig. 3. At position 1 the response of the fundamental mode at 0.7 THz should be strongest while the response of the Mie mode at 1.6 THz is expected to appear at position 2. However, this is not observed. No measurable response is observed at position 2, which confirms that the Mie-mode β has a smaller oscillator strength than the fundamental mode α. In fact, both resonances are found at position 1, which makes a reinterpretation of the resonance at 1.6 THz necessary.

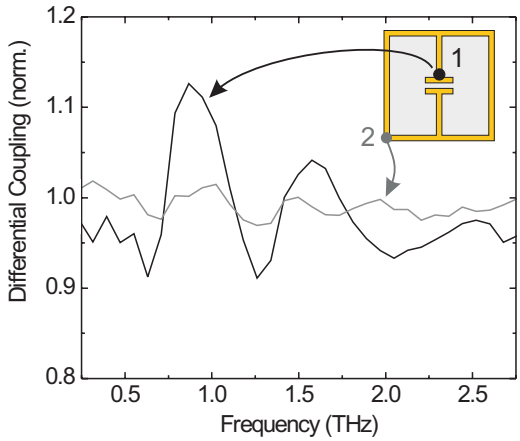

Fig. 3. Spectrally resolved coupling of the near-field to the metamaterial. The spectra were obtained at two different positions of the metamaterial.

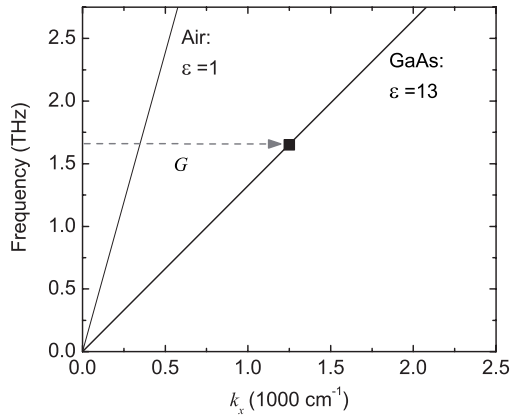

Fig. 4. Dispersion relation for surface plasmon excitations propagating on a metal/air interface and on a metal/GaAs interface. Coupling between light and surface plasmons is possible at 1.6 THz, when an inverse lattice vector $G = \frac{2\pi}{a}$ is gained from the grating.

#101635 - $15.00 USD Received 16 Sep 2008; revised 23 Oct 2008; accepted 23 Oct 2008; published 29 Oct 2008

4. Discussion

The resonance at 1.6 THz results from the excitation of surface plasmons along the surface of the structure. Figure 4 illustrates the surface plasmon dispersion, which can be approximated for the THz range by $\omega = kc/\sqrt{\varepsilon}$, where c is the speed of light. At perpendicular incidence, the THz radiation has a wave vector component in the surface plane of $k_x \approx 0$, which prevents direct excitation of the surface plasmons. The incident radiation can gain the required wave vector from the inverse lattice vector $G = 2\pi/a$ of the metamaterial, where $a = 50$ μm is the metamaterial's period. This Bragg-type scattering leads to a surface plasmon excitation that propagates parallel to the surface in the GaAs substrate. Considering the permittivity of GaAs ($\varepsilon = 13$) leads to a resonance at 1.6 THz in agreement with the data shown in Figs. 1(c) and 3. We have performed further measurements and finite-element numerical simulations of metamaterials with 50 μm and 60 μm periodicity. The results shown in Fig. 5 reveal that the frequency of the second resonance depends on the periodicity which agrees well with the interpretation of surface plasmon excitations.

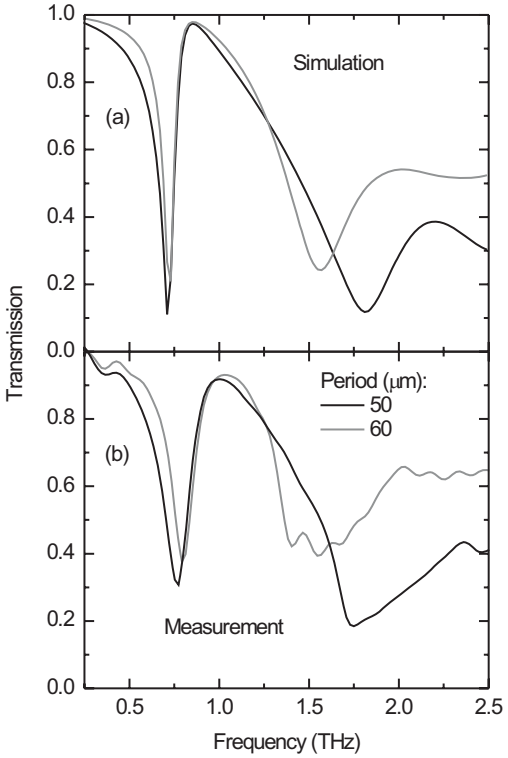

Fig. 5. (a) Simulated and (b) measured far-field transmission spectra for two different periodicities, 50 μm and 60 μm. The samples were fabricated on intrinsic Si.

The experimental data of Fig. 1(c) show that the surface plasmon resonance can be switched by electronic means. A detailed description of the modulation of the central capacitor can be found in [9]. But in contrast to such individual components of the structure, surface plasmons are delocalized excitations. Thus, the switching of the surface plasmon resonance cannot be assigned to a specific element or sub-circuit of the structure. It requires a discussion in reciprocal

#101635 - $15.00 USD Received 16 Sep 2008; revised 23 Oct 2008; accepted 23 Oct 2008; published 29 Oct 2008

space rather than in the original lattice. The electro-modulation of any periodic lattice property leads to a modulation at wave vector $G = 2\pi/a$ in reciprocal space. At this inverse lattice vector the surface plasmon couples to light. This modulation of Fourier components in reciprocal space suffices for electromodulating the surface plasmon. In the micrographs (Fig. 2) and in the spectral measurements in Fig. 3 the surface plasmon resonance has an enhanced visibility in the region of the capacitor because here the electrical field energy is stored every half cycle.

Finally, it should be mentioned that the framework of surface plasmons in metamaterials agrees with resonances reported in other works [16, 17, 18]. The fact that these works cover a variety of metamaterial structures emphasizes the generic role of surface plasmons in THz metamaterials.

5. Conclusions

In summary, we have shown that plasmonic resonances significantly affect the optical properties of metamaterials. The strength of plasmonic resonances can exceed that of Mie resonances within the unit cell. The finding suggests that future design and interpretation of metamaterials should consider collective excitations.

Acknowledgments

This work is partially supported by the Nanosystems Initiative Munich (NIM), the International Doctorate Program Nano-Bio-Technology (IDK-NBT) of the Elite Network of Bavaria, and by the Deutsche Forschungsgemeinschaft (DFG), contract KE516/1-1. H.T.C and A.J.T acknowledge support from the Los Alamos National Laboratory LDRD Program and the Center for Integrated Nanotechnologies, a U.S. Department of Energy, Office of Basic Energy Sciences Nanoscale Science Research Center operated jointly by Los Alamos and Sandia National Laboratories. The authors acknowledge technical support by F. Buersgens, W. H. Nitsche, and S. Schloegl, and material growth by J. M. O. Zide and A. C. Gossard at UCSB.

#101635 - $15.00 USD Received 16 Sep 2008; revised 23 Oct 2008; accepted 23 Oct 2008; published 29 Oct 2008

3.3 Subsequent Experiments

In the following of publication P1, subsequent experiments were conducted to fully characterize the second resonance and to investigate how it fits into surface plasmon theory:

The periodicity dependence of the resonance shift was measured by further far-field transmission spectroscopy experiments as the ones described in publication P1 (see Figure 9ab). Here, intrinsic silicon was used as substrate because a bare silicon chip without metamaterial structures was used as reference spectrum and thus, switching the metamaterials was not needed.

Figure 9d shows spectra of samples with square periodicities varying between 50 and 200 µm. Both resonances show a clear dynamic: While the fundamental resonance shifts

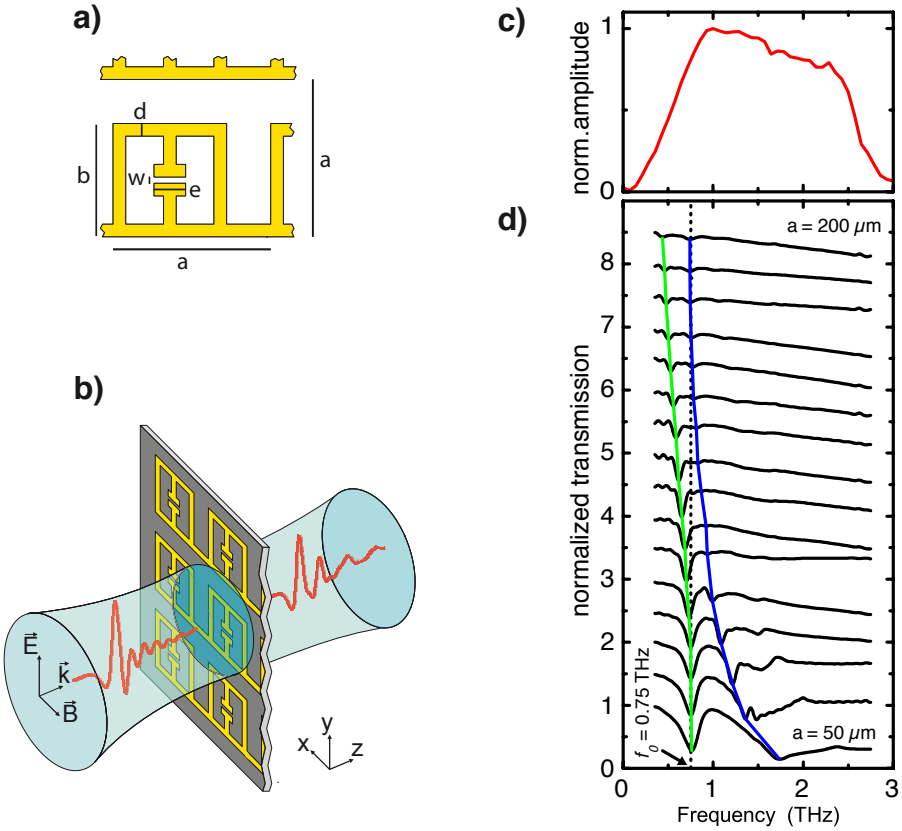

Figure 9: Experimental design and results from transmission spectroscopy: a) Geometry and dimensions of the metamaterial structures: w = 2 µm, e = 10 µm, d = 4 µm and b = 36 µm. The periodicity a of the metamaterial samples is varied. The gold structures were fabricated on intrinsic silicon. **b)** Schematic of the experimental setup: Few-cycle THz pulses hit the metamaterial sample at normal incidence. The polarization of the E-field is parallel to the capacitive arms of the metamaterials. The wavelength limited width of the THz focus is approximately 1 mm allowing illumination of numerous sub-wavelength structures. The transmitted pulses are then detected. **c)** Spectrum of the probing THz radiation. **d)** Transmission spectra of metamaterials with periodicities varying from 200µm to 50µm in steps of 10µm. The green and blue lines mark LC-resonances and secondary resonances, respectively. The original (for a = 50 µm) LC-resonance f_0 is marked with a dotted line. Drawings a) and b) were kindly provided by S. Schloegl.

nonlinearly towards lower frequencies with increasing periodicity *a*, the second resonance approaches the original (for a = 50 µm) LC-resonance asymptotically. These shifts are depicted more clearly in Figure 10a. Here, the resonances are plotted against the wavevector k_{xy} which the incident radiation gains when it is diffracted by the metamaterial array into the xy-plane:

$$k_{xy} = 2\pi/a \qquad (4)$$

The original LC-resonance and the dispersion of non-interacting light in matter

$$k_{light} = \omega\sqrt{\varepsilon_b}/c \qquad (5)$$

are drawn in black, for orientation. Here, *c* is the speed of light and $\varepsilon_b = 11.7$ is the background permittivity in silicon at THz frequencies [87].

The polariton-like anticrossing behavior of the two resonances at f_0 is a fundamental behavior of light-matter interaction [69], thus not allowing new conclusions on the origin of the resonances. However, the asymptotic approach of the resonances to the linear dispersion of light in bulk silicon (black light line) is both characteristic and revealing as the abscissae of the resonances are the in-plane lattice vectors of the metamaterial arrays. This means that the second resonance occurs exclusively wherever it matches – in *k-ω-space* - incident light that was diffracted by the metamaterial array in either x- or y-direction. This exclusive excitation by in-plane radiation implies that the oscillations underlying the second resonance also have an in-plane momentum, so that several oscillators have to be coupled as was concluded in publication P1.

To find out the directionality of the oscillation we varied x- and y- periodicities separately. Figure 10b shows exemplary results: Whereas a variation of the y- periodicity did not spectrally shift the resonances at all, the transmission spectrum of a metamaterial array with shorter x- periodicity is differing drastically from its y- analog but matching the spectrum of its x-analog (see bottom spectrum in Figure 9d) relatively well. As the

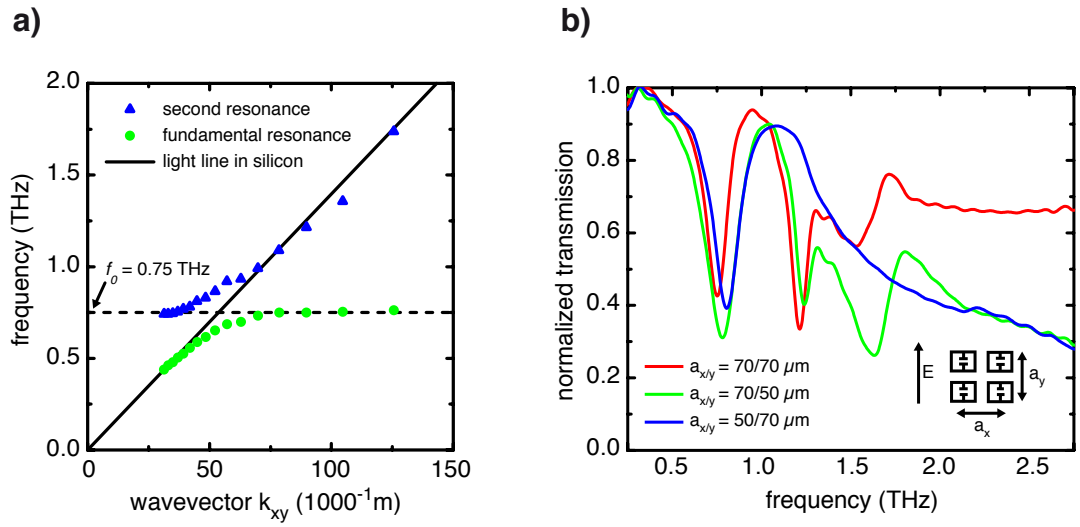

Figure 10 Dispersion relation and orientation of the resonances: a) Resonance frequencies are plotted against the wave vector which the incident radiation gains from the periodicity of the metamaterials: $k_{xy} = 2\pi/a$. The silicon light line is shown in black, and the dotted line marks the fundamental LC-resonance f_0. **b)** An independent variation of the x- and y-periodicity shows strong resonance shifts only in the case of a variation in the horizontal (x) variation.

$\vec{E}$-field of incident light was always polarized in y-direction, these results show that the collective oscillations are driven by p-polarized ($\vec{E}$) light with an in-plane momentum in x-direction.

Surface plasmon polaritons are longitudinal surface charge oscillations excited by diffracted s-polarized light ($\vec{E}$) [88, 89]. So our findings are orthogonal to surface plasmon resonances - in their classical picture.

As the effective medium approach does not consider interactions of a metamaterial's elements, collective oscillations were widely ignored in metamaterial literature, prior to publication P1. In recent studies, magnetic plasmons [90], surface plasmons in fishnet metamaterials [91] and other collective oscillations reviewed in ref. [92] were reported. None of them, however, explain the physical mechanism underlying the collective resonance characterized here, because of their unique orientation. This will have to remain an open question as any further speculation is beyond the biophotonic scope of this thesis. However, additional experimental results and an Ansatz explaining collective oscillation behavior by polariton theory may be found in S. Schlögl's diploma thesis [93].

4 Nanoapertures for AFM-based single molecule force spectroscopy

Nanophotonic devices facilitate access of information on biomolecules while bringing about minimal changes in the environment. This is mainly true regarding chemical and biological alterations. In case of ZMWs, even the spatial environment is almost unaltered when compared to other advanced single-molecule methods like NSOM or optical tweezers [94]. This accessibility of the upper half-space of a ZMW sample allows the employment of an AFM whose tip can reach the bottom of a ZMW for manipulation. This compatibility makes ZMWs the long missed tool that enables the combination of two very powerful single-molecule techniques: fluorescence and force spectroscopy.

So far, simultaneous single-molecule force and fluorescence spectroscopy has been applied to e.g. labeled DNA [95, 96] but the actual observation of enzymatic substrate turnover at the single-molecule level was limited by the diffraction limited observation volume to picomolar concentrations of labeled substrate: The low probability of substrate binding coming with these low concentrations can sometimes be compensated in massively parallel arrangements where enzymes in hundreds or thousands of waveguides can be observed in parallel. But for single-molecule investigation of force-activated enzymes, low binding probabilities are experimentally unacceptable as optical tweezers or AFM can probe only one enzyme at a time. An alternative scenario has been the employment of substrates that become fluorescent upon enzymatic catalysis [97]. Unfortunately, these fluorescent products are rare and hard to observe with single-molecule resolution because, often, they have low quantum yields or do not start fluorescing before enzymatic release will end additional quenching but start diffusion from of the observation volume.

ZMWs were designed to solve the problem of low substrate concentrations and are applicable for most natural enzyme-substrate combinations (see chapter 2.2). Their sole requirements are that the size of the enzyme substrate complex must fit the ZMW and that the substrate must be suited with a label. Dye labeling can be an obstacle when any influence of the label on enzymatic processing is to be avoided. However, the most important substrates like adenosine triphosphate (ATP) and most nucleic acids are already commercially available in various labeling stoichiometries and with different dyes.

On the other hand, the benefits of a simultaneous fluorescence read-out are tremendous: As force activated enzymes are autoinhibited, determination of their enzymatic rates with conventional ensemble techniques requires unnatural alterations like “activation” through truncation of the inhibitory domain [1]. Alternatively, sophisticated force pulling studies on single molecules as done by Puchner et al. [1] can reveal on and off rates but this has the prerequisite that substrate binding significantly effects the enzyme’s structural stability.

So combined single-molecule force and fluorescence spectroscopy in ZMWs has all requisites for becoming a highly valued tool in biomolecular research of force-activated enzymes:

- natural conditions
- applicable to most enzymes and substrates
- unambiguous data through the combination of two established and independent techniques

This chapter presents the pioneering study on combined force and fluorescence microscopy of enzymes at natural conditions. It includes unfolding of titin kinase (TK) on the bottom of ZMWs and simultaneously recorded proof-of-principle fluorescence traces marking the possible substrate binding to the force activated enzyme. Technical challenges of this new technique are discovered and solutions are suggested.

4.1 Summary of Associated Publication P2

Publication P2 is divided in two parts: First, the fabrication of ZMWs samples applicable for force spectroscopy is described and the samples are characterized. Then, in the second part, the methodology of the proposed technique is described and the pioneering results are presented.

Force spectroscopy in ZMWs requires large glass windows allowing to visualize the cantilever tip in transmission microscopy and broadly align it with a ZMW structure. As milling of large areas into a metal film with a focused-ion beam is very time consuming, a pattern of large glass and aluminum areas was first fabricated on a cover glass by optical lithography. The waveguides were then milled into the designated and marked aluminum areas by the FIB. To find the correct milling dose, test arrays of apertures were characterized with electron beam microscopy and AFM.

Regarding storage and buffer usage, we found that the aluminum waveguides were often subject to corrosion and it could be proved that this was partially induced by the ZMWs themselves: Subdiffusion in the apertures enhances autocatalytic corrosion processes – a phenomenon known for naturally occurring nanoscopic cracks in aluminum [98]. For artificial nanoholes this issue had not yet been reported. We could significantly reduce corrosion by usage of chloride-free buffers and dry-storage of the ZMW samples.

The correct observation volume confinement of the milled ZMWs was then tested in diffusion experiments and found to be sufficient for micromolar label concentrations.

Publication P2 then describes the technical necessities for force spectroscopy in ZMWs. Major requirements are additional transmission and TIRF microscopy modes. For transmission mode, light-emitting diodes on the AFM head were employed. Regarding TIRF microscopy, the EMCCD camera of the custom-built hybrid microscope setup [99] was synchronized with the AFM controller in such a way that a force-pulling event triggered the fluorescence signal recording with a precision beyond one millisecond.

As to the actual force-pulling experiments, TK protein elongated with Ig-domains was unspecifically immobilized on the sample surface, any unbound TK was washed away and the sample was incubated with experimental buffer containing 1 μM Cy3-labeled ATP. Rough alignment of AFM tip was done in transmission mode: Due to its increased length, the actual tip of a high-aspect ratio cantilever transmits less white light than the cantilever itself and thus is visible as dark spot of approx. 400 nm diameter. This “shadow” was roughly aligned with a 150 nm ZMW visible as white spot from extraordinary transmission [18]. A following topography scan of 1 × 1 μM revealed the actual position of the ZMW relative to the cantilever with nm precision, and force pulling routines were started with the cantilever in the center of the aperture. After approximately 70 force curves, another scan assured that the AFM had not drifted out of the aperture.

With an occurrence of only 1%, 8 clear TK unfolding patterns could be recorded from ZMW surfaces. Only one of these shows a distinct plateau in its simultaneously recorded fluorescence trace. However, the time at which this plateau occurs, correlates with the unfolding of the inhibitory domain[1]. Together with the lack of plateaus in the other curves, this strongly suggests the successful premiering optical observation of an ATP binding event to a force-activated TK.

Eight successful unfolding events seem statistically insignificant to draw conclusions about ATP affinity or exact time-correlations of activation and binding behavior. These results, however, demonstrate the general feasibility of combined force- and fluorescence microscopy in ZMWs. While the overall TK-unfolding efficiency can be highly improved by specific immobilization arrangements, the number of overall pulling events is limited by the slow and elaborate localization via AFM scans and furthermore by irreversible protein-clogging of the cantilevers resulting from these scans. This protein-clogging is the current bottle-neck of the method, and the most promising approach employing superresolution optics to localize cantilever and ZMW will be discussed in the chapter 5.

4.2 Associated Publication P2

Nanoapertures for AFM-based single molecule force spectroscopy

by

Stephan F. Heucke, Elias M. Puchner, Stefan W. Stahl,
Alexander W. Holleitner, Hermann E. Gaub and Philip Tinnefeld

published in

International Journal of Nanotechnology, 10 (5/6/7), 607–619, 2013

Int. J. Nanotechnology, Vol. 10, Nos. 5/6/7, 2013 607

Nanoapertures for AFM-based single-molecule force spectroscopy

Stephan F. Heucke

Center for Nanoscience and Department of Physics,
Ludwig-Maximilians-Universität München,
Amalienstr. 54, 80799 Munich, Germany
Email: stephan.heucke@lmu.de

Elias M. Puchner

Department of Cellular and Molecular Pharmacology,
University of California,
600 – 16th Street, San Francisco, CA 94158, USA
Email: elias.puchner@ucsf.edu

Stefan W. Stahl

Center for Nanoscience and Department of Physics,
Ludwig-Maximilians-Universität München,
Amalienstr. 54, 80799 Munich, Germany
Email: stefan.stahl@physik.uni-muenchen.de

Alexander W. Holleitner

Walter Schottky Institut and Physik-Department,
Technische Universität München,
Am Coulombwall 4a, 85748 Garching, Germany
Email: holleitner@wsi.tum.de

Hermann E. Gaub*

Center for Nanoscience and Department of Physics,
Ludwig-Maximilians-Universität München,
Amalienstr. 54, 80799 Munich, Germany
Email: gaub@lmu.de
*Corresponding author

Philip Tinnefeld

Physikalische und Theoretische Chemie – NanoBioSciences,
Technische Universität Braunschweig,
Hans-Sommer-Strasse 10, 38106 Braunschweig, Germany
Email: p.tinnefeld@tu-braunschweig.de

Abstract: Simultaneous single-molecule force spectroscopy and microfluorescence binding measurements are often hampered by background fluorescence from the bulk. Zero-Mode Waveguides (ZMW) restrict the excited volume but require a special design, which allows the tip of the force probing cantilever to protrude into the nanoaperture. Here, we describe the design and fabrication of such ZMW and report the first experiments where binding of fluorescent adenosine triphosphate to the force-activated enzyme titin kinase was measured while the enzyme was subjected to mechanical forces.

Keywords: single-molecule force spectroscopy; zero-mode waveguide; nanoaperture; force-activated enzyme; mechanoenzymatics; titin kinase; AFM; nanotechnology; single-molecule fluorescence.

Reference to this paper should be made as follows: Heucke, S.F., Puchner, E.M., Stahl, S.W., Holleitner, A.W., Gaub, H.E. and Tinnefeld, P. (2013) 'Nanoapertures for AFM-based single-molecule force spectroscopy', *Int. J. Nanotechnology*, Vol. 10, Nos. 5/6/7, pp.607–619.

Biographical notes: Stephan F. Heucke received his MSc in Physics from St Andrews University, Scotland, in 2007. He is currently finalising his PhD in Physics at LMU. His research interests include nanopositioning, manipulation and fluorescence spectroscopy of single molecules, metallic nanostructures and force spectroscopy of biomolecules.

Elias M. Puchner studied Physics at the LMU Munich and received his PhD from Hermann Gaub's Lab. He combined AFM-based single-molecule force spectroscopy and fluorescence microscopy to study mechanoenzymatic processes and to assemble biomolecules to complexes. In his current postdoctoral research in the Lim Lab at UCSF, he investigates the spatial organisation and regulation of signalling proteins in cells.

Stefan W. Stahl studied Physics at the LMU Munich and graduated in 2008. He received his PhD at the chair of Hermann Gaub at the LMU Munich in August 2012. His research interests include AFM-based single-molecule force spectroscopy experiments and its combination with fluorescent techniques.

Alexander W. Holleitner currently is an Associate Professor at TU Munich. He studied Physics at LMU Munich where he received his PhD in 2002. He then went to UCSB for postdoctoral research. His interests lie in optical and electronic phenomena on the nanometre scale, methods of nanostructuring and physical characterisation of solid-state devices.

Hermann E. Gaub studied Physics in Ulm and received his PhD form the TU-Munich before going to Stanford for postdoctoral research. He currently holds the chair in Applied Physics at the LMU-Munich. He pioneered the use of atomic force microscopy for the study of the mechanical properties of single molecules.

Philip Tinnefeld studied Chemistry in Münster, Montpellier and Heidelberg. In 2002, he received his PhD from the University of Heidelberg. After his Habilitation at the University of Bielefeld, he became Professor at LMU-Munich. Since 2010 he is Professor of Biophysical Chemistry at TU Braunschweig. His research interests include the development of microscopy techniques and applications of DNA nanotechnology to study problems at the interface of physics, chemistry and biology.

This paper is a revised and expanded version of a paper entitled 'Force and function: mechanoenzymatics investigated by single molecule force spectroscopy' presented at the 'Nanoscale Science and Technology (NS&T'12) Conference', Hammamet, Tunisia, 17–19 March 2012.

1 Introduction

The rapidly evolving single-molecule techniques have revolutionised modern life sciences. Since the first realisation of this concept in single-ion channel recordings, the access to properties of individuals rather than the collective response of an ensemble has brought stunning insight into a broad range of phenomena and opened entire new research fields [1]. For example, fluorescence microscopy with single-molecule resolution allows imaging beyond the Abbe limit or in combination with Förster Resonance Energy Transfer (FRET) the relative localisation of labels with angstrom precision [2]. Mechanical experiments with single-molecule resolution and piconewton sensitivity provided for the first time control over a new and, as it turned out, extremely important parameter in molecular interaction: force [3]. The functional mechanisms of molecular motors were interrogated with techniques like AFM and optical tweezers, and forces governing protein folding or nucleic acid suprastructures were determined [4–7].

With its superb position control with sub-Å precision, the AFM moreover provides an additional feature, which goes far beyond force spectroscopy. It allows the molecular manipulation of individual molecules at surfaces. With the introduction of Single-Molecule Cut & Paste (SMC&P), a technique became available which allows for a controlled pick up of individual molecules, like proteins from a surface, and their one by one deposition at a chosen position at a surface [8].

It is obvious that a combination of these two strong single-molecule techniques, fluorescence and mechanics, provides a realm of new possibilities of controlled manipulation. Hybrid instruments were developed that allowed in one-half space of the sample the manipulation of the molecules by AFM and in the other half fluorescence microscopy in TIRF excitation via the microscope objective [9]. New phenomena such as force-triggered enzyme reactions were investigated, or the functional reconstitution of individual RNA aptamers by SMC&P was monitored [10, 11].

In previous studies, we had investigated by AFM-based single-molecule force spectroscopy the force-activation of titin kinase (TK), a functional module in the giant muscle protein titin, which organises the molecular architecture of the sarcomere and provides its passive elasticity [12–14]. We had shown that the auto-inhibition of this enzyme is removed by a stretching force of 40 pN exposing the putative active site [12]. A direct observation of the binding of adenosine triphosphate (ATP) for example by means of fluorescence would unambiguously clarify this process. To design such a simultaneous single-molecule optomechanical experiment and to elucidate the boundary conditions for such an investigation was the motivation of this study.

When the mechanically probed molecules are labelled either covalently or via a high affinity binder and where no fluorescent molecules remain in the sample volume the experimental designs are straightforward. However in cases where a limited affinity of the label results in substantial background fluorescence from the bulk fluorophores, discrimination of the single molecule under investigation against the background soon

becomes a limiting problem. Particularly for the investigation of interactions of soluble ligands in equilibrium with an immobilised receptor at the surface, the background signal of ligands in solution may overwhelm the single-molecule signal from the surface.

The contribution of the bulk molecules to the signal may be estimated as follows: both in Confocal Fluorescence Microscopy (CFM) and TIRF excitation, the detection volume has a lower bound of somewhat less than 1 μm^3. Background fluorescence caused by the labels of mobile ligands in this volume will come from

$$n = cVN_A \tag{1}$$

molecules where c is the ligands' molar concentration, V is the detection volume and N_A is Avogadro's number. This means that for a signal-to-background ratio of 1 and a minimum voxel volume of 1 μm^3 the concentration of analytes in solution must not exceed a concentration of 0.16 nM.

In order to study interactions amongst molecules close to equilibrium, the interaction partners need to be present in concentrations on the order of the equilibrium constant. Particularly when enzymes are to be studied in their interaction with labelled substrates, this boundary condition imposes severe limitations, particularly at high Michaelis–Menten constants. Figure 1 depicts a histogram of all Michaelis–Menten constants for enzymes known today. It is an updated version of the viewgraph that Samiee et al. [15] used to rationalise the need for improved methods to reduce background fluorescence. It shows that the large majority of enzymes known to date have a K_M around 100 µM and can therefore not be investigated with conventional fluorescence microscopy techniques, like CFM or TIRFM.

Figure 1 Histogram of Michaelis–Menten constants (K_M) for 62,000 enzymes taken from the Brenda database (see http://www.brenda-enzymes.info). It emphasises how conventional fluorescence techniques fail to observe single-enzyme kinetics at natural concentrations of labelled substrates. The use of Zero-Mode Waveguides (ZMW), however, allows experiments at label concentrations up to 100 µM (see online version for colours)

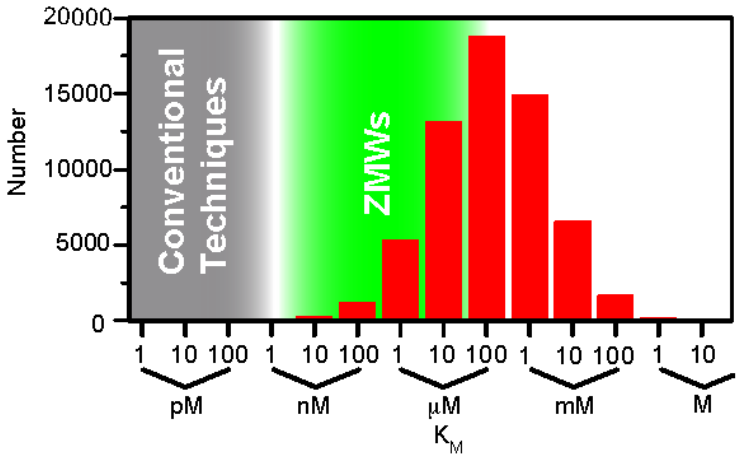

Due to the nature of our proposed experiment, there is generally another reason to work near equilibrium than its obvious physiological relevance: the time window in which an enzyme that is subject to an activating force is able to form an enzyme-substrate complex

is usually limited, as the current force-pulling techniques will not be able to prevent rupture for arbitrarily long times. Thus, low-affinity ligand must be compensated with high-substrate concentration.

The labs of Web and Craighead found a very elegant means to reduce the background fluorescence. They used nanoapertures in metal films which they called Zero-Mode Waveguides (ZMW) and measured the emission of fluorophores form within the holes [16]. Since the largest part of the voxel is occupied by metal, only the remaining aperture volume may contribute to the bulk background signal. An additional reduction of the excitation volume comes from the field geometry within the nanoaperture. Since ZMWs have diameters much smaller than the wavelength of the incident light that they allow zero light propagation. Instead, the incoming light gets reflected at the apertures and an evanescent field illuminates only at the bottom of the waveguides.

Since their introduction in 2003 by Levene et al., ZMWs have proven their applicability in a variety of studies: besides relatively straightforward fluorescence correlation spectroscopy of protein–protein interactions [17], diffusion within lipid bilayers inside ZMWs [18] could be monitored as well as membrane regions of living cells [19]. Most prominently, the use of ZMWs in a massively parallel approach allowed time- and cost-efficient DNA-sequencing [20].

In the present work, we will first describe the fabrication of ZMWs by Focused-Ion-Beam (FIB) milling. We then characterise their design and discuss handling and storage issues that have to be dealt with when using ZMWs. We will show fluorescence spectroscopy data form within our ZMWs and introduce the experiments combining force and fluorescence spectroscopy in a set-up schematically depicted in Figure 2. Finally, we will present initial results of ATP binding to titin kinase in ZMWs and discuss what further improvements are to be done to standardise force spectroscopy in ZMWs.

Figure 2 Schematic diagram of the conducted experiment: an AFM cantilever triggers the enzymatic activity of a force-regulated enzyme immobilised at the bottom of a zero-mode waveguide. Additionally to the force–distance information from the AFM, the binding of fluorescently labelled substrates can be characterised optically with a TIRF microscope. The waveguide is necessary to limit the exciting field to the enzyme at the bottom and thus reduce fluorescence from diffusing substrates (see online version for colours)

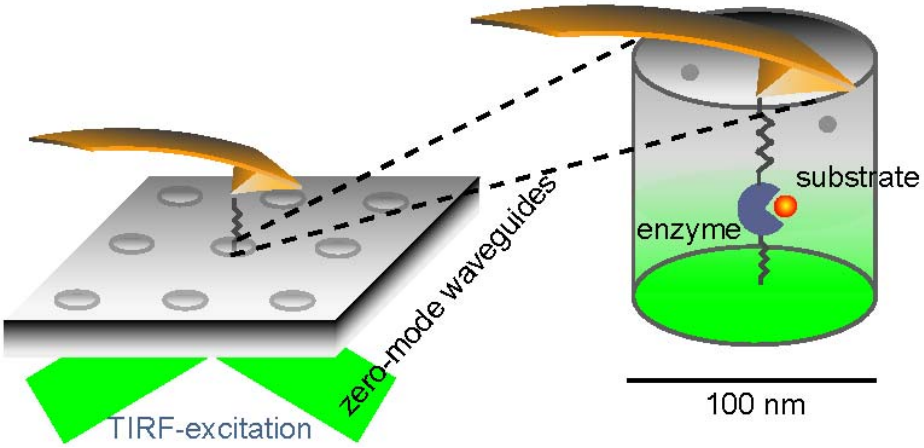

2 Zero-mode waveguides

2.1 Fabrication of zero-mode waveguides

For fabrication of ZMW, we used an FIB method described by Rigneault et al. [21]. Compared to the other two common ZMW fabrication methods, reactive ion etching [16] and eBeam-lithography [22], FIB milling is the least elaborate process. It consists of two basic steps: first blanks are fabricated by evaporating a thin aluminium film onto a glass substrate. Then nanometre-sized holes are milled into the aluminium film with an FIB.

We altered the first step and used negative tone optical lithography to produce blanks with orientation markers and wide glass windows. This was done to allow by-eye alignment of the AFM cantilever to designated ZMWs in the later experiments.

We cleaned conventional glass cover slips in consecutive ultrasonic bathes of acetone, isopropanol and double-distilled water (ddH_2O). Samples were then dried under a nitrogen stream and treated with oxygen plasma (Femto, Diener, Ebhausen, Germany) for 2 min at 100 W. To remove adsorbed water from the glass surface, substrates were heated up to 120°C for 2 min on a hot plate and cooled down under a dry steam of nitrogen just prior to photoresist coating. Negative tone photoresist (AZ5214E, Microchemicals, Ulm, Germany) was spun onto the substrates at 4000 rpm for 60 s with an accelerating ramp of 9 s followed by a prebake at 120°C for 60 s. Samples were exposed to UV-light (320 nm wavelength) for 35 s at 5.1 W/cm^2. During exposure, contact of a chromium mask with the substrate was achieved by a mask aligner (MA6, Suess Microtec, Garching, Germany). A post-exposure bake at 120°C for 120 s was followed by flood exposure of the whole surface for 105 s at the previously used wavelength and power. The exposed samples were developed in AZ726 (Microchemicals) for 40 s, dipped in consecutive stop and rinse baths of ddH_2O for 30 s each and then dried under a nitrogen stream. To remove undesired photoresist remains, samples were again treated with oxygen plasma for 60 s at 100 W power. A 110 nm thick aluminium film was evaporated in a thermal evaporator (306 Turbo, Edwards, Crawley, UK) with a rate of 0.1 nm/s at a pressure of 1.7×10^{-6} mbar. Lift-off was done in 40°C warm acetone. To support the lift-off process, a turbulent stream was created locally with handheld glass pipette. Samples were then cleaned by 30 s dips in isopropanol and ddH_2O followed by a rinse in ddH_2O and a final treatment with oxygen plasma for 120 s at 100 W.

We used a NVISION40 FIB (Zeiss, Oberkochen, Germany) to mill arrays of ZMWs into the designated metallic areas on the blanks. Array periodicity was 5 µm in the x-direction and the y-direction. The FIB aperture was set to 30 µm and the ion current was measured to be 10 pA at an acceleration bias of 30 kV. With these settings, milling doses for the ZMWs ranged from 120.000 to 200.000 µA/cm^2.

2.2 Characterisation of zero-mode waveguides

The challenge of the FIB-milling method comes from the manual focusing of the ion-beam, which requires optimisation and experience to fabricate reproducible ZMWs. Therefore, careful analysis of the fabricated structures is a prerequisite to successful experiments.

Due to the directionality of the milling process, the apertures' sidewalls converge towards the bottom of the hole rather than diverge. This makes the upper aperture diameter maximal and thus a sufficient criterion for an aperture being a ZMW. The depth of milling is set just below the glass interface to minimise negative effects of aluminium residues at the bottom of the aperture on the excitation and photophysical properties of the fluorophores as well as on the coupling efficiency for immobilisation.

ZMWs' opening diameters were analysed immediately after milling with the NVISION's SEM at an electron beam incidence angle of 54° (see Figure 3a). This allowed corrections of the FIB focus before milling further ZMWs on the same blank. AFM scans ensuring a sufficient depth was done later with a commercial AFM (MFP3D, Asylum Research, Santa Barbara, USA) operated in tapping mode in air. To correct for drift and sample tilt, a flattening algorithm was applied to the topography scans as the one shown in Figure 3b. To avoid not only slow scanning but also breakage of the cantilever, we chose a relatively robust cantilever (MSCT, Bruker, Camarillo, CA, USA). The SEM image of an MSCT tip in Figure 3c is a 90° side view of the tip and was made with a LEO-SEM (Zeiss). A comparison with the cantilever dimensions reveals that the cross-section in Figure 3b is rather a plot of the probe's shape than of the aperture. Nevertheless, opening diameter and minimal depth are still valid information from the scan.

Figure 3 (a) SEM image of a zero-mode waveguide. (b) Section through an AFM scan of a ZMW. The red line in the inserted scan marks the position of the section. (c) A SEM micrograph of the used cantilever's side view (see online version for colours)

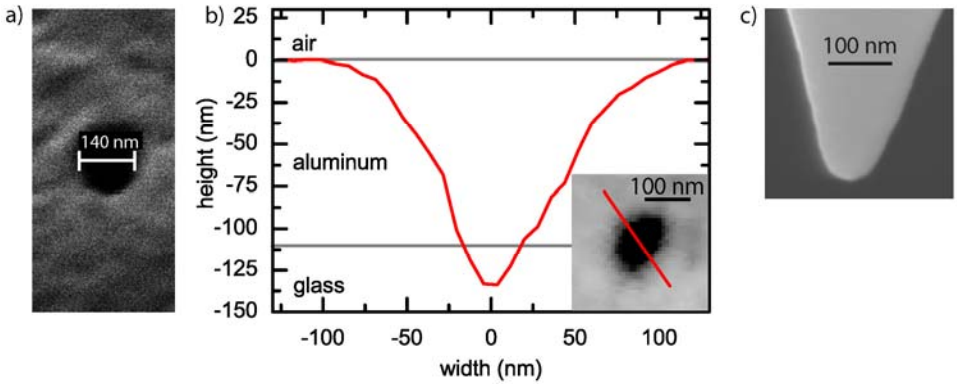

2.3 Corrosion of zero-mode waveguides

Working with ZMWs, we occasionally experienced degradation of samples due to corrosion. Although Korlach et al. [23] emphasised that passivation with polyvinylphosphonic acid prevents corrosion [23], corroded ZMWs have not yet been reported in the literature. In this section, we will thus present findings of corrosion and discuss possible mechanisms, reasons and precautions.

Aluminium is generally preferred over, for example, gold or silver as ZMW material. This is mainly due to its short skin depth and low-plasmonic coupling efficiency in the visible spectrum, where latter would increase the observation volume inside and above the ZMW by surface plasmon excitation. Another advantage of aluminium is its generally high-chemical stability and that it does not gradually oxidise and thus alter its

optical properties. Instead, aluminium forms a steady oxide layer of approximately 3 nm within seconds upon first contact to air and then remains unaltered for months if handled correctly [24]. However, when this passive layer is lost – even just locally – due to critical chemical conditions, impurities or physical stress, the underlying metal is subject to corrosion until an oxide layer reforms. For further details of the different corrosive processes see references [25, 26].

We found large areas (0.1–10 mm^2) of our aluminium surfaces corroded when stored in non-dry environments for days. We also witnessed corrosion upon abnormally high indentation with a cantilever. Most interestingly, however, we found signs for corrosion caused by the nanohole structures themselves.

Figure 4 shows a transmission image and an AFM-topography scan of a nanohole array milled for dose test purposes. Prior to the analysis, the sample had been incubated in 1x PBS buffer for 24 h. The original hole depth was approximately 60 nm into the 110 nm thick aluminium and original diameters had not exceeded 200 nm. One notices that some of the nanoapertures show perfectly circular corrosion patterns of arbitrary diameters ranging up to 4 µm, while other apertures remained unaltered. A striking feature best seen in the cross-section in Figure 4c is the thin rod that remained at the original hole position.

Figure 4 A transmitted light image (a) and an AFM topography scan (b) of the same nanohole array. The green grid (5 µm periodicity) was drawn to guide the eye. The nanoholes had an original depth of approximately 60 nm into the 110 nm thick aluminium film. The green arrows point out a pillar remaining at the original position of a corroded hole. The actual depth of the uncorroded nanohole (blue arrow) is not resolved in this scan (see online version for colours)

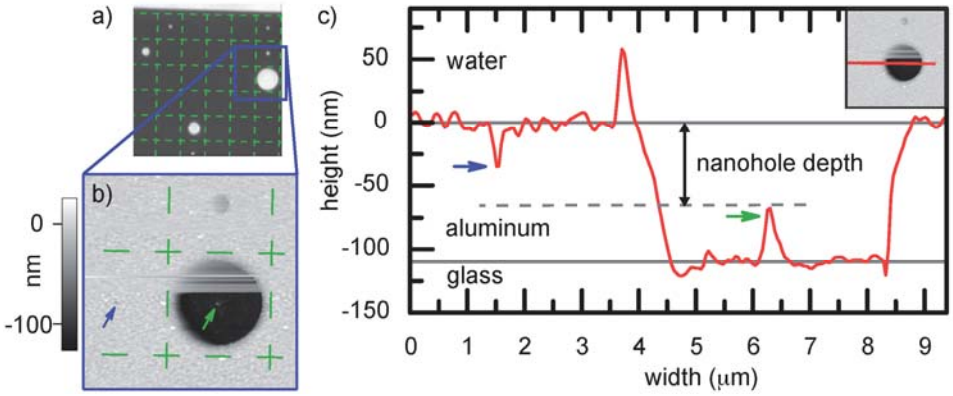

We interpret this rod as corrosion resistant, aluminium remains contaminated with FIB gallium ions. Contaminations are a known side effect of FIB milling [27]. These gallium remains are also a possible cause for an insufficient formation of the apertures' oxide layer that would then allow corrosion to start.

Another explanation for corrosion nucleation or corrosion enhancement in nanoapertures is related to their geometry: their confined volume limits diffusion and thus enhances autocatalytic pathways including the accumulation of chloride ions and the prevention of surface passivation by oxygen. This phenomenon is known, for example, micro cracks or other confined microstructures in material science as crevice corrosion

[25, 26]. This interpretation of our corrosion findings is especially striking, since it is an intrinsic property of the apertures and independent of our FIB-milling method.

We learned to drastically reduce corrosion by storing ZMW samples under argon and by avoiding buffers with chloride ions where possible.

3 Combined force and fluorescence spectroscopy of titin kinase

3.1 Experiment

Combined force and fluorescence spectroscopy was performed on a homebuilt AFM-TIRF-hybrid instrument described by Gumpp et al. [9]. However, we used a different 532 nm laser (Cobolt Samba, Cobolt, Stockholm, Sweden), a lower magnification oil objective (CFI Apochromat TIRF 60× oil, N.A. 1.49, Nikon, Tokyo, Japan) and another EMCCD-camera (iXon + 860, Andor, Belfast, Northern Ireland). The AFM part of the instrument did not differ from the one described in the publication.

To synchronise both units of the instrument, an additional source code was implemented in the AFM software. Thus, at the start of a force-pulling event, the AFM-controller triggered the EMCCD-camera via the camera's external trigger.

Expression and purification of the TK protein construct A168M2 (867 amino acids, from position 24422–25288 in human cardiac N2-B titin, accession No. NP 003310.3) is described in the supporting material of Puchner et al. [12]. For the actual experiments combining force-activation and fluorescence spectroscopy, 0.5 μM TK was incubated in HEPES buffer (40 mM, pH 7.2, 2 mM MgCl2) on untreated ZMWs for 20 min.

The approximate diameter of the used apertures was 150 nm. TK that did not adsorb to the substrate was washed away by buffer exchange. For the measurement, HEPES buffer containing 1 μM ATP was used. The ATP was labelled with a Cy3 dye at the gamma phosphate and is commercially available from Jena Bioscience (Jena, Germany).

To allow access to most of the ZMW's bottom, we used a high aspect ratio cantilever (Biolever Mini, Olympus, BL-AC40TS), which also showed less fluorescence background signal from inelastic scattering due to its silicon tip. In SEM images (not shown), we measured the cantilever's width to be smaller than 50 nm at a distance of 110 nm away from its tip thus allowing to probe the inner 100 nm wide disc of a 150 nm diameter hole. To avoid large area AFM scans resulting in a TK clogged cantilever, we did a broad alignment of the cantilever's shadow (light source was a handheld flashlight by MagLite, USA) and the ZMWs (visible from diffusing of labelled ATP in TIRF configuration). Following this alignment procedure, we were able to localise individual ZMWs in 1 × 1 μm topography scans. We then started our force-pulling routines with the cantilever localised in the ZMW's centre. After 100 force-pulling events another 1 × 1 μm topography scan ensured that our cantilever's picking position had not moved out of the ZMW despite thermal drift.

A force-pulling event started with an approach at 3 μm/s velocity. Pulling velocities were varied: during the first 75 nm of retraction, a reduced pulling velocity of 200 nm/s was applied in order to widen the time window in which a substrate could bind. The remaining pull was done with a speed of 1 μm/s.

For the fluorescence time traces shown in Figures 5 and 6, the mean signal of a 3 × 3 pixel square containing the ZMW's centre was calculated and plotted over time.

Figure 5 Fluorescence intensity of Cy3-labelled ATP molecules (0.5 µM) diffusing in and out of a ZMW. The average dwell time is less than the camera's time resolution of 1 ms (see online version for colours)

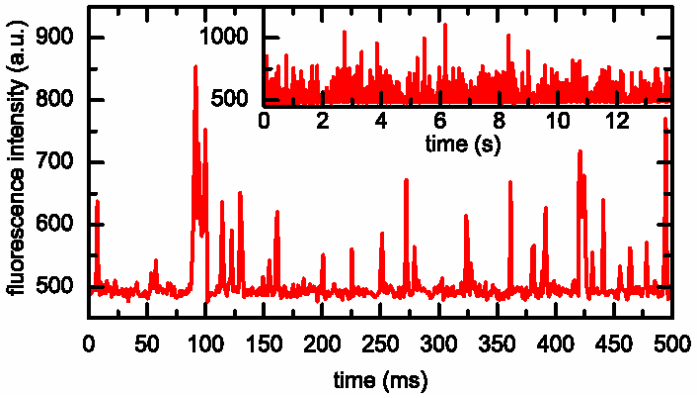

Figure 6 Two force-pulling curves from the bottom of a ZMW show the characteristic unfolding pattern of titin kinase (upper curves). The pulling speed was switched from 200 to 1000 nm/s at approximately 75 nm above the surface (grey line). The fluorescence intensity signal (lower curves) shows background only in the left case and a possible ATP binding event around 0.83 s (marked with a star) in the right case (see online version for colours)

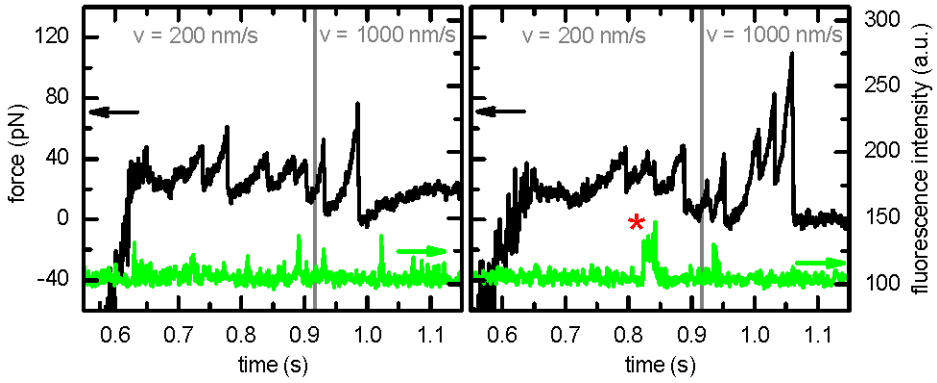

3.2 Results and discussion

To test sufficient optical confinement and thus ZMW characteristics of our nanoapertures, we first recorded fluorescence from diffusing labelled ATP in the absence of TK.

A typical fluorescence time trace is shown in Figure 5. The separated spikes of varying height and dwell times below the camera's time resolution of 1 ms are characteristic for concentrations below single-molecule occupation [16]. Spike frequency is in the order of the theoretical occupancy of 0.015 molecules given by equation (1) when assuming an illumination depth of 20 nm and 150 nm ZMW diameters. An autocorrelation analysis (data not shown) did not exhibit plateaus within our time resolution. These results verify strong optical confinement and thus ZMW character.

Compared to these initial experiments, we chose one magnitude less laser power and a twofold ATP concentration for the actual force-activation experiments to minimise dye bleaching and increase substrate-binding probabilities, respectively.

Figure 6 shows force and fluorescence intensity data recorded during force-pulling events in ZMWs. Both force curves show the characteristic unfolding pattern of TK with its attached Ig-domains. The two corresponding fluorescence traces show spikes below the resolution limit that we denote as diffusing ATP. Additionally the right time trace features a distinct fluorescence plateau (marked with a star). In agreement with reference [14], the plateau appears just after unfolding of the second barrier and its length of approximately 30 ms is too long to be explained with a non-bound merely diffusing ATP molecule (Figure 5).

This distance correlation and the lacking of similar fluorescence signatures in other force curves recorded in the same experiment suggest that the recorded data shown in Figure 6b is optical evidence of single ATP molecule binding to a TK upon force-activation.

Stronger evidence has to be given by statistics. However, our described experiment is yet far from a high-throughput method. We only found eight clear TK unfolding signatures in a total of 700 recorded force curves, distributed over ten ZMWs. This yield of 1% is comparable to other unspecific force spectroscopy measurements with that TK construct. Since our protocol cannot be completely automated so far and its trace acquisition rate is much lower, a long-term measurement over several days is not feasible. A straight forward method to enhance this yield is the use of a specific immobilisation procedure or – more sophisticated – the employment of SMC&P. Latter can be used to pick up proteins in small but very dense protein depots and probe them upon anchoring in a ZMW. Another factor limiting our statistics is the collection of protein during localisation scans that eventually leads to clogging of the cantilever. An optical alignment procedure using super-resolution techniques to localise and non-invasively align cantilever and ZMW could make AFM scans obsolete.

4 Conclusion

For the optical investigation of substrate binding to mechanoactive enzymes, physiologically high equilibrium concentrations are not only scientifically desirable but also an experimental requirement. As discussed above, this intrinsic demand comes from signal-to-background limitations as well as the short time window between the activation of a force-activated enzyme and its rupture under the tension caused by the activation. So far background fluorescence going along with these high substrate concentrations prevented the optical observation of single-binding events in such experiments.

In the study presented here, we showed how ZMWs can be used to overcome these limitations. We characterised the necessary fabrication methods and designs as well as the chemical environment necessary for such an experiment. Meeting these conditions, we were able to conduct the first experiment that optically observed the binding of a single substrate to an enzyme force-activated at the bottom of a ZMW.

With this first proof of principle, we believe that the use of ZMWs will now allow the application of the powerful techniques of fluorescence microscopy in their whole bandwidth and thus open up unprecedented characterisation possibilities for force-activated enzymes.

In a more general view, the proven possibility to mechanically access and manipulate molecules in ZMWs widens the range of applications for ZMWs even further. For example, this opens up the possibility to use SMC&P in ZMWs. Applied to ZMWs, SMC&P could be used to selectively immobilise anchors or enzymes at desired positions, like hotspots within the nanoapertures.

Acknowledgements

We thank Prof. D. Schomburg of TU Braunschweig for raw data from the BRENDA database, Mathias Gautel of King's College (London) for providing TK, Wolfram Summerer, Peter Weiser and Leopold Prechtel of TU Munich for technical advice with the FIB. This work was supported by the DFG through SFB 863, Volkswagen Stiftung and the German excellence initiative via the 'Nanosystems Initiative Munich' (NIM). S.H is grateful to the Elite Network of Bavaria (IDK-NBT) for a doctoral fellowship.

References

1 Neher, E. and Sakmann, B. (1976) 'Single-channel currents recorded from membrane of denervated frog muscle fibres', *Nature*, Vol. 260, No. 5554, pp.799–802.

2 Tinnefeld, P. and Sauer, M. (2005) 'Branching out of single-molecule fluorescence spectroscopy: challenges for chemistry and influence on biology', *Angewandte Chemie International Edition*, Vol. 44, No. 18, pp.2642–2671.

3 Florin, E., Moy, V. and Gaub, H.E. (1994) 'Adhesion forces between individual ligand-receptor pairs', *Science*, Vol. 264, No. 5157, pp.415–417.

4 Nishizaka, T., Miyata, H., Yoshikawa, H., Ishiwata, S. and Kinosita Jr., K. (1995) 'Unbinding force of a single motor molecule of muscle measured using optical tweezers', *Nature*, Vol. 377, No. 6546, pp.251–254.

5 Rief, M., Gautel, M., Oesterhelt, F., Fernandez, J.M. and Gaub, H.E. (1997) 'Reversible unfolding of individual titin immunoglobulin domains by AFM', *Science*, Vol. 276, No. 5315, pp.1109–1112.

6 Clausen-Schaumann, H., Rief, M., Tolksdorf, C. and Gaub, H.E. (2000) 'Mechanical stability of single DNA molecules', *Biophysical Journal*, Vol. 78, No. 4, pp.1997–2007.

7 Woodside, M.T., Anthony, P.C., Behnke-Parks, W.M., Larizadeh, K., Herschlag, D. and Block, S.M. (2006) 'Direct measurement of the full, sequence-dependent folding landscape of a nucleic acid', *Science*, Vol. 314, No. 5801, pp.1001–1004.

8 Kufer, S.K., Puchner, E.M., Gumpp, H., Liedl, T. and Gaub, H.E. (2008) 'Single-molecule cut-and-paste surface assembly', *Science*, Vol. 319, No. 5863, pp.594–596.

9 Gumpp, H., Stahl, S.W., Strackharn, M., Puchner, E.M. and Gaub, H.E. (2009) 'Ultrastable combined atomic force and total internal fluorescence microscope', *Review of Scientific Instruments*, Vol. 80, No. 6, pp.063704–063705.

10 Gumpp, H., Puchner, E.M., Zimmermann, J.L., Gerland, U., Gaub, H.E. and Blank, K. (2009) 'Triggering enzymatic activity with force', *Nano Letters*, Vol. 9, No. 9, pp.3290–3295.

11 Strackharn, M., Stahl, S.W., Puchner, E.M. and Gaub, H.E. (2012) 'Functional assembly of aptamer binding sites by single-molecule cut-and-paste', *Nano Letters*, Vol. 12, No. 5, pp.2425–2428.

12 Puchner, E.M., Alexandrovich, A., Kho, A.L., Hensen, U., Schäfer, L.V., Brandmeier, B., Gräter, F., Grubmüller, H., Gaub, H.E. and Gautel, M. (2008) 'Mechanoenzymatics of titin kinase', *Proceedings of the National Academy of Sciences*, Vol. 105, No. 36, pp.13385.

13 Stahl, S.W., Puchner, E.M., Alexandrovich, A., Gautel, M. and Gaub, H.E. (2011) 'A conditional gating mechanism assures the integrity of the molecular force-sensor titin kinase', *Biophysical Journal*, Vol. 101, No. 8, pp.1978–1986.

14 Puchner, E.M. and Gaub, H.E. (2010) 'Exploring the conformation-regulated function of titin kinase by mechanical pump and probe experiments with single molecules', *Angewandte Chemie International Edition*, Vol. 49, No. 6, pp.1147–1150.

15 Samiee, K., Foquet, M., Guo, L., Cox, E. and Craighead, H. (2005) 'Lambda-repressor oligomerization kinetics at high concentrations using fluorescence correlation spectroscopy in zero-mode waveguides', *Biophysical Journal*, Vol. 88, No. 3, pp.2145–2153.

16 Levene, M.J., Korlach, J., Turner, S.W., Foquet, M., Craighead, H.G. and Webb, W.W. (2003) 'Zero-mode waveguides for single-molecule analysis at high concentrations', *Science*, Vol. 299, No. 5607, pp.682–686.

17 Miyake, T., Tanii, T., Sonobe, H., Akahori, R., Shimamoto, N., Ueno, T., Funatsu, T. and Ohdomari, I. (2008) 'Real-time imaging of single-molecule fluorescence with a zero-mode waveguide for the analysis of protein− protein interaction', *Analytical Chemistry*, Vol. 80, No. 15, pp.6018–6022.

18 Samiee, K.T., Moran-Mirabal, J.M., Cheung, Y.K. and Craighead, H.G. (2006) 'Zero mode waveguides for single-molecule spectroscopy on lipid membranes', *Biophysical Journal*, Vol. 90, No. 9, pp.3288–3299.

19 Moran-Mirabal, J.M., Torres, A.J., Samiee, K.T., Baird, B.A. and Craighead, H.G. (2007) 'Cell investigation of nanostructures: zero-mode waveguides for plasma membrane studies with single molecule resolution', *Nanotechnology*, Vol. 18, No. 19, p.195101.

20 Eid, J., Fehr, A., Gray, J., Luong, K., Lyle, J. and Turner, S. (2009) 'Real-time DNA sequencing from single polymerase molecules', *Science*, Vol. 323, No. 5910, pp.133–138.

21 Rigneault, H., Capoulade, J., Dintinger, J., Wenger, J., Bonod, N., Popov, E., Ebbesen, T. and Lenne, P-F. (2005) 'Enhancement of single-molecule fluorescence detection in subwavelength apertures', *Physical Review Letters*, Vol. 95, No. 11, pp.117401.

22 Foquet, M., Samiee, K.T., Kong, X., Chauduri, B.P., Lundquist, P.M., Turner, S.W., Freudenthal, J. and Roitman, D.B. (2008) 'Improved fabrication of zero-mode waveguides for single-molecule detection', *Journal of Applied Physics*, Vol. 103, No. 3, p.034301.

23 Korlach, J., Marks, P.J., Cicero, R.L., Gray, J.J., Murphy, D.L., Roitman, D.B., Pham, T.T., Otto, G.A., Foquet, M. and Turner, S.W. (2008) 'Selective aluminum passivation for targeted immobilization of single DNA polymerase molecules in zero-mode waveguide nanostructures', *Proceedings of National Academy of Science USA*, Vol. 105, No. 4, pp.1176–1181.

24 Zhu, P. and Craighead, H.G. (2012) 'Zero-mode waveguides for single-molecule analysis', *Annual Review of Biophysics*, Vol. 41, No. 1, pp.269–293.

25 Szklarska-Smialowska, Z. (1999) 'Pitting corrosion of aluminum', *Corrosion Science*, Vol. 41, No. 9, pp.1743–1767.

26 Vargel, C. (2004) *Corrosion of Aluminium*, Elsevier, Amsterdam.

27 Han, G., Weber, D., Neubrech, F., Yamada, I., Mitome, M., Bando, Y., Pucci, A. and Nagao, T. (2011) 'Infrared spectroscopic and electron microscopic characterization of gold nanogap structure fabricated by focused ion beam', *Nanotechnology*, Vol. 22, No. 27, p.275202.

5 Placing Individual Molecules in the Center of Nanoapertures

Nanophotonic devices for biological purposes usually make use of light-metal interactions to concentrate field energy and then employ fluorescent labels in order to generate signals within these hot-spots. But, as discussed in chapter 2.2, the presence of metal also brings about undesired, non-fluorescent, deexcitation channels that decrease the quantum yield and quench fluorescence intensity. Roughly, these two effects - enhancement and quenching - are strongest with molecular contact to the metal and decay within the distance of the light's wavelength [44]. This results in strong signal-inhomogeneities of fluorophores immobilized within metal based nanophotonic devices. Thus, in experiments where comparative signal strengths are advantageous or even prerequisites, the desire is raised to actively place probes at reproducible positions within nanophotonic devices rather than to distribute them stochastically.

The advantage of ZMWs – used commercially or non-commercially - lie in their massively parallel usage. So for ZMWs, active placement is even more important because their yield decreases dramatically with stochastic immobilization as then not only signal intensity but also single-occupation are governed by Poissonian statistics.

In this chapter the development of a new method used to place single fluorescent molecules in the center of ZMWs is presented. This method is based upon the previously described experiences with force spectroscopy in ZMWs and realized by combining optical superresolution localization and SMC&P. To demonstrate the capability of this placing method, it is used to probe the fluorescence properties within nanoapertures which, so far, have only been characterized in spatial ensemble measurements (see chapter 2.2). These results are compared to data from stochastically immobilized probes and, in combination, give a first picture on the spatial heterogeneity of the electrodynamic environment inside ZMWs. Generally, both aims - loading and probing - of this refined SMC&P method, can be applied to other biophotonic devices such as nanoantennas or nanoparticle-based assays.

5.1 Summary of Associated Publication P3

The apertures used in publication P3 were fabricated according to an e-beam lithography recipe that was developed within this study. It is described in the supplementary information (SI) of P3 and was discussed in chapter 2.2. The properties of these nanoaptertures are good reproducibility, vertical sidewalls and uncontaminated glass bottom surfaces. This new fabrication method was necessary as these three properties are prerequisites to allow comparability of fluorescence spectroscopy results to theory and other experiments; e.g. gallium ion contaminations from FIB-milling would be a source for quenching not associated with intrinsic ZMW properties.

For similar reasons, an elaborate functionalization recipe was developed for this study and is described in the SI of P3. It combines aluminum specific passivation and silane chemistry to allow the restriction of PEG-Biotin binding sites to the apertures' bottoms. These protocols were optimized towards minimizing of unspecific binding, corrosion and contamination. In the case of SMC&P, depots and target areas were functionalized with a microfluidic system or, alternatively, with a microspotter.

To investigate their fluorescence properties, double-stranded DNA oligos labeled with ATTO647N dyes were immobilized in nanoapertures of different sizes from solution and via avidin-biotin binding. Then, confocal fluorescence lifetime imaging was used to record the spectral properties of the dyes. Multiple occupation of apertures was minimized through a low overall occupation density, and apertures showing more than one single bleaching step in transient curves recorded after the scans were excluded from data analysis. For the latter, a deconvolution software was used to resolve fluorescence lifetimes below 1 ns.

More than 1300 single molecules in nanoapertures were recorded and analyzed. And although this method is very elaborate compared to e.g. FCS measurements in one single ZMW, the characterization of stochastically distributed molecules represents a first unaveraged insight into the electrodynamic environment of the experimentally interesting ZMW-bottom:

As to fluorescence lifetime, all aperture diameters show quenched lifetimes, but for smaller diameters the occurrence probability of unquenched lifetimes decreases. This leads to the interpretation that the apertures' centers experience least lifetime quenching, and it agrees with the basic picture in which lifetime quenching decreases with increasing fluorophore-metal distance.

The data also shows that most of the dyes in nanoapertures have quenched intensities i.e. smaller than the average intensity of dyes measured on a metal-free glass reference surface. However, for all aperture diameters some dyes were also recorded that had increased intensities of up to 3-fold. This is evidence for regions where metallic field enhancement exceeds metallic quenching. As the probes with highest intensities also have the longest lifetime, this points towards the central region of the apertures – furthest away from quenching metal – to be the location where the highest intensities occur.

These heterogeneities demonstrate the potential benefit from a site-specific loading-technique.

For this, we refined SMC&P: We implemented a custom fit software into an hybrid AFM-TIRF microscope which, in addition, included a confocal microscope with a pulsed laser for lifetime recordings. The software was equipped with Gaussian fitting routines able to localize the position of the cantilever tip as well as the nanoapertures in camera images.

As it is a Poissonian process to functionalize a tip with only one active transport handle, the position of that handle within the tip radius is also statistically distributed and by no means restricted to the very center of the tips axis. So, to localize the active handle, we localized a pasted reference dye rather than the tip. The subsequent localization of a nanoaperture visible from extraordinary transmission revealed both positions within the optical coordinate system of the camera and allowed the alignment of cantilever and aperture by piezo-driven movement of the sample stage.

To minimize inaccuracies, localization procedures were done quickly and with automated routines to cope with drift. Also, absolute movements were minimized to reduce the influence of inaccuracies in the transformation matrices relating the optical and the piezo coordinate system. The overall lateral inaccuracy of the procedure was estimated to be ±19 nm (see SI of P3).

The proof-of-principle results for this method consist of a 130 nm ZMW which is loaded with a single molecule as proven by single step bleaching and by a single force rupture event. Furthermore, 400 nm diameter apertures were loaded with single probes whose fluorescence lifetime and intensity were recorded in confocal scans. Lifetime and intensity of the probes ranged in the unquenched region of the stochastically placed probes revealing that the central position within the apertures is indeed that of maximum lifetime and intensity. This, in turn, validates the expected benefit from SMC&P based loading of ZMWs.

5.2 Associated Publication P3

Placing individual molecules in the center of nanoapertures

by

Stephan F. Heucke, Fabian Baumann, Guillermo P. Acuna, Philip M. D. Severin, Stefan W. Stahl, Mathias Strackharn, Ingo H. Stein, Philipp Altpeter, Philip Tinnefeld and Hermann E. Gaub

submitted to

Nature Photonics

2013

Placing individual molecules in the center of nanoapertures

Stephan F. Heucke[1], Fabian Baumann[1], Guillermo P. Acuna[2], Philip M. D. Severin[1], Stefan W. Stahl[1], Mathias Strackharn[1], Ingo H. Stein[1], Philipp Altpeter[1], Philip Tinnefeld[2*] & Hermann E. Gaub[1]

Optical spectroscopy of single enzymes provides unique insights into their activity but, at the same time, requires sophisticated means to cope with the high label concentrations needed. A prominent approach to overcome the concentration limitation is the placement of molecules in photonic devices called zero-mode waveguides (ZMWs)[1,2], which are also commercially used for single-molecule DNA sequencing[3]. However, both intensity and fluorescence lifetime in these metallic nanoapertures strongly depend on the precise location of the fluorophore with respect to the metallic walls. Here, we investigated this heterogeneity by placing single fluorescent molecules in ZMWs - first in a stochastic then in a controlled manner. We advanced the recently developed single-molecule cut-and-paste technique[4] by superresolution routines for pasting individual fluorophores into the center of nanoapertures. The greatly reduced heterogeneity compared to stochastic immobilization demonstrates our technique's nanometer accuracy while additionally providing a picture of spatial differences in the electrodynamic environment of ZMWs.

Zero-mode waveguides (ZMWs) are nanoapertures in opaque metallic films with diameters below cut-off i.e. smaller than approximately half the wavelength of the incident light. The resulting strong confinement of the excitation light to an evanescent field at the apertures' bottom results in observation volumes more than three orders of magnitude smaller than a diffraction-limited laser focus[2]. With standard nanolithography allowing their mass production[5], ZMWs became the flagship of commercialized nanophotonic single-molecule technology. The fast and unambiguous optical read-out of single ligand binding events led to the direct observation of translation[6] and even allowed epigenetic DNA sequencing[7]. In these applications, enzymes were immobilized from solution resulting in a low yield of ZMWs with only one immobilized enzyme. By this stochastic immobilization, single-occupancy can be maximized to a theoretical Poissonian limit of only 37%[8]. In addition, the fluorescence signal intensities are expected to vary strongly, due to the randomly distributed distances of the immobilized enzymes to the fluorescence quenching metallic sidewalls. This further reduces the fraction of ZMWs that can be used for analysis and drastically limits the breadth of quantitative spectroscopic measurements of biomolecular processes.

To characterize the fluorescence properties of individual fluorophores in nanoapertures, single molecules of double-stranded DNA labeled with one ATTO647N dye were, in a first set of experiments, stochastically immobilized in the nanoapertures using passivated metal walls and biotin-neutravidin interaction on the pegylated bottom of the nanoapertures[3,8] (Fig. 1a and SI). By confocal fluorescence lifetime imaging[9], we quantified fluorescence intensities and fluorescence lifetimes. Fig. 1b shows a false-color fluorescence image of single molecules in 150 nm nanoapertures. In an additional background channel, shown in green, we recorded reflection from the metal cladding and leakage through the dichroic filter to make nanoapertures visible as a dim regular grid. The red spots of different intensity in some of the nanoapertures represent fluorescence from immobilized DNA molecules labeled with ATTO647N. The density of fluorophores was kept low to reduce the probability of multiple occupancies. Additionally, single-step photobleaching in fluorescent transients recorded for the brightest spots, such as those depicted in Fig. 1c, confirmed that the fluorescence, indeed, can be ascribed to single fluorophores. The different intensity of the fluorescent spots already suggests substantial heterogeneity. This is further characterized in probability density maps correlating fluorescence intensity and fluorescence lifetime of more than 1700 dyes immobilized in different size nanoapertures and on a glass reference surface (Fig. 1d). For all nanoapertures the fluorescence lifetime was shorter than that of the glass reference. For all aperture sizes a population of strongly quenched fluorescence lifetimes close to the time resolution of the setup is observed which extends to longer lifetimes to a degree that depends on the nanoaperture size. Interestingly, the fluorescence intensity normalized to the mean fluorescence intensity of the glass reference (termed relative intensity) is not proportionally correlated with the fluorescence lifetime. While the spots with the short lifetimes exhibit weak fluorescence, some of the molecules with intermediate lifetimes display even stronger fluorescence than the glass reference. The interaction between fluorophores and metallic structures has been

[1] Center for Nanoscience and Department of Physics, University of Munich, Amalienstrasse 54, 80799 Munich, Germany, [2] Physical and Theoretical Chemistry - NanoBioScience, TU Braunschweig, Hans-Sommer-Strasse 10, 38106 Braunschweig, Germany; * e-mail: p.tinnefeld@tu-bs.de

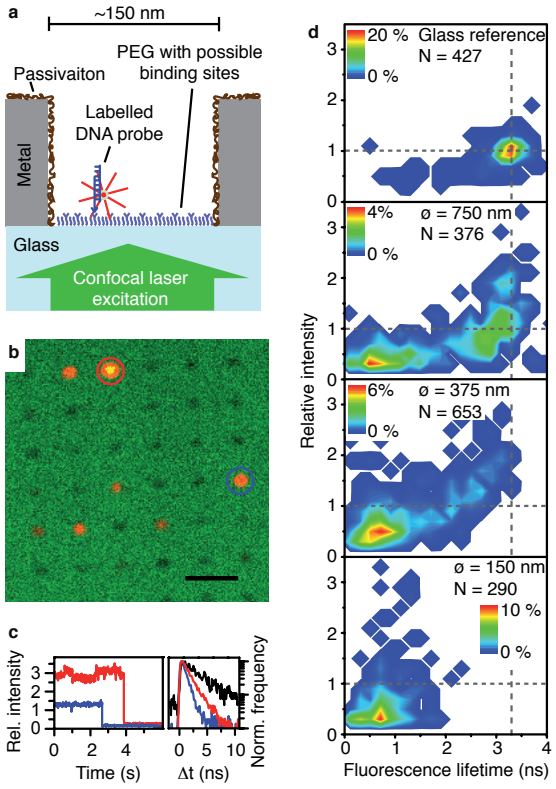

Fig. 1| Fluorescence heterogeneity from stochastic immobilization. a, Schematics of the experiment. Dye-labeled double-stranded DNA from solution is immobilized via biotin-avidin binding on a PEG layer that is restricted to the aperture's bottom by chemical passivation. **b**, A false color confocal microscopy image of an array of ZMWs with diameters of 150 nm. The black bar represents 2 µm. ZMWs are visible as dark minima in a background channel (green). A low overall occupation density of the dyes (red), together with single-step bleaching in fluorescence transients assures single-dye occupation of the ZMWs. **c**, Transients and fluorescence decay times Δt are plotted for two exemplary dyes (red and blue circles in **b**). The intensity of the transients is normalized to the mean intensity of a population of reference dyes that were immobilized in a large glass window without metal. For comparison, the fluorescence decay time of one reference dye is graphed in black. **d**, Lifetime and intensity data from N number of dyes immobilized in a large glass reference window and in different diameter apertures are plotted in probability maps. Dyes in apertures reveal pronounced heterogeneity in fluorescence lifetime and an up to threefold intensity enhancement compared to dyes immobilized on a glass reference. The longest fluorescence lifetime measured decreases for smaller nanoapertures.

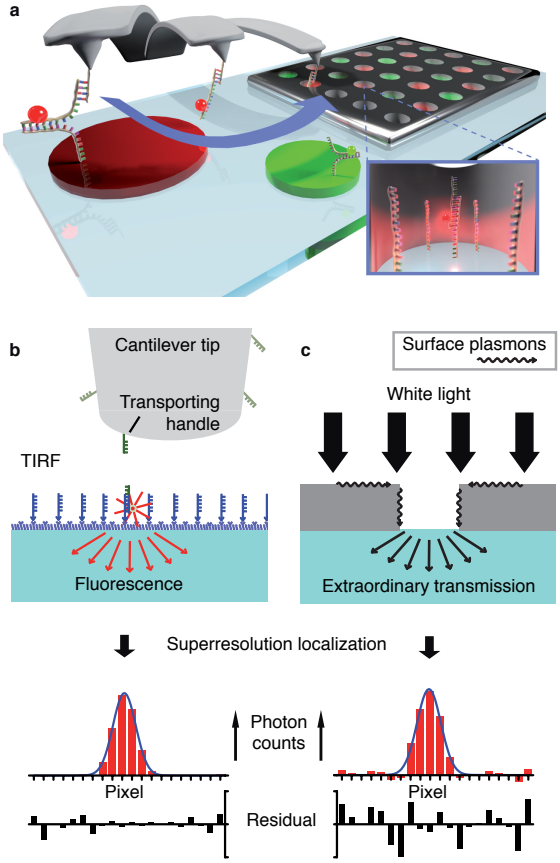

Fig. 2| Principle of Cut-and-Paste in nanoapertures. a, Schematics of single-molecule cut-and-paste into nanoapertures. An AFM cantilever is used to transport labeled DNA anchors from a remote depot area into the center of a nanoaperture. **b**, The position of the AFM's transporting handle is localized by fitting Gaussians to the fluorescence of a pasted anchor in TIRF-microscopy mode. **c**, Similarly, white light extraordinarily transmitted through the nanoaperture by surface plasmons is used to localize the apertures by Gaussian fitting of the intensity distribution.

theoretically studied for simple geometries such as mirrors[10] and spheres[11], whereas for more complex geometries such as nanoapertures numerical simulations have been employed[1,12]. Metals can modify all defining rates of a fluorophore (i.e. excitation, radiative and non-radiative) leading to an enhancement or to a reduction of the fluorescence intensity[9]. Metals generally shorten the fluorescence lifetime, particularly in close vicinity to the metallic surface where the increase of the non-radiative rate prevails[13]. Fluorescence enhancement was, for example, reported for dyes diffusing through nanoapertures in gold[14] and in aluminum films[15], but little information[16] on spatial distributions or correlation of lifetime and intensity was reported.

In order to overcome the heterogeneity and to assign the fluorescence lifetimes to positions in the nanoapertures, we adapted atomic force microscopy (AFM) based single-molecule cut-and-paste (SMC&P)[4] to the needs of placing into nanoapertures. We used the cantilever of an AFM as a nanoscopic robotic arm for loading nanoapertures and DNA oligos as programmable handles and anchors (see Fig. 2a). In previous studies, single molecules such as DNA[4,17], avidin binding sites[18], functional aptamers[19] or whole proteins[20]

were deposited with a precision relative to one another of ~11 nm[17]. This approach should not only overcome the Poissonian occupation limit but should also enable signal homogenization and maximization by restricting molecule immobilization to the nanoapertures' center.

A prerequisite for pasting molecules into nanoapertures is to align both the position of the handle DNA oligo on the AFM tip and the position of the nanoapertures with the microscope optics. Since the functionalization of the AFM cantilever tip is a stochastical process where only the functionalization density is controlled and kept within the Poisson limit, those cantilevers are selected which have one active handle only, but the position of this handle is not known a priori. To localize this active handle oligo on the AFM tip we first picked up an individual DNA oligo with its fluorophore from the depot area and then pasted it in a large reference window next to the nanoapertures. Its localization by Gaussian fitting the point-spread function yields the position of the active SMC&P handle on the AFM tip in the coordinate system of the optical microscope with the precision of a few nanometers[21] (Fig. 2b). To localize the target nanoaperture, we made use of extraordinary transmission through the sub-wavelength apertures – a phenomenon first discovered by Ebbesen and co-workers[22]. The transmitted light allows localization of the aperture by a Gaussian fit to its intensity distribution (Fig. 2c). Since both positions are defined by this procedure with nanometer precision in the coordinate system of the optical microscope, individual DNA oligos may now be pasted at the bottom of the nanoapertures. In contrast to AFM topography scans, this procedure is fast and noninvasive since it does not impair the activity of the handle DNA on the cantilever through mechanical contact. The lateral precision of our method was determined to be 19 nm (see Supplementary Information for a detailed error analysis).

The detected light intensity during the loading of a 130 nm nanoaperture is shown in Fig. 3a and b (see also: Supplementary Movie). Initially, the targeted nanoaperture (red arrow) has been aligned with the AFM and is visible by transmitted white light. After the white light is switched off the nanoaperture is loaded with a single DNA strand. The high signal at the beginning of the paste event (stage iii)) originates from inelastic scattering of the cantilever's tip[17]. After it is withdrawn, fluorescence from the DNA strand's label remains until it bleaches in a single step. In combination with the single rupture event in the simultaneously recorded force curve of the paste (Fig. 3c), this single photobleaching step proofs single-molecule occupancy. Assuming 100% interaction efficiency and minimized fluorescence acquisition times, the duration of

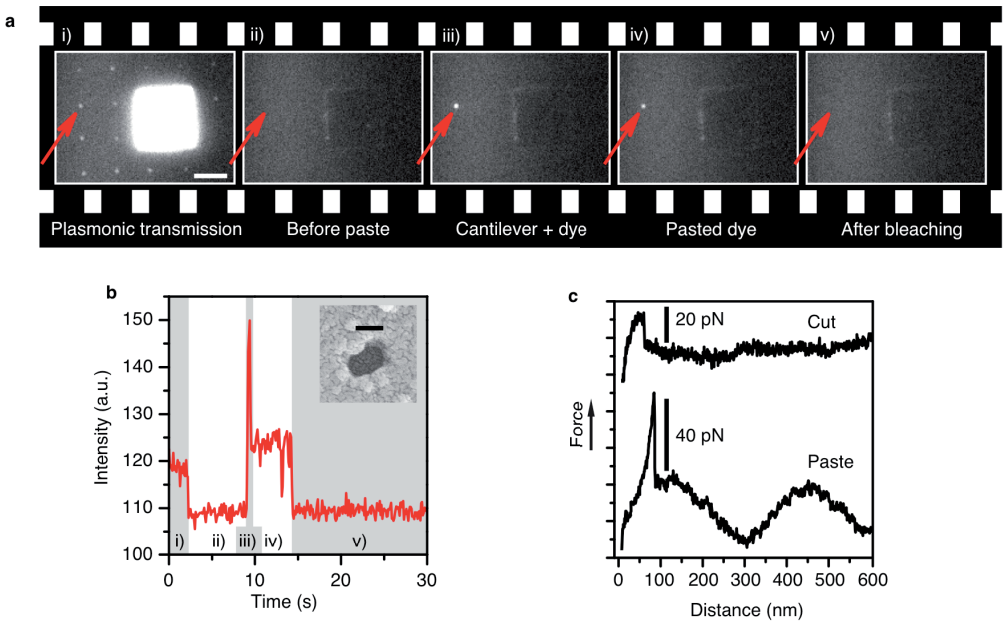

Fig. 3| Single dyes placed in nanoapertures with SMC&P. a,**b**, Video frames (**a**) documenting the pasting of a single dye into a 130 nm nanoaperture and the corresponding intensity transient from the aperture (**b**) show five phases: i) first, extraordinary transmission reveals the position of the aperture about to be loaded (red arrow). ii) Before the pasting event transmitted light is switched off and none of the nanoapertures show fluorescence under TIRF illumination. iii) Scattered light from the cantilever tip and dye fluorescence mark the pasting event. iv) After the cantilever has retracted, the fluorescence signal of a single dye remains before it bleaches in one step bringing the intensity back to background level (v). The inset in the intensity transient is a SEM-image of the actual nanoaperture loaded (bar = 100 nm). The white bar in frame i) represents 3 mm. **c**, Force curves recorded during the cut-and-paste processes show characteristic one-step zipper- (cut) and shear-force (paste) rupturing, respectively. The sine superimposing the paste force curve originates from interference of the AFM's IR-laser with the reflective metal surrounding the ZMW.

3

one loading cycle is limited by the travelling and pulling speeds of the AFM to about 3 s. It should be noted here that after bleaching of the label, the pasted DNA strand may be used as anchor point for other molecules of interest in the center of the nanoaperture.

Besides the abilities of TIRF imaging for synchronization and SMC&P, our setup incorporates a confocal microscope for fluorescence lifetime imaging. This enabled us to carry out SMC&P, to visualize successful pasting in the nanoapertures and to subsequently switch to the confocal mode for single-molecule spectroscopy of the same molecules. We extracted the fluorescence lifetime by reconvoluting with the instrument response function and quantify the fluorescence intensities by normalizing to the intensities of dye molecules pasted in metal free areas (see Supplementary Information for experimental section).

With this protocol, individual fluorophores were pasted into nanoapertures of 375 nm diameter. Fluorescence lifetimes were found in a range around 3 ns close to the maximum of the distribution obtained by stochastic immobilization (see Fig. 4, red data points). The narrow fluorescence lifetime distribution suggests that all molecules are successfully pasted close to the center of the nanoapertures. Furthermore, the lifetime of ~ 3 ns in the center of the nanoapertures is consistent with the interpretation that the central region experiences least quenching. Interestingly, the fluorescence intensity is mostly higher than that of the glass reference in accordance with the distribution of stochastically immobilized molecules (see Fig. 4).

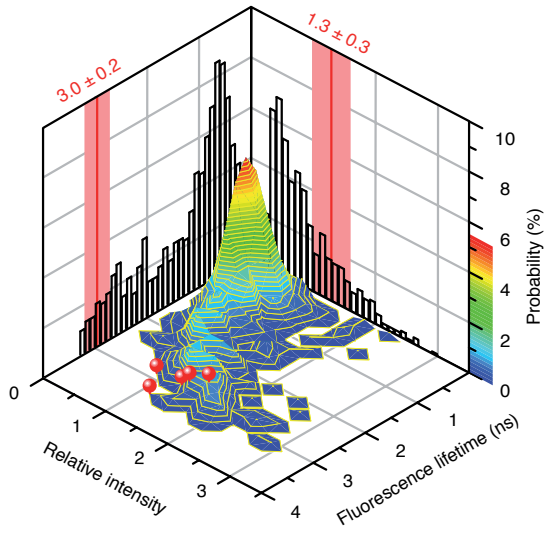

Fig. 4| Comparison of SMC&P-placed and stochastically immobilized dyes. The broad distribution of lifetimes and relative intensities from 653 dyes stochastically immobilized in nanoapertures of 375 nm is presented in the 3D probability plot and the corresponding histograms (black). In contrast, lifetime and intensity of dyes pasted into the center of same-size nanoapertures are confined to long lifetimes and enhanced relative intensity (red balls on the 3D plot). Their mean and standard deviation are represented by the red lines and boxes in the histograms

Our study shows that stochastic immobilization of molecules in nanoapertures results in a pronounced heterogeneity of fluorescence properties with a high fraction of strongly quenched molecules. We advanced single-molecule cut-and-paste technology to overcome these limitations using a superresolution-based optical navigation technique. Analysis of quantitative confocal single-molecule imaging revealed that the brightest molecules are found near the center of the nanoapertures and that quenching scales with the proximity of the metal walls. Our data indicate that targeted placing of single molecules, using an approach that is not Poisson-limited, is a key for optimizing single-molecule spectroscopy in nanoapertures. Immobilization of other kinds of molecules, such as different enzymes from multiple depots, can open new routes for parralleled single-molecule assays. The site-specific one-by-one immobilization of single molecules can generally facillitate probing of the electromagnetic environment of other nanostructures such as the coupling of optical emitters to antennas[23].

Methods

Nanoapertures were fabricated on conventional glass cover slips using negative e-beam lithography. A detailed recipe based on a fabrication method by Foquet et al.[5] is given in the SI. To functionalize the samples for SMC&P we adapted our previously published protocols[4,19] to the needs of the partially metallic surfaces and implemented steps to selectively passivate the aluminum with polyvinylphosphonic acid as described in Ref. 8. To allow comparison of spectroscopic data from stochastically immobilized probes with those placed by SMC&P, we used the same labeled DNA constructs in both experiments. DNA sequenches and further details on sample preparation protocols, procedures of the experiments and the custom-built microscopes they were performed on are given in the SI Text.

References:

1 Levene, M. J. *et al.* Zero-mode waveguides for single-molecule analysis at high concentrations. *Science* **299**, 682-686 (2003).
2 Zhu, P. & Craighead, H. G. Zero-mode waveguides for single-molecule analysis. *Annu. Rev. Biophys.* **41**, 269-293, doi:10.1146/annurev-biophys-050511-102338 (2012).
3 Eid, J. *et al.* Real-time DNA sequencing from single polymerase molecules. *Science* **323**, 133-138 (2009).
4 Kufer, S. K., Puchner, E. M., Gumpp, H., Liedl, T. & Gaub, H. E. Single-molecule cut-and-paste surface assembly. *Science* **319**, 594-596 (2008).
5 Foquet, M. *et al.* Improved fabrication of zero-mode waveguides for single-molecule detection. *J. Appl. Phys.* **103**, 034301, doi:10.1063/1.2831366 (2008).
6 Uemura, S. *et al.* Real-time trna transit on single translating ribosomes at codon resolution. *Nature* **464**, 1012-1017, doi:10.1038/nature08925 (2010).
7 Flusberg, B. A. *et al.* Direct detection of DNA methylation during single-molecule, real-time sequencing. *Nat. Methods* **7**, 461-465, doi:10.1038/nmeth.1459 (2010).

8 Korlach, J. *et al.* Selective aluminum passivation for targeted immobilization of single DNA polymerase molecules in zero-mode waveguide nanostructures. *Proceedings of the National Academy of Sciences* **105**, 1176-1181 (2008).
9 Acuna, G. P. *et al.* Fluorescence enhancement at docking sites of DNA-directed self-assembled nanoantennas. *Science* **338**, 506-510, doi:10.1126/science.1228638 (2012).
10 Drexhage, K. H. Interaction of light with monomolecular dye layers. *Prog. Optics* **12**, 163-232, doi:10.1016/S0079-6638(08)70266-X (1974).
11 Gersten, J. & Nitzan, A. Spectroscopic properties of molecules interacting with small dielectric particles. *J. Chem. Phys.* **75**, 1139-1152, doi:10.1063/1.442161 (1981).
12 Fore, S., Yuen, Y., Hesselink, L. & Huser, T. Pulsed-interleaved excitation FRET measurements on single duplex DNA molecules inside c-shaped nanoapertures. *Nano Lett.* **7**, 1749-1756, doi:10.1021/nl070822v (2007).
13 Anger, P., Bharadwaj, P. & Novotny, L. Enhancement and quenching of single-molecule fluorescence. *Phys. Rev. Lett.* **96**, 113002, doi:10.1103/PhysRevLett.96.113002 (2006).
14 Wenger, J. *et al.* Emission and excitation contributions to enhanced single molecule fluorescence by gold nanometric apertures. *Opt. Express* **16**, 3008-3020 (2008).
15 Wenger, J. *et al.* Radiative and nonradiative photokinetics alteration inside a single metallic nanometric aperture. *J. Phys. Chem. C* **111**, 11469-11474, doi:10.1021/jp0726135 (2007).
16 Choy, J. T. *et al.* Enhanced single-photon emission from a diamond–silver aperture. *Nature Photon.* **5**, 738-743, doi:10.1038/nphoton.2011.249 (2011).
17 Kufer, S. K. *et al.* Optically monitoring the mechanical assembly of single molecules. *Nat. Nanotechnol.* **4**, 45-49, doi:10.1038/nnano.2008.333 (2008).
18 Puchner, E. M., Kufer, S. K., Strackharn, M., Stahl, S. W. & Gaub, H. E. Nanoparticle self-assembly on a DNA-scaffold written by single-molecule cut-and-paste. *Nano Lett.* **8**, 3692-3695 (2008).
19 Strackharn, M., Stahl, S. W., Puchner, E. M. & Gaub, H. E. Functional assembly of aptamer binding sites by single-molecule cut-and-paste. *Nano Lett.* **12**, 2425-2428, doi:10.1021/nl300422y (2012).
20 Strackharn, M., Pippig, D. A., Meyer, P., Stahl, S. W. & Gaub, H. E. Nanoscale arrangement of proteins by single-molecule cut-and-paste. *J. Am. Chem. Soc.* **134**, 15193-15196, doi:10.1021/ja305689r (2012).
21 Thompson, R. E., Larson, D. R. & Webb, W. W. Precise nanometer localization analysis for individual fluorescent probes. *Biophys. J.* **82**, 2775-2783 (2002).
22 Ebbesen, T. W., Lezec, H. J., Ghaemi, H. F., Thio, T. & Wolff, P. A. Extraordinary optical transmission through sub-wavelength hole arrays. *Nature* **391**, 667-669 (1998).
23 Novotny, L. & van Hulst, N. Antennas for light. *Nature Photon.* **5**, 83-90, doi:10.1038/nphoton.2010.237 (2011).

Acknowledgements:

The authors would like to thank A. Meindl, S. Schneider, A. Vetter and W. Summerer for technical support and C. Hohmann for artwork. This work was supported by the Volkswagen Stiftung, the German Science Foundation (SFB 863) and the German excellence initiative via the "Nanosystems Initiative Munich" (NIM). S.H. is grateful to the Elite Network of Bavaria (IDK- NBT) for a doctoral fellowship.

Author contributions:

S.H., P.T. and H.G. conceived and designed the experiments and co-wrote the paper. S.H., F.B., G.A. and P.A. fabricated the samples. S.H., F.B., P.S. and M.S. functionalized the samples. S.H., F.B., I.S. and G.A. conducted the stochastic experiments. S.H., F.B., S.S. and M.S. performed the SMC&P experiments. S.H., F.B. and I.S. analyzed the data. All authors discussed the results and commented on the manuscript.

Additional information:

The authors declare no competing financial interests.

5.3 Supporting Information for Associated Publication P3

Supplementary Information for: Placing individual molecules in the center of nanoapertures

by

Stephan F. Heucke, Fabian Baumann, Guillermo P. Acuna, Philip M. D. Severin, Stefan W. Stahl, Mathias Strackharn, Ingo H. Stein, Philipp Altpeter, Philip Tinnefeld and Hermann E. Gaub

submitted to

Nature Photonics

2013

Supplementary information

Placing individual molecules in the center of nanoapertures

Stephan F. Heucke[1], Fabian Baumann[1], Guillermo P. Acuna[2], Philip M. D. Severin[1], Stefan W. Stahl[1], Mathias Strackharn[1], Ingo H. Stein[1], Philipp Altpeter[1], Philip Tinnefeld[2*] & Hermann E. Gaub[1]

[1] Center for Nanoscience and Department of Physics, University of Munich, Amalienstrasse 54, 80799 Munich, Germany
[2] Physical and Theoretical Chemistry - NanoBioScience, TU Braunschweig, Hans-Sommer-Strasse 10, 38106 Braunschweig, Germany
* e-mail: p.tinnefeld@tu-bs.de

Lithography of nanoapertures

For loading nanoapertures via SMC&P, samples have to contain nanoapertures, a glass window for the depot area as well as a second, smaller glass window for the reference pastes – all within reach of the AFM cantilever. Fig. S1 depicts the structural arrangement used in the underlying experiments. Samples were fabricated with negative e-beam lithography based on a method described in ref. 1. However, we used an alternative photoresist and a discharge layer consisting of silver instead of gold:

Initial cleaning: Conventional borosilicate glass cover slips were first cleared from glass debris by a nitrogen stream and then excessively cleaned in solvents: They were immersed in an ultrasonic (US) bath (Super Digital, Bandelin Sonorex) of 2% Hellmanex at 50 °C for 15 min followed by a rinse with water (all water used during lithography was purified and of HPLC grade), a 15 min US-bath in water and again another water rinse to wash away any Hellmanex remains. Further subsequent 15 min US-baths in acetone, isopropanol and water additionally assured removal of any organic contaminations. Finally, samples were again rinsed in water and then dried under a nitrogen stream.

Photoresist coating: To increase hydrophobicity of the glass surface, and thus promote photoresist adhesion, the cover slips were treated with an oxygen plasma (GigaEtch, PVA TePla Technics) at 200 W for 180 s and heated up to 120 °C on a hot plate for 120 s. To prevent resorption of air humidity the cover slips were then taken from the hot plate and directly placed onto a spin coater (WS-400-6NPP/LITE/IND, Laurell) where resist promoter (1:10, isopropanol : Ti-Prime, MicroChemicals) was spun onto the samples immediately. Spin coater settings were 4000 rpm for 40 s with a 3 s acceleration ramp of 800 rpm. Primer solvents were evaporated by baking the sample on a hot plate at 120 °C for 120 s. Now photoresist (ma-N 2403, Microresist) was spun onto the sample for 30 s with a 3 s ramp of 800 rpm and a final rotational speed of 3000 rpm followed by a bake at 90 °C for 60 s.

Deposition of the discharge layer: To avoid charge accumulations in the nonconducting glass substrate, a 5 nm Ag film was thermally evaporated onto the photoresist from a tungsten boat in a hybrid evaporator (Bestec) capable of e-beam and thermal evaporation. A current of 190 A at a voltage of 0.8 V resulted in a rate of 1.2 Å/s while pressure was 5×10^{-9} mbar prior to evaporation. The samples were water-cooled via physical contact on their backside to prevent heating above the critical cross-linking temperature of the photoresist resin. When evaporating Cr, Au or Al instead, we experienced cross-linking which we denote to the increased thermal radiation coming with the higher boiling points of these metals. To avoid fluctuations in oxidation degree of the Ag discharge layer, samples were transferred into the electron microscope immediately after evaporation.

Exposure: Electron beam exposure was made in an eLine system (Raith) with thermal field-emitting cathode (Schottky emitter). An acceleration voltage of 10 kV and an aperture of 20 μm resulted in a beam current of 0.074 nA. Working distance was 8 mm. Apertures with diameters smaller than 150 nm were written as single dots with a dose of 0.023 pC. Apertures with diameters of 150 nm, 375 nm and 750 nm were written as filled circles with a step size of 12.8 nm, a dose of 10 $\mu C/cm^2$. Glass windows were written with a step size of 10 nm and an area dose of 7 $\mu C/cm^2$.

Development: Samples were then heated in a post exposure bake at 72 °C on a hot plate for 120 s to increase linking of the exposed photoresist. The discharge layer was dissolved by a 7 s bath in a commercial etchant (Iodine / Potassium iodide = I2/KI, 50% aq., Alfa Aesar) followed by a stop and a rinse bath in water for 30 s each. The samples were then developed under slight stirring in ma-D 525 (Microresist) for 70 s, stopped from development in a 30 s water bath and rinsed in another water bath. As the exposed dots which later were to become apertures are free standing pillars from the developer bath on, great care was taken not to expose them to unnecessary physical stress. Thus, samples were held in a horizontal orientation with the structures facing upwards when slowly taken out of one bath and into the next. The resulting aqueous meniscus on the surface avoided stressing the pillars with surface tension. Additionally, the meniscus prevented resist remains floating in the baths from drying in on the sample. After the third and last bath, samples were held horizontally and a gentle flow of water over the surface was established with a handheld washing bottle to rinse away any resist remains. Finally, the sample was dried in a controlled manner by turning it vertical. This let the meniscus withdraw slowly due to gravitational force.

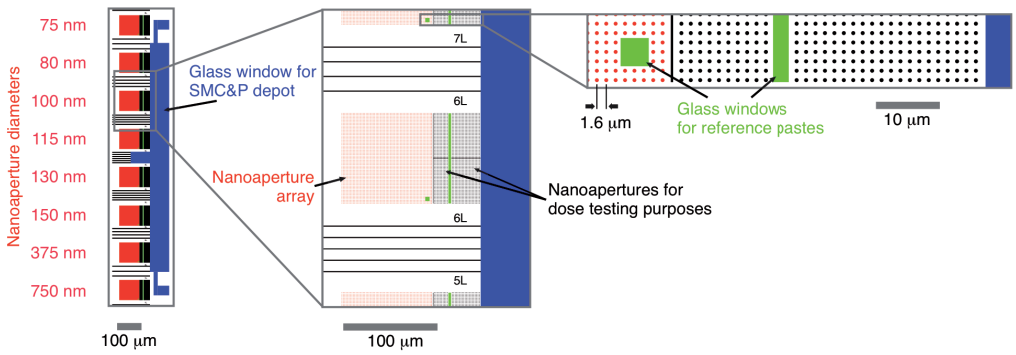

Fig. S1| Drawing of the lithography pattern. The large quadratic fields (red) are aperture arrays of different aperture diameters. The large blue vertical rectangle represents the depot glass window. In between aperture arrays and depot, dose tests were written to control the quality of our fabrication process. The small green areas are glass windows for reference pastes.

Metal deposition and lift-off: Prior to metal evaporation, descumming of the samples was performed with a 200 W oxygen plasma for 180 s. A 100 nm thick aluminum film was then evaporated onto the sample in the above mentioned evaporator but with e-beam evaporation (acceleration voltage 8.5 kV, emission current 50 mA) and a rate of 0.8 nm/s. Lift-off of the metal caps on the pillars, of the underlying resist pillars and the glass windows was done in a 5 min US-bath of 40 °C hot acetone. This was followed by 30 s baths in isopropanol and water. A final water rinse and a 120 s plasma clean cleared away possible remains of the lithography process. Samples were then stored under argon atmosphere until further use.

Characterization: Aperture diameters were measured after the experiments in the above mentioned electron microscope with a 5 nm Au layer sputtered (Sputter Coater S150B, Edwards) onto the previously cleaned samples to avoid charge accumulations in the apertures' glass bottoms (Fig. S2). AFM topography scans (Fig. S3) assured that our fabrication method resulted in steep sidewalls and a smooth glass bottom surface without resist remains. Scans were done on a commercial AFM-setup (MFP3D, Asylum Research) with a high aspect ratio cantilever probe (HART, Nanoscience Instruments) in tapping mode in air.

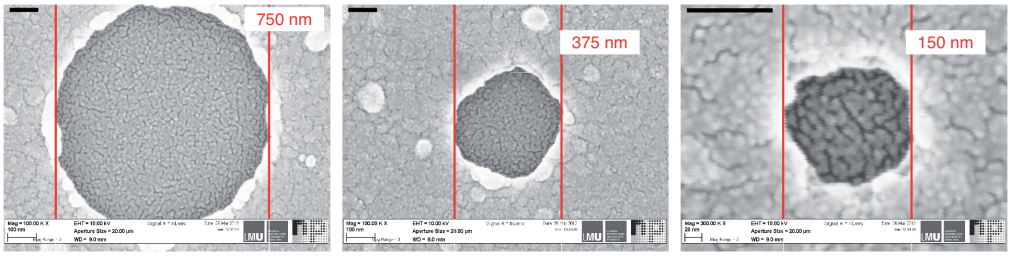

Fig. S2| SEM images of the different size nanoapertures. The fine texture in the scans originates from a 5 nm gold film sputtered onto the samples to avoid charge accumulations in the apertures' glass bottoms. The black bars in the top left corners represent 100 nm.

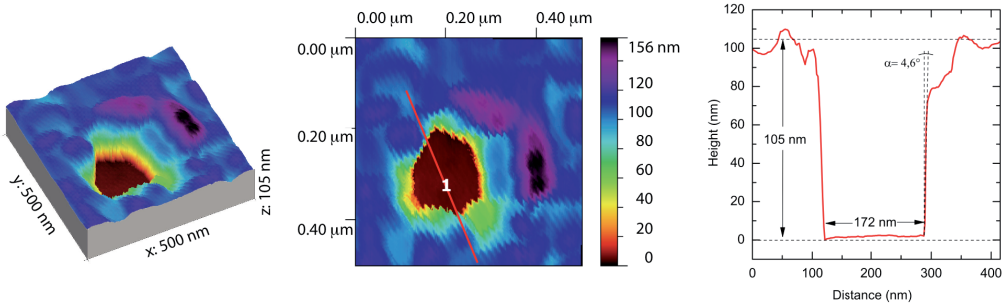

Fig. S3| AFM topography scan of a 175 nm diameter aperture. It features a smooth glass surface and steep sidewalls. The sidewall angle measured in the cross section represents the apex angle of the used high aspect ratio cantilever tip.

Surface functionalization

To achieve better comparability to the stochastically immobilized probes, depot and target DNA were not immobilized via maleimide-sulfide bonds as in previous studies, but via biotin-avidin. This high-affinity bond withstands forces that are much higher than those of the SMC&P force hierarchy[2] and no significant decrease of transport efficiencies due to DNA-PEG rupture could be observed.

Cleaning and chemically selective passivation of the aluminum surface: After the described nanolithography and storage in argon, samples were cleaned in an US-bath of pure ethanol for 1 h, rinsed under water (water used for functionalization was MilliQ water) and sonicated again in water for 15 min. They were then blown dry by a nitrogen stream and subjected to a UV-cleaner (UVOH 150 Lab, FHR) for 30 min. In the following, they were immersed into a 90 °C hot aqueous solution (2% vol/vol) of polyvinylphosphonic acid (Polysciences) for 2 min, dipped in water for 20 s and carefully rinsed under water. Samples were then baked in an oven at 80 °C for 10 min. To further wash away physisorbed PVPA and to hydrolyze PVPA still bound to the glass surface, samples were then immersed in baths of, first water for 10 min, then methanol for 5 min and again water for 5 min, on a shaker (KS 260 basic, IKA). Gentle drying was done in a stream of nitrogen.

Silanization and PEGylation: Right after passivation samples were incubated in a freshly made solution of 3-aminopropyldimethylethoxysilane (ABCR, Karlsruhe), water and ethanol (1:5:44, vol.:vol.) for one hour, dipped 10 times in each ethanol and water, and finally annealed in an 80 °C hot oven for 30 min. A freshly made 25 mM solution of NHS-PEG-biotin (3000 g/mol, Rapp) in sodium bicarbonate buffer (pH 8.3, 100 mM) was vortexed for 15 s and then centrifuged at 10,000 rpm for 30 s. Samples then were sandwiched in pairs with ZMW structures facing each other and 100 μl PEG-solution in between. After 3 hours incubation in a humid chamber, unbound PEG was washed off by 10 dips in beakers of each sodium bicarbonate buffer, water and again water. After gently drying with a nitrogen stream, samples were stored under argon until they were used in the stochastic experiments or further functionalized for SMC&P experiments, respectively.

SMC&P functionalization

Preparation of oligomeric DNA: Sequences and labels of the used commercial DNA oligos (IBA) are listed in Table S1. First, transfer and depot DNA were hybridized in a thermocycler (Mastercycler gradient, Eppendorf) by heating up the 10 μM mixture (ratio of 1:1) to 95 °C and then slowly cooling it down to 5 °C at a rate of 0.3 °C/s. Buffer was 1 × PBS. After that, neutravidin was pre-incubated with the depot/transfer-construct and the target DNA, respectively, at a concentration of 5 μM and a ratio of 1:1, also in 1 × PBS. After one hour, DNA was further diluted to 1 μM in 1 × PBS.

Application of the microfluidic system: Microfluidic polydimethylsiloxan (PDMS) channels were fabricated as described by Strackharn et al.[3]: Additionally, to reduce surface adhesion of the PDMS to the wafer and thus facilitate lift-off, the master mold wafer was exposed to perfluorodecyltrichlorosilane (97%, ABCR) vapor for 10 min before pouring the PDMS on. Also, care had to be taken to align the two channels with the target nanoapertures and the depot window,

respectively. Thus, by-eye-alignment and contact were made with a mechanical xyz-microstage and the help of a stereo microscope.

Assembly of depot and target area: Target DNA and depot/transfer-construct were then sucked into the corresponding channels by a peristaltic pump (Gilson Minipuls 3) and incubated for 15 minutes. Unbound DNA was washed away with 200 µl 1 × PBS flushed through the channels at a rate of 10 µl/min. Finally, the PDMS channels were carefully removed in a bath of 1 × PBS to prevent neutravidin from falling dry and denaturing. Samples were then mounted into a teflon sample holder and buffer was exchanged with experimental buffer (50 mM MOPS, 150 mM potassium acetate, pH 7.1). Prior to experiments, the functionalization density was checked in a fluorescence microscope (Fig. S4).

Alternative preparation with a microspotter: We also successfully used an alternative approach and prepared depot and target areas by micro-structuring the PEGylated samples via a microspotter (GIX, Sonoplot)[4]. This represents a convenient approach to prepare multiple neighboring depots with different transfer constructs within the travel range of the AFM[5]. A standard glass capillary (World Precision Instruments) with an inner diameter of 30 µm was used resulting in spots of a diameter of 45 µm to 50 µm on the cover glass (depot) and around 80 µm on the metallic surfaces containing the apertures (target). Dispenser voltage was 2.5 to 3.8 V and dispensing time was 0.1 s. A humidity chamber with a moistening feedback held the humidity at 85% to improve the coupling density of DNA strands to the sample. Alignment of sample and glass capillary was achieved via the CCD camera of the microspotter. Depot and target areas were spotted with the same DNA-solutions that were incubated in the microfluidics system, and the sample was rinsed with 3 ml 1 × PBS after 15 minutes incubation time. Coupling densities on control samples were checked with a confocal scanner, they were comparable to those achieved with the microfluidic system.

Table S1: Sequences of the partially thiolated (SH) or biotinylated DNA oligos used.

Depot	5' (Biotin) TTTTTAAGTAGCTATTCGAACTATAGCTTAAGGACGTCAA 3’
Transfer	5' TTGACGTCCTT (Atto647N) AAGCTATAGTTCGAATAGCTACTTTTTGATATCGAATTCCTGCAGTT 3’
AFM	5' SH- TTTTT CTGCAGGAATTCGATATCAA 3'
Target	5’ AAAAAGTAGCTATTCGAACTATAGCTTAAGGACGTCTTTTTTTTTT (Biotin) 3’

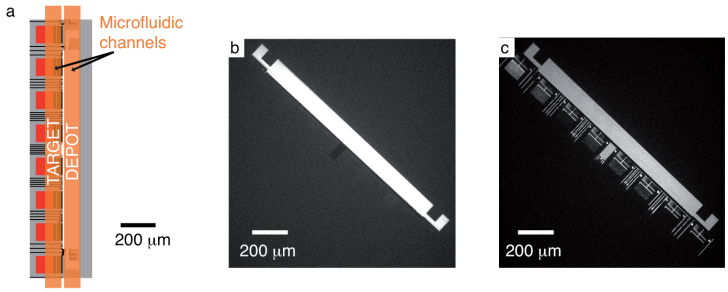

Fig. S4| SMC&P functionalization. a, Schematic drawing indicating the position and the orientation of the microfluidic channels relative to the sample structure. **b**, Fluorescence from the ATTO647N labeled transfer strand in the depot region. **c**, Fluorescence of an avidin label (Alexa Fluor 488) present in both, depot and target region.

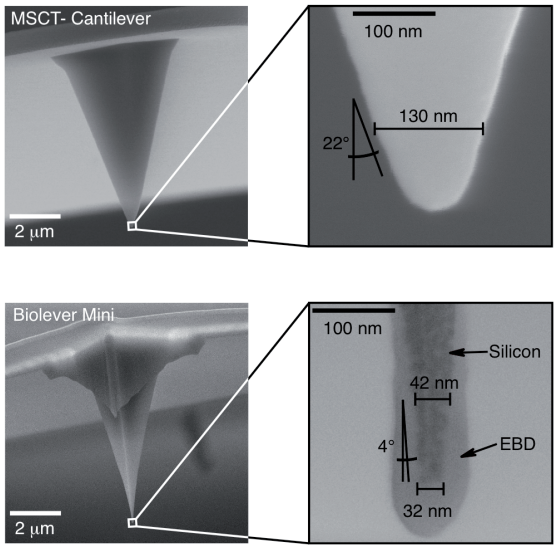

Fig. S5| SEM micrographs of the two cantilever types used in the experiments. Width and apex angle at 100 nm distance from the tips are plotted in close up. The grey layer around the silicon tip of the Biolever Mini in the close up is an artifact from SEM imaging (electron beam deposition layer, EBD) and no intrinsic part of the cantilever.

Cantilever preparation

Cantilevers were functionalized according to the recipe published in ref. 3. However, to be able to access the apertures we employed cantilevers with smaller tip radii and higher aspect ratios: Biolever Mini cantilevers (AC40TS, Olympus) with high aspect ratio silicon tips and MSCT cantilevers (Bruker) with silicon nitride tips. Their widths at a distance of 100 nm from the tip were measured by SEM (scanning electron microscopy) after sputtering them with 5 nm of Au for discharging purposes (Fig. S5). This width restricted us to use only Biolever Mini cantilevers in apertures of diameters smaller than 200 nm.

Spectroscopy of stochastically immobilized dyes

Setup: Spectroscopic measurements of stochastically immobilized fluorophores were performed on a custom-built confocal microscope as described in ref. 6. An excitation wavelength of 640 nm was selected out of the broad emission spectrum of a pulsed supercontinuum laser (800MHz, Koheras SuperK Extreme, NKT Photonics) by an acousto-optic tunable filter (AOTF, AOTFnc-VIS, AA Optoelectronic). An inverse oil immersion objective (60x, NA 1.49, Apo N, Olympus) was used for excitation as well as for the collection of the fluorescence signal. The latter was separated from the majority of reflected laser light by a double band dichroic filter (Dualband z532/633 rpc, AHF Analysentechnik). Residual reflected light passing the dichroic was then separated from the fluorescence signal by a second dichroic filter (640 DCXR, AHF) and focused onto one of the two employed avalanche photodiodes (APD, SPCM-AQR-14, Perkin Elmer). This APD was protected from fluorescence by an emission filter (Brightline HC582/75, AHF) and provided the background signal used to identify nanoapertures. The fluorescence passing both dichroic filters was finally cleaned up by two emission filters (ET-Bandpass

700/75M and RazorEdge LP 647 RU, AHF) and focused onto the second APD. Two emission filters were used for this detection channel to minimize background from metallic reflection. The detection signal was synchronized with the pulsed laser excitation and collected by a time-correlated single photon counting card (Hydra Harp 400, PicoQuant) which measures the specific lifetime Δt of each detected photon[7].

Immobilization: For comparability with SMC&P placed probes, we used a double-stranded DNA oligo consisting of Atto647N-labeled transfer and biotinylated target strand. The construct was hybridized and pre-incubated with neutravidin in the same manner as the depot construct described above. Under steady state optical control, probes were incubated until reasonable ratios of occupied apertures (~20 %) were obtained. The loading buffer was 1 × PBS and the corresponding concentrations and incubation times for the different aperture sizes were: 50 pM and 2 min for the glass reference dyes and those immobilized in 750 nm diameter apertures, 100 pM and 15 min for the 375 nm apertures and 300 pM and 25 min for the apertures with 150 nm diameters. Five consecutive buffer exchanges with experimental buffer (see next section) stopped immobilization and extracted unbound probes from the sample.

Measurement: To reduce the risk of corrosion[8], the actual confocal measurements were performed with a chloride-free experimental buffer (pH 7.1) of 50 mM MOPS, 150 mM potassium acetate, 1 mM of ascorbic acid and methylviologen. The latter two were freshly solved from powder and they served as reducing and oxidizing system (ROXS)[9] to reduce the lifetime of the non-fluorescent triplet state thus stabilizing the dyes' fluorescence signal. It is worth noting that the stochastic data presented in this work was recorded during one single experiment and performed on the same sample. The experiment started with confocal scans of the glass reference dyes immobilized in the large depot window of our sample structure. It was then proceeded with scanning of the apertures, starting with large diameters and finishing with the small ones. After all apertures of one size had been recorded, additional incubation according to the next aperture size was done before proceeding with the next set of confocal scans. After each confocal scan, the ~15% most intense dyes were additionally probed by recording a fluorescence transient. Investigation of the stepwise photobleaching in the transients allowed exclusion of data from double- or even triple-occupations.

Data analysis: The fluorescence properties of specific dyes in the confocal scans were then analyzed by custom-made software (LabView): A spot finding algorithm extracted the photons from one detected dye. The lower relative intensity threshold at which dyes were to dim to be detected was at ~20% of the mean intensity of the glass reference dyes. The amount of photons denoted to one dye directly determined its intensity. For lifetime analysis, the delay times of these photons were added up to a fluorescence decay which was fit by a commercial deconvolution software (Fluofit, PicoQuant). To achieve lifetime resolution below 1 ns, this software fits a monoexponential decay, reconvoluted with the instrument's response function (IRF), to the recorded fluorescence decays. An exemplary fluorescence decay curve with the IRF and a reconvoluted fit is shown in Fig. S6. The IRF of our confocal microscope was measured from scattered laser light, and care was taken so that the intensity during IRF-recordings was of comparable magnitude to the fluorescence intensities of the dyes. A further important advantage of the deconvolution software is that varying background scattering e.g. by the aluminum cladding of the apertures can be compensated by one fit parameter of the decay.

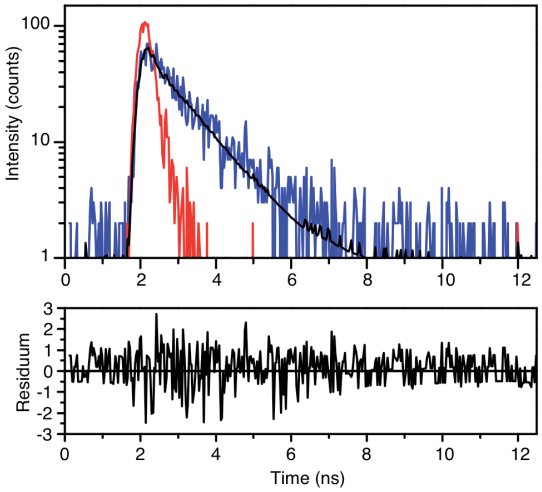

Fig. S6| Fluorescence lifetime fit. The fluorescence decay of a single fluorophore immobilized in a nanoaperture is shown in blue and the impulse response function in red. The reconvoluting fit (black) matches the fluorescence decay. The resulting residuum is shown below.

TIRF / Confocal / AFM Hybrid Microscope Setup

Loading of the nanoapertures by means of SMC&P and the consecutive lifetime measurements were performed on a custom-built setup combining atomic force microscopy with confocal as well as total internal reflection fluorescence (TIRF) microscopy. It is thus a further development of the TIRF/AFM-hybrid setup described in ref. 10. It is schematically depicted in Fig. S7.

Confocal: For the confocal part of the instrument a pulsed supercontinuum laser (Koheras SuperK Extreme, NKT Photonics), restricted to 640 nm with an AOTF (AOTFnc-VIS, AA Optoelectronic) and cleaned up by a filter (HQ 640/10, AHF), served as excitation source. The laser beam was reflected into a high numerical aperture objective (60x, NA 1.49, Apo N, Olympus) by a dichroic filter (Dualband z532/633 rpc, AHF) and focused onto the specimen. Fluorescence was collected through the same objective passed the dichroic as well as an IR-blocking filter (HC 750/SP, AHF), and was focused onto a pinhole (50 µm) by a tubus lens (U-TLU, Olympus). A system of two additional lenses (f = 150 mm, f = 25 mm) focused fluorescence light passing the pinhole onto an APD (SPCM-AQR-14, Perkin Elmer) that was protected by two fluorescence emission filters (ET-Bandpass 700/75M and RazorEdge LP 647 RU, AHF). Pulse repetition rate, photon counting system and measuring software were the same as in the confocal microscope used for the stochastic measurements. However, confocal scanning was done by movement of the objective via a xyz-piezo (Physik Instrumente).

TIRF: Switching to the combined TIRF microscope was done with two motorized flip mirrors as depicted in the schematics (Fig. S7). The TIRF laser source, a 638 nm continuous wave laser (Cube 1064915, Coherent), was cleaned up with a laser filter (BrightLine HC 636/8, AHF). Fluorescence was collected through the objective, passed the dichroic filter, was cleaned up by an emission filter (M 700/75, AHF) and focused onto an EMCCD (iXon 512x512, DU-897, Andor). The overall resolution of the TIRF-system was 102 nm/pixel. The camera chip was operated at a temperature of -75 °C and an electron multiplication gain of 300 was applied.

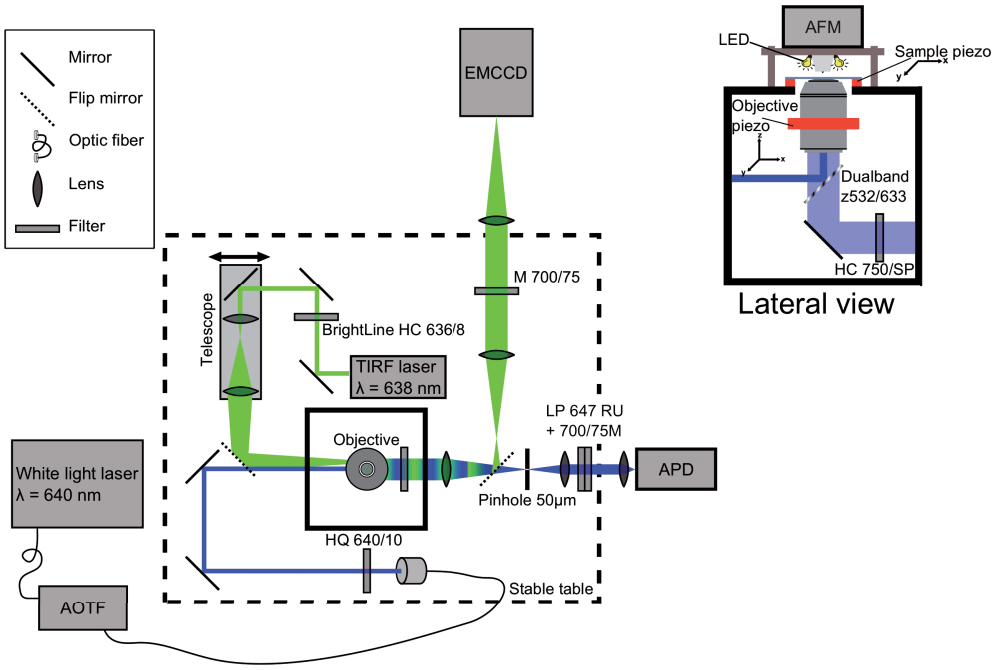

Fig. S7| Schematics of the TIRF / Confocal / AFM Hybrid Microscope Setup. The green path represents the excitation and emission in the total-internal reflection fluorescence (TIRF) microscopy mode. In blue, the path of confocal laser excitation and detection is shown. In transmission mode, laser sources are blocked and light emitting diodes (LEDs, drawn in the lateral view) on the AFM head are used as excitation source. In this mode, the EMCCD camera detects a dominantly red fraction of the LEDs' emission spectrum since all detected light has to pass the dualband dichroic filter as well as the emission filter in front of the camera.

AFM: The AFM head did only differ in one aspect from the one described ref. 10: For extraordinary transmission localization, three LEDs were mounted to the AFM-head as white light illumination source. A stable table (Micro40 M6/25, HALCYOICS) required for reducing vibrational noise in the AFM-signal was implemented underneath the main parts of the setup in such a way that the optical paths of confocal and TIRF fluorescence would leave it as parallel beams (see Fig. S7). This decoupled parallel movement of the stable table from optical signals. The AFM was controlled via self-written IGOR software (Wavemetrics), and cantilever calibration was based on the equipartition theorem[11]. For SMC&P processes, the sample was moved relative to the AFM by a xy-piezo stage (Physik Instrumente). An additional software routine allowed the external triggering of force curves i.e. cut and paste events via an analog signal.

Software: A custom-made software (LabView) was used to control TIRF laser, LED illumination, the sample holding xy-piezo and the EMCCD camera. The software also had the Gaussian fitting routines implemented and triggered the cut and paste routines by signaling to the AFM software. The main steps of the aperture loading procedure were executed by automated routines of the software. This was necessary to minimize the time lag between localization of the active anchor and the subsequent loading of an aperture, thus minimizing inaccuracies caused by thermal drift of involved components. To allow accurate conversion of the optically measured relative movements into piezo positions, the x- and y- conversion factors and a rotational constant were measured in a calibration procedure. For this, an aperture was localized optically, moved with the piezos by a known distance and then localized again.

SMC&P procedure

Whereas the lifetime measurements of pasted dyes were conducted on the setup described above, the loading process presented in Fig. 3 was made on another setup. It is described in ref. 8 and equipped with a green TIRF laser (532 nm wavelength). This is why a Cy3b label was used instead of the ATTO647N on the transfer strand.

Localization of the active anchor: Broad alignment of cantilever, sample and optics was done by eye under white light transmission and approximate positions of depot, reference window and target were saved. Loading of an aperture was then started by loading a transfer molecule from the depot onto the cantilever and pasting it into the reference window nearby the apertures. This process was optically controlled in TIRF illumination. Upon pasting and retraction of the cantilever, the dye was localized in an EMCCD image by a 2D-Gaussian fitting algorithm and its coordinates within the camera's coordinate system were saved. As the cantilever is kept at a fixed position with respect to the optical axis and the sample is moved instead, this position of the cantilever within the camera image is fixed.

Loading of the aperture: The aperture to be loaded was then positioned roughly underneath the cantilever by eye and localized with a Gaussian fit in LED illumination. The relative movement determined by the conversion factors and the localizations of the two fits was typically at the order of one micrometer, which reduced possible errors from imprecision of the conversion factors. After equipping the cantilever with a new transfer molecule from the depot, it was aligned with the aperture, and a paste in the aperture center was made. All cut- and paste processes were controlled live by TIRF fluorescence and force-distance curves.

Comparability: For lifetime measurements of pasted dyes, the same experimental buffer as in the stochastic measurements was used. Confocal scans were made right after loading of each aperture. To assure reproducible focusing of the confocal beam onto the surface plane and thus comparability of the fluorescence intensities, fine-adjustment of objective-sample distance was made in TIRF mode. To allow comparison of data from the two different confocal instruments (hybrid and regular), confocal scans of reference fluorophores pasted into a glass window were used for normalization.

Calculation of the loading process's lateral uncertainty

There are four main sources for lateral uncertainty in our aperture loading procedure: The positioning uncertainty of the two pastes (reference paste and final loading of the aperture) and the errors of the two superresolution localizations.

To measure the optical localization precision of our instrument, we carried out 100 subsequent localizations of a single dye under the same experimental conditions as in the SMC&P experiments (Fig. S8). The localizations were made on single frames of 0.1 s acquired over 10 s. Each frame had collected 990 ± 110 fluorescence photons from the dye, which corresponds well with the range of photon counts used for localizations of the reference pastes in the SMC&P experiments. The resulting standard error of the 100 localized positions was 9.7 nm. According to ref. 12, this localization precision can be approximated by $\frac{s}{\sqrt{N}}$, where *s* is the standard deviation of the point spread function and *N* is the number of detected

photons. An additional prefactor of $\sqrt{2}$ is necessary to take account for EMCCD excess camera noise[13]. With *s* = 280 ± 3 nm for the used setup, the theoretical localization precision for 990 photons thus is: 6.3 nm. This discrepancy between theory and experiment can be explained by polarization effects[14].

Other than fluorescence from dyes, extraordinary transmission of nanoapertures is not limited by photobleaching. Therefore, we collected at least a fourfold amount of photons from them. In the case of the less transmissive zero-mode waveguides, this was achieved by maximizing the LED emission power and by raising the integration time. The error of localizing a nanoaperture can therefore be approximated with 4.9 nm.

Regarding the general accuracy of a SMC&P event, we have previously demonstrated that the precision by which single molecules are placed relative to one another is ± 11 nm[15].

Therefore, the overall precision of our method - approximated by twice the uncertainty of a paste plus the localization errors of one dye and one aperture - sums up to 19 nm. It is dominated by the general positioning uncertainty of single SMC&P pastes, which could be reduced by shorter linker lengths or by denser surface functionalization[15]. This error analysis takes into account that the time interval between reference paste and loading of an aperture was less than 20 s, allowing to neglect the drifts of cantilever and sample.

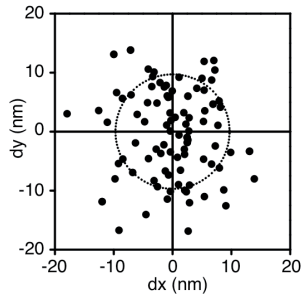

Fig. S8| Superresolution accuracy of the setup. 100 subsequent localizations of the same fluorophore result in a standard deviation of 9.7 nm (dotted circle). Localizations were made by Gaussian fits on approx. 1000 photons each.

References

1 Foquet, M. *et al.* Improved fabrication of zero-mode waveguides for single-molecule detection. *J. Appl. Phys.* **103**, 034301, doi:10.1063/1.2831366 (2008).

2 Moy, V., Florin, E. & Gaub, H. E. Intermolecular forces and energies between ligands and receptors. *Science* **266**, 257-259, doi:10.1126/science.7939660 (1994).

3 Strackharn, M., Stahl, S. W., Puchner, E. M. & Gaub, H. E. Functional assembly of aptamer binding sites by single-molecule cut-and-paste. *Nano Lett.* **12**, 2425-2428, doi:10.1021/nl300422y (2012).

4 Severin, P. M. D. & Gaub, H. E. DNA-protein binding force chip. *Small* **8**, 3269-3273, doi:10.1002/smll.201201088 (2012).

5 Strackharn, M., Stahl, S. W., Severin, P. M. D., Nicolaus, T. & Gaub, H. E. Peptide-antibody complex as handle for single-molecule cut & paste. *ChemPhysChem.* **13**, 914-917, doi:10.1002/cphc.201100765 (2011).

6 Stein, I. H. *et al.* Linking single-molecule blinking to chromophore structure and redox potentials. *ChemPhysChem.* **13**, 931-937, doi:10.1002/cphc.201100820 (2011).

7 Acuna, G. P. *et al.* Distance dependence of single-fluorophore quenching by gold nanoparticles studied on DNA origami. *ACS Nano* **6**, 3189-3195, doi:10.1021/nn2050483 (2012).

8 Heucke, S. F. *et al.* Nanoapertures for AFM-based single molecule force spectroscopy. *Int. J. Nanotechnol. (in the press)*.

9 Vogelsang, J. *et al.* A reducing and oxidizing system minimizes photobleaching and blinking of fluorescent dyes. *Angew. Chem. Int. Ed.* **47**, 5465-5469 (2008).

10 Gumpp, H., Stahl, S. W., Strackharn, M., Puchner, E. M. & Gaub, H. E. Ultrastable combined atomic force and total internal fluorescence microscope. *Rev. Sci. Instrum.* **80**, 063704 (063705), doi:10.1063/1.3148224 (2009).

11 Butt, H. J. & Jaschke, M. Calculation of thermal noise in atomic force microscopy. *Nanotechnology* **6**, 1-7, doi:10.1088/0957-4484/6/1/001 (1995).

12 Thompson, R. E., Larson, D. R. & Webb, W. W. Precise nanometer localization analysis for individual fluorescent probes. *Biophys. J.* **82**, 2775-2783 (2002).

13 Bossi, M. *et al.* Multicolor far-field fluorescence nanoscopy through isolated detection of distinct molecular species. *Nano Lett.* **8**, 2463-2468, doi:10.1021/nl801471d (2008).

14 Enderlein, J., Toprak, E. & Selvin, P. R. Polarization effect on position accuracy of fluorophore localization. *Opt. Express* **14**, 8111-8120 (2006).

15 Kufer, S. K. *et al.* Optically monitoring the mechanical assembly of single molecules. *Nat. Nanotechnol.* **4**, 45-49, doi:10.1038/nnano.2008.333 (2008).

6 Conclusion and Outlook

THz near-field microscopy of metamaterials

In the studies of THz metamaterials, the Mie interpretation of a secondary resonance in dielectric metamaterials could be refuted and it was shown that the resonance belongs to collective in-plane oscillations, instead. The exact nature of these oscillations remained open.

However, regarding the use of the investigated metamaterial for a biological assay the interesting hot-spots could be localized and spectrally characterized: In the presented case, the maximum capacitances of both modes were localized at the split gap. So, a dielectric change from proteins immobilized in the split gap will have an unlike higher effect on signal strength than proteins bound elsewhere on the structure. Consequently, a restriction of protein binding sites to the split gap can drastically lower the required sample amount while producing similar detection signals.

Thus, publication P1 succeeded to show the importance of experimental techniques compared to theoretical simulations which as a sole technique can fail to correctly predict physical mechanisms. In particular, THz near-field microscopy proved to be a viable analysis tool for biophotonic devices especially since most conclusions made for microscale structures will hold over a broad range of downscaled analogs.

Force and Fluorescence microscopy

The main studies of this thesis focused on the manipulation and placement of single-molecules in ZMWs.

The employment of these nanoapertures for force spectroscopy was a logic step, and the premiering results presented in publication P1 are the ultimate proof for the possibilities of this powerful combination. Limiting factors, especially the clogging of the cantilever tip from localizing AFM topography scans, hampered the acquisition of a sufficient amount of spectroscopy data which would have been necessary to make qualitative or quantitative conclusions about the kinetics of the underlying biomolecular system.

A general solution of this problem was given in chapter 5 where it was shown how live superresolution routines are to be employed to securely and centrally navigate the cantilever into a ZMW. Whereas the localization of ZMWs by extraordinary transmission generally can be employed in force spectroscopy, the adaptations necessary to localize the cantilever via a pasted reference dye are too elaborate for simple force spectroscopy experiments.

Several experimentally simpler alternatives are promising for tip localization:

i) One possibility is the localization of the tip's signal in transmission microscopy. Most cantilevers used in force spectroscopy are made from silicon which has an absorption length of ~1.8 µm in the visible (crystalline Si, at 600 nm wavelength) [87]. So, parallel light incident on a usually ~200 nm thin cantilever is transmitted with some losses. But the fraction incident on its high-aspect ratio tip experiences strong absorption because of the tip's length of several micrometers[‡]. The resulting "shadow", already been used for rough by eye alignment in publication P2, is a superposition of parallel and diffracted light so the resulting tip profile is far from a Gaussian-like point-spread function. However, as the signal generation is not bleaching-limited, here, employment of a suitable light-source and a more sophisticated fitting algorithm could enable tip localization with an accuracy of a few nanometers.

ii) Luminescence from doped silicon in cantilever tips is known to generate significant signals in fluorescence microscopy [100, 101]. The resulting signal profile is not that of a point-spread function but, in case of TIRF illumination, it will result from the lowest ~ 150 nm of the tip, and the widened source profile could again be compensated by adjusted fitting algorithms as in i).

iii) Finally, the most straight-forward way to localize a cantilever tip is via fluorescent labeling of the cantilever. The downside of this approach is of course an interference with the cantilever functionalization protocol that is likely to result in reduced interaction probabilities with respect to successful force-pulling events.

With one of the above or any alternative approach the implementation of a fast tip localization to the presented force and fluorescence spectroscopy method is possible and should allow the automated data acquisition at rates similar to those in standard fluorescence spectroscopy. With these adjustments at the latest, it then will have the potential of becoming a standard tool in the field and boost mechanoenzymatic research.

SMC&P in ZMWs

The probably the most important achievement of this thesis is the development of a methodology to anchor single-molecules in ZMWs. As the spectroscopic studies showed, the electrodynamic environment in ZMWs is highly heterogeneous. With the help of SMC&P-placed probes it was concluded that the apertures' center is their actual hot-spot. Here, a follow-up study could actually map the fluorescence properties by pasting probes at different off-center locations. This will be a good basis for theoretical framework comparing an emitting dipole in a short metallic cylinder to the classic dipole and mirror problem studied by Drexhage and others [45, 46, 49].

As SMC&P is lacking high throughput potential it is unlikely to become a standard method for loading commercially used, massively parallel assays like samples with ten thousands of ZMWs. However, as shown in publication P3, SMC&P is the method of choice to non-invasively probe the fluorescence properties of nanophotonic devices and to

[‡] this approximation neglects the cantilever's reflective coating. Also, some cantilevers differ in their actual lever material from that of their tip

locate their hot-spots. Based upon these findings, self-assembling spacers as e.g. DNA-origami can be used to restrict binding to desired sites in a convenient and cheap way.

In basic enzymological research, where less throughput is necessary, there are many scenarios where ZMWs-loading is advantageous. So for example when different enzymatic mutants are to be observed in neighboring ZMWs for a highly parallel comparison. Here, a precise placement of the different enzymes within the waveguides allows not only certainty about the underlying mutant but also to exclude a position-dependant sterical hindrance as cause for differences in single-enzyme spectroscopy results.

Great potential benefits also lie in the employment of SMC&P for combined force and fluorescence spectroscopy. Here, central anchoring and subsequent force-probing of single enzymes can be done in one step. The advantages are:

- comparable and high fluorescence intensities at the ZMWs' center
- a potentially 100% yield of unfolding-events per probing and thus a reduced risk of damaging the tip on the metallic sidewalls
- no potential cross-talk from other, pre-incubated enzymes in the ZMWs

This "pick-and-probe" technique will be best realized by covalently bonding enzymes to the ZMW's bottom through e.g. ybbR-tag fusion [102].

"SMC&P 2.0"

The refinement of SMC&P with superresolution positioning should additionally be seen in a greater picture than that of probing or loading photonic nanostructures: After Kufer et al. invented the technique and established the positioning of single-molecules with nanometer-precision relative to one another, it has been taken to a new level as biochemical modifications enabled the transport of whole proteins and superresolution allows precise placement relative to an absolute position on a sample structure.

In alternative to ZMWs, randomly distributed nanoparticles [103] or silicon discs [104] can also be localized with superresolution capabilities. Navigation to coordinates that are not a-priori defined within the SMC&P piezo-positioning system, then allows drift independent bottom-up assembly over long time spans. This ability combined with direct protein transport [105] are requisites for the single-molecule assembly of complex enzyme networks as e.g. designer cellulosomes [106].

To remark concludingly: The use of extraordinary transmission for the loading of ZMWs which may be used to build large enzymatic networks, is just a further example of the symbiosis of methodological development and scientific findings.

7 Bibliography

[1] Puchner, E. M., A. Alexandrovich, A. L. Kho, U. Hensen, L. V. Schäfer, B. Brandmeier, F. Gräter, H. Grubmüller, H. E. Gaub and M. Gautel: *Mechanoenzymatics of titin kinase*. Proceedings of the National Academy of Sciences, 105(36):13385, **2008**.

[2] Rothemund, P. W. K.: *Folding DNA to create nanoscale shapes and patterns*. Nature, 440(7082):297-302, **2006**.

[3] Yildiz, A., J. N. Forkey, S. A. McKinney, T. Ha, Y. E. Goldman and P. R. Selvin: *Myosin V walks hand-over-hand: Single fluorophore imaging with 1.5-nm localization*. Science, 300(5628):2061-2065, **2003**.

[4] Geisler, M., S. Xiao, E. M. Puchner, F. Gräter and T. Hugel: *Controlling the structure of proteins at surfaces*. Journal of the American Chemical Society, 132(48):17277-17281, **2010**.

[5] Vollrath, F. and D. P. Knight: *Liquid crystalline spinning of spider silk*. Nature, 410(6828):541-548, **2001**.

[6] Andersen, E. S., M. Dong, M. M. Nielsen, K. Jahn, R. Subramani, W. Mamdouh, M. M. Golas, B. Sander, H. Stark, C. L. P. Oliveira, J. S. Pedersen, V. Birkedal, F. Besenbacher, K. V. Gothelf and J. Kjems: *Self-assembly of a nanoscale DNA box with a controllable lid*. Nature, 459(7243):73-76, **2009**.

[7] Willets, K. A. and R. P. Van Duyne: *Localized surface plasmon resonance spectroscopy and sensing*. Annual Review of Physical Chemistry, 58:267-297, **2007**.

[8] Anker, J. N., W. P. Hall, O. Lyandres, N. C. Shah, J. Zhao and R. P. Van Duyne: *Biosensing with plasmonic nanosensors*. Nature materials, 7(6):442-453, **2008**.

[9] Ståhl, P. L. and J. Lundeberg: *Toward the single-hour high-quality genome*. Annual Review of Biochemistry, 81(1):359-378, **2012**.

[10] Howorka, S., S. Cheley and H. Bayley: *Sequence-specific detection of individual DNA strands using engineered nanopores*. Nature Biotechnology, 19(7):636-639, **2001**.

[11] Eid, J., A. Fehr, J. Gray, K. Luong, J. Lyle, G. Otto, P. Peluso, D. Rank, P. Baybayan, B. Bettman, A. Bibillo, K. Bjornson, B. Chaudhuri, F. Christians, R. Cicero, S. Clark, R. Dalal, A. Dewinter, J. Dixon, M. Foquet, A. Gaertner, P. Hardenbol, C. Heiner, K. Hester, D. Holden, G. Kearns, X. Kong, R. Kuse, Y. Lacroix, S. Lin, P. Lundquist, C. Ma, P. Marks, M. Maxham, D. Murphy, I. Park, T. Pham, M. Phillips, J. Roy, R. Sebra, G. Shen, J. Sorenson, A. Tomaney, K. Travers, M. Trulson, J. Vieceli, J. Wegener, D. Wu, A. Yang, D. Zaccarin, P. Zhao, F. Zhong, J. Korlach and S. Turner: *Real-time DNA sequencing from single polymerase molecules.* Science, 323(5910):133-138, **2009**.

[12] Rothberg, J. M., W. Hinz, T. M. Rearick, J. Schultz, W. Mileski, M. Davey, J. H. Leamon, K. Johnson, M. J. Milgrew, M. Edwards, J. Hoon, J. F. Simons, D. Marran, J. W. Myers, J. F. Davidson, A. Branting, J. R. Nobile, B. P. Puc, D. Light, T. A. Clark, M. Huber, J. T. Branciforte, I. B. Stoner, S. E. Cawley, M. Lyons, Y. Fu, N. Homer, M. Sedova, X. Miao, B. Reed, J. Sabina, E. Feierstein, M. Schorn, M. Alanjary, E. Dimalanta, D. Dressman, R. Kasinskas, T. Sokolsky, J. A. Fidanza, E. Namsaraev, K. J. McKernan, A. Williams, G. T. Roth and J. Bustillo: *An integrated semiconductor device enabling non-optical genome sequencing*. Nature, 475(7356):348-352, **2011**.

[13] Chin, C.-S., J. Sorenson, J. B. Harris, W. P. Robins, R. C. Charles, R. R. Jean-Charles, J. Bullard, D. R. Webster, A. Kasarskis, P. Peluso, E. E. Paxinos, Y. Yamaichi, S. B. Calderwood, J. J. Mekalanos, E. E. Schadt and M. K. Waldor: *The origin of the haitian cholera outbreak strain*. New England Journal of Medicine, 364(1):33-42, **2011**.

[14] Rasko, D. A., D. R. Webster, J. W. Sahl, A. Bashir, N. Boisen, F. Scheutz, E. E. Paxinos, R. Sebra, C.-S. Chin and D. Iliopoulos: *Origins of the e. coli strain causing an outbreak of hemolytic–uremic syndrome in germany*. New England Journal of Medicine, 365(8):709-717, **2011**.

[15] Kuehn, B. M.: *Database of food-borne pathogen genomes created*. Journal of the American Medical Association, 308(6):557-557, **2012**.

[16] Church, G. M.: *The personal genome project*. Molecular Systems Biology, 1(1), **2005**.

[17] Venter, J. C.: *Multiple personal genomes await*. Nature, 464(7289):676-677, **2010**.

[18] Ebbesen, T. W., H. J. Lezec, H. F. Ghaemi, T. Thio and P. A. Wolff: *Extraordinary optical transmission through sub-wavelength hole arrays*. Nature, 391(6668):667-669, **1998**.

[19] Moy, V. T., E. Florin and H. E. Gaub: *Intermolecular forces and energies between ligands and receptors*. Science, 266(5183):257-259, **1994**.

[20] Enderle, T., T. Ha, D. F. Ogletree, D. S. Chemla, C. Magowan and S. Weiss: *Membrane specific mapping and colocalization of malarial and host skeletal proteins in the plasmodium falciparum infected erythrocyte by dual-color near-field scanning optical microscopy*. Proceedings of the National Academy of Sciences, 94(2):520-525, **1997**.

[21] Acuna, G. P., F. M. Moller, P. Holzmeister, S. Beater, B. Lalkens and P. Tinnefeld: *Fluorescence enhancement at docking sites of DNA-directed self-assembled nanoantennas*. Science, 338(6106):506-510, **2012**.

[22] Haes, A. J., L. Chang, W. L. Klein and R. P. Van Duyne: *Detection of a biomarker for Alzheimer's disease from synthetic and clinical samples using a nanoscale optical biosensor*. Journal of the American Chemical Society, 127(7):2264-2271, **2005**.

[23] Kufer, S. K., E. M. Puchner, H. Gumpp, T. Liedl and H. E. Gaub: *Single-molecule cut-and-paste surface assembly.* Science, 319(5863):594-596, **2008**.

[24] Crut, A., D. A. Koster, Z. Huang, S. Hage and N. H. Dekker: *Controlling the surface properties of nanostructures for studies of polymerases*. Nanotechnology, 19(46):465301, **2008**.

[25] Tinnefeld, P. and M. Sauer: *Branching out of single-molecule fluorescence spectroscopy: Challenges for chemistry and influence on biology*. Angewandte Chemie International Edition, 44(18):2642-2671, **2005**.

[26] Lakowicz, J. R. (1999). *Principles of fluorescence spectroscopy* (2nd ed.). Kluwer Academic.

[27] Vogelsang, J., R. Kasper, C. Steinhauer, B. Person, M. Heilemann, M. Sauer and P. Tinnefeld: *A reducing and oxidizing system minimizes photobleaching and blinking of fluorescent dyes*. Angewandte Chemie International Edition, 47(29):5465-5469, **2008**.

[28] Lu, H. P., L. Xun and X. S. Xie: *Single-molecule enzymatic dynamics*. Science, 282(5395):1877-1882, **1998**.

[29] Zhuang, X., L. E. Bartley, H. P. Babcock, R. Russell and T. Ha: *A single-molecule study of RNA catalysis and folding*. Science, **2000**.

[30] Schuler, B., E. A. Lipman and W. A. Eaton: *Probing the free-energy surface for protein folding with single-molecule fluorescence spectroscopy*. Nature, 419(6908):743-747, **2002**.

[31] Levene, M. J., J. Korlach, S. W. Turner, M. Foquet, H. G. Craighead and W. W. Webb: *Zero-mode waveguides for single-molecule analysis at high concentrations*. Science, 299(5607):682-686, **2003**.

[32] Laurence, T. A. and S. Weiss: *How to detect weak pairs*. Science, 299(5607):667-668, **2003**.

[33] Zhu, P. and H. G. Craighead: *Zero-mode waveguides for single-molecule analysis*. Annual Review of Biophysics, 41(1):269-293, **2012**.

[34] Schwille, P.: *Fluorescence correlation spectroscopy and its potential for intracellular applications*. Cell biochemistry and biophysics, **2001**.

[35] Wenger, J., E. Popov, H. Rigneault, J. Dintinger and T. Ebbesen: *Single molecule fluorescence in rectangular nano-apertures*. Optics Express, **2005**.

[36] Samiee, K. T., J. M. Moran-Mirabal, Y. K. Cheung and H. G. Craighead: *Zero mode waveguides for single-molecule spectroscopy on lipid membranes*. Biophysical Journal, 90(9):3288-3299, **2006**.

[37] Lundquist, P. M., C. F. Zhong, P. Zhao, A. B. Tomaney, P. S. Peluso, J. Dixon, B. Bettman, Y. Lacroix, D. P. Kwo, E. McCullough, M. Maxham, K. Hester, P. McNitt, D. M. Grey, C. Henriquez, M. Foquet, S. W. Turner and D. Zaccarin: *Parallel confocal detection of single molecules in real time*. Optics Letters, 33(9):1026-1028, **2008**.

[38] Hassler, K., M. Leutenegger, P. Rigler, R. Rao, R. Rigler, M. Gösch and T. Lasser: *Total internal reflection fluorescence correlation spectroscopy (TIR-FCS) with low background and high count-rate per molecule*. Optics Express, 13(19):7415-7423, **2005**.

[39] Xie, X. S. and R. C. Dunn: *Probing single molecule dynamics*. Science, 265(5170):361-364, **1994**.

[40] Hell, S. W. and J. Wichmann: *Breaking the diffraction resolution limit by stimulated emission: Stimulated-emission-depletion fluorescence microscopy*. Optics Letters, 19(11):780-782, **1994**.

[41] Genet, C. and T. W. Ebbesen: *Light in tiny holes*. Nature, 445(7123):39-46, **2007**.

[42] Heucke, S. F., E. M. Puchner, S. W. Stahl, A. W. Holleitner, H. E. Gaub and P. Tinnefeld: *Nanoapertures for AFM-based single molecule force spectroscopy*. International Journal of Nanotechnology, 10(5/6/7):607-619, **2013,** http://www.inderscience.com/jhome.php?jcode=ijnt.

[43] Anger, P., P. Bharadwaj and L. Novotny: *Enhancement and quenching of single-molecule fluorescence*. Physical Review Letters, 96(11):113002, **2006**.

[44] Barnes, W. L.: *Fluorescence near interfaces: The role of photonic mode density*. Journal of Modern Optics, 45(4):661-699, **1998**.

[45] Drexhage, K. H.: *Influence of a dielectric interface on fluorescence decay time*. Journal of Luminescence, 1:693-701, **1970**.

[46] Enderlein, J.: *Single-molecule fluorescence near a metal layer*. Chemical Physics, 247(1):1-9, **1999**.

[47] Geddes, C. D. and J. R. Lakowicz: *Metal-enhanced fluorescence*. Journal of Fluorescence, 12(2):121-129, **2002**.

[48] Lakowicz, J. R.: *Radiative decay engineering 5: Metal-enhanced fluorescence and plasmon emission*. Analytical Biochemistry, 337(2):171-194, **2005**.

[49] Chance, R. R., A. H. Miller, A. Prock and R. Silbey: *Fluorescence and energy transfer near interfaces: The complete and quantitative description of the Eu+3/ mirror systems*. The Journal of Chemical Physics, 63(4):1589-1595, **1975**.

[50] Acuna, G. P., M. Bucher, I. H. Stein, C. Steinhauer, A. Kuzyk, P. Holzmeister, R. Schreiber, A. Moroz, F. D. Stefani, T. Liedl, F. C. Simmel and P. Tinnefeld: *Distance dependence of single-fluorophore quenching by gold nanoparticles studied on DNA origami*. ACS Nano, 6(4):3189-3195, **2012**.

[51] Seelig, J., K. Leslie, A. Renn, S. Kühn, V. Jacobsen, M. Van de Corput, C. Wyman and V. Sandoghdar: *Nanoparticle-induced fluorescence lifetime modification as nanoscopic ruler: Demonstration at the single molecule level*. Nano Letters, 7(3):685-689, **2007**.

[52] Rigneault, H., J. Capoulade, J. Dintinger, J. Wenger, N. Bonod, E. Popov, T. Ebbesen and P.-F. Lenne: *Enhancement of single-molecule fluorescence detection in subwavelength apertures*. Physical Review Letters, 95(11):117401, **2005**.

[53] Wenger, J., B. Cluzel, J. Dintinger, N. Bonod, A. L. Fehrembach, E. Popov, P. F. Lenne, T. W. Ebbesen and H. Rigneault: *Radiative and nonradiative photokinetics alteration inside a single metallic nanometric aperture*. Journal of Physical Chemistry C, 111(30):11469-11474, **2007**.

[54] Liu, Y. and S. Blair: *Fluorescence enhancement from an array of subwavelength metal apertures*. Optics Letters, 28(7):507, **2003**.

[55] Foquet, M., K. T. Samiee, X. Kong, B. P. Chauduri, P. M. Lundquist, S. W. Turner, J. Freudenthal and D. B. Roitman: *Improved fabrication of zero-mode waveguides for single-molecule detection*. Journal of Applied Physics, 103(3):034301, **2008**.

[56] Korlach, J., P. J. Marks, R. L. Cicero, J. J. Gray, D. L. Murphy, D. B. Roitman, T. T. Pham, G. A. Otto, M. Foquet and S. W. Turner: *Selective aluminum passivation for targeted immobilization of single DNA polymerase molecules in zero-mode waveguide nanostructures*. Proceedings of the National Academy of Sciences, 105(4):1176-1181, **2008**.

[57] Miyake, T., T. Tanii, H. Sonobe, R. Akahori, N. Shimamoto, T. Ueno, T. Funatsu and I. Ohdomari: *Real-time imaging of single-molecule fluorescence with a zero-mode waveguide for the analysis of protein− protein interaction*. Analytical Chemistry, 80(15):6018-6022, **2008**.

[58] Patel, S. S., I. Wong and K. A. Johnson: *Pre-steady-state kinetic analysis of processive DNA replication including complete characterization of an exonuclease-deficient mutant*. Biochemistry, 30(2):511-525, **1991**.

[59] Flusberg, B. A., D. R. Webster, J. H. Lee, K. J. Travers, E. C. Olivares, T. A. Clark, J. Korlach and S. W. Turner: *Direct detection of DNA methylation during single-molecule, real-time sequencing*. Nature Methods, 7(6):461-465, **2010**.

[60] Samiee, K., M. Foquet, L. Guo, E. Cox and H. Craighead: *Lambda-repressor oligomerization kinetics at high concentrations using fluorescence correlation spectroscopy in zero-mode waveguides*. Biophysical Journal, 88(3):2145-2153, **2005**.

[61] Moran-Mirabal, J. M., A. J. Torres, K. T. Samiee, B. A. Baird and H. G. Craighead: *Cell investigation of nanostructures: Zero-mode waveguides for plasma membrane studies with single molecule resolution*. Nanotechnology, 18(19):195101, **2007**.

[62] Uemura, S., C. E. Aitken, J. Korlach, B. A. Flusberg, S. W. Turner and J. D. Puglisi: *Real-time tRNA transit on single translating ribosomes at codon resolution*. Nature, 464(7291):1012-1017, **2010**.

[63] Veselago, V. G.: *The electrodynamics of substances with simultaneously negative values of ε and μ*. Soviet Physics Uspekhi, 10:509-514, **1968**.

[64] Pendry, J. B., A. J. Holden, D. J. Robbins and W. J. Stewart: *Magnetism from conductors and enhanced nonlinear phenomena*. IEEE Transactions on Microwave Theory and Techniques, 47(11):2075-2084, **1999**.

[65] Smith, D., W. Padilla, D. Vier, S. Nemat-Nasser and S. Schultz: *Composite medium with simultaneously negative permeability and permittivity*. Physical Review Letters, 84(18):4184-4187, **2000**.

[66] Shelby, R. A., D. R. Smith and S. Schultz: *Experimental verification of a negative index of refraction*. Science, 292(5514):77-79, **2001**.

[67] Pendry, J. B. and D. R. Smith: *Reversing light: Negative refraction*. Physics Today, 8, **2003**.

[68] Ramakrishna, S. A.: *Physics of negative refractive index materials*. Reports on Progress in Physics, 68(2):449, **2005**.

[69] Klingshirn, C. F. (2007). *Semiconductor optics* (3rd ed.). Springer.

[70] Pendry, J., A. Holden, W. Stewart and I. Youngs: *Extremely low frequency plasmons in metallic mesostructures*. Physical Review Letters, 76(25):4773-4776, **1996**.

[71] Enkrich, C., M. Wegener, S. Linden, S. Burger, L. Zschiedrich, F. Schmidt, J. F. Zhou, T. Koschny and C. M. Soukoulis: *Magnetic metamaterials at telecommunication and visible frequencies*. Physical Review Letters, 95(20):203901, **2005**.

[72] Padilla, W., M. Aronsson, C. Highstrete, M. Lee, A. Taylor and R. Averitt: *Electrically resonant terahertz metamaterials: Theoretical and experimental investigations*. Physical Review B, 75(4):041102, **2007**.

[73] Kuzyk, A., R. Schreiber, Z. Fan, G. Pardatscher, E.-M. Roller, A. Högele, F. C. Simmel, A. O. Govorov and T. Liedl: *DNA-based self-assembly of chiral plasmonic nanostructures with tailored optical response*. Nature, 483(7389):311-314, **2012**.

[74] Gansel, J. K., M. Thiel, M. S. Rill, M. Decker, K. Bade, V. Saile, G. von Freymann, S. Linden and M. Wegener: *Gold helix photonic metamaterial as broadband circular polarizer*. Science, 325(5947):1513-1515, **2009**.

[75] Pendry, J. B.: *Negative refraction makes a perfect lens*. Physical Review Letters, 85(18):3966-3969, **2000**.

[76] Fang, N.: *Sub-diffraction-limited optical imaging with a silver superlens*. Science, 308(5721):534-537, **2005**.

[77] Liu, Z., H. Lee, Y. Xiong, C. Sun and X. Zhang: *Far-field optical hyperlens magnifying sub-diffraction-limited objects*. Science, 315(5819):1686-1686, **2007**.

[78] Leonhardt, U.: *Optical conformal mapping*. Science, 312(5781):1777-1780, **2006**.

[79] Schurig, D., J. J. Mock, B. J. Justice, S. A. Cummer, J. B. Pendry, A. F. Starr and D. R. Smith: *Metamaterial electromagnetic cloak at microwave frequencies*. Science, 314(5801):977-980, **2006**.

[80] Chen, H.-T., W. J. Padilla, J. M. O. Zide, A. C. Gossard, A. J. Taylor and R. D. Averitt: *Active terahertz metamaterial devices*. Nature, 444(7119):597-600, **2006**.

[81] Soukoulis, C. M. and M. Wegener: *Past achievements and future challenges in the development of three-dimensional photonic metamaterials*. Nature Photonics, **2011**.

[82] Lee, H.-J. and J.-G. Yook: *Biosensing using split-ring resonators at microwave regime*. Applied Physics Letters, 92(25):254103, **2008**.

[83] Chen, H. T., S. Kraatz, G. Cho and R. Kersting: *Identification of a resonant imaging process in apertureless near-field microscopy*. Physical Review Letters, 93(26):267401, **2004**.

[84] Buersgens, F., G. P. Acuna, C. H. Lang, S. I. Potrebic, S. Manus and R. Kersting: *Shear force control for a terahertz near field microscope*. Rev Sci Instrum, 78(11):113701-113706, **2007**.

[85] Klein, M. W., C. Enkrich, M. Wegener and S. Linden: *Second-harmonic generation from magnetic metamaterials*. Science, 313(5786):502-504, **2006**.

[86] Acuna, G. P., S. F. Heucke, F. Kuchler, H. T. Chen, A. J. Taylor and R. Kersting: *Surface plasmons in terahertz metamaterials.* Optics Express, 16(23):18745-18751, **2008**.

[87] Palik, E. D. (1991). *Handbook of optical constants of solids II*. Academic.

[88] Ritchie, R., E. Arakawa, J. Cowan and R. Hamm: *Surface-plasmon resonance effect in grating diffraction*. Physical Review Letters, 21(22):1530-1533, **1968**.

[89] Barnes, W. L., A. Dereux and T. W. Ebbesen: *Surface plasmon subwavelength optics*. Nature, 424(6950):824-830, **2003**.

[90] Tang, C. J., P. Zhan, Z. S. Cao, J. Pan, Z. Chen and Z. L. Wang: *Magnetic field enhancement at optical frequencies through diffraction coupling of magnetic plasmon resonances in metamaterials*. Physical Review B, 83(4):041402, **2011**.

[91] Ortuño, R., C. García-Meca, F. Rodríguez-Fortuño, J. Martí and A. Martínez: *Role of surface plasmon polaritons on optical transmission through double layer metallic hole arrays*. Physical Review B, 79(7):075425, **2009**.

[92] Liu, H., T. Li, S.-m. Wang and S.-n. Zhu: *Hybridization effect in coupled metamaterials*. Frontiers of Physics in China, 5(3):277, **2010**.

[93] Schloegl, S. *Polaritonen in terahertz–metamaterialien,* thesis, Ludwig-Maximilians-Universität München, Munich, 2009 (unpublished).

[94] Stigler, J., F. Ziegler, A. Gieseke, J. C. M. Gebhardt and M. Rief: *The complex folding network of single calmodulin molecules*. Science, 334(6055):512, **2011**.

[95] Lang, M. J., P. M. Fordyce, A. M. Engh, K. C. Neuman and S. M. Block: *Simultaneous, coincident optical trapping and single-molecule fluorescence*. Nature Methods, 1(2):133-139, **2004**.

[96] Hohng, S., R. Zhou, M. K. Nahas, J. Yu, K. Schulten, D. M. J. Lilley and T. Ha: *Fluorescence-force spectroscopy maps two-dimensional reaction landscape of the holliday junction*. Science, 318(5848):279-283, **2007**.

[97] Gumpp, H., E. M. Puchner, J. L. Zimmermann, U. Gerland, H. E. Gaub and K. Blank: *Triggering enzymatic activity with force*. Nano Letters, 9(9):3290-3295, **2009**.

[98] Vargel, C. (2004). *Corrosion of aluminium*. Elsevier.

[99] Gumpp, H., S. W. Stahl, M. Strackharn, E. M. Puchner and H. E. Gaub: *Ultrastable combined atomic force and total internal fluorescence microscope*. Rev Sci Instrum, 80(6):063704 (063705), **2009**.

[100] Kufer, S. K., M. Strackharn, S. W. Stahl, H. Gumpp, E. M. Puchner and H. E. Gaub: *Optically monitoring the mechanical assembly of single molecules*. Nature Nanotechnology, 4(1):45-49, **2008**.

[101] Gaiduk, A., R. K hnemuth, M. Antonik and C. A. M. Seidel: *Optical characteristics of atomic force microscopy tips for single-molecule fluorescence applications*. Chemphyschem, 6(5):976-983, **2005**.

[102] Yin, J., A. J. Lin, D. E. Golan and C. T. Walsh: *Site-specific protein labeling by sfp phosphopantetheinyl transferase*. Nature Protocols, 1(1):280-285, **2006**.

[103] Urban, A. S., M. Fedoruk, M. R. Horton, J. O. Rädler, F. D. Stefani and J. Feldmann: *Controlled nanometric phase transitions of phospholipid membranes by plasmonic heating of single gold nanoparticles*. Nano Letters, 9(8):2903-2908, **2009**.

[104] King, G. M., A. R. Carter, A. B. Churnside, L. S. Eberle and T. T. Perkins: *Ultrastable atomic force microscopy: Atomic-scale stability and registration in ambient conditions*. Nano Letters, 9(4):1451-1456, **2009**.

[105] Strackharn, M., D. A. Pippig, P. Meyer, S. W. Stahl and H. E. Gaub: *Nanoscale arrangement of proteins by single-molecule cut-and-paste*. Journal of the American Chemical Society, 134(37):15193-15196, **2012**.

[106] Bayer, E. A., E. Morag and R. Lamed: *The cellulosome—a treasure-trove for biotechnology*. Trends in Biotechnology, 12(9):379-386, **1994**.

Appendix

Investigating the Affinity of Focal Adhesion Kinase to PIP2

In this preliminary study, a general affinity of the potentially force-activated enzyme Focal Adhesion Kinase to Phosphatidylinositol (4,5)-bisphosphate in lipid membranes could be detected; however, initial results estimate the binding forces to be around 15 to 20 pN, which is too low for quantitative AFM-based force spectroscopy measurements.

Introduction

Signaling via transmembrane proteins is a major communication pathway in cells. It regulates cellular growth or cell migration and is further crucial in immunological detection and defense processes [A1]. Research of these signaling pathways (has) received marked attention in recent past[‡] and this also because errors in these networks are often the cause for severe diseases [A2]. The actual signal transduction usually involves numerous proteins, complex signaling cascades and feedback mechanisms. Triggering stimuli can be e.g. growth factors, pathogenic agents or force.

One prominent protein involved in transmembrane cell signaling is Focal Adhesion Kinase (FAK) [A3, A4]. It is found in the focal adhesions which are membrane areas where the cytosceleton is linked to the extracellular matrix. Here, FAK resembles a link between clustering integrins and upstream signaling proteins, while its main role is the direction and regulation of motillity.

FAK was linked to cell force sensing [A5], and recent molecular dynamics simulations [A6] hint towards a direct force-activation of FAK similar to that in titin kinase [A7]. The direct activation of FAK's catalytic domain is excpected to be a result of strain building up after FAK's FERM-domain binds to phosphatidylinositol (4,5)-bisphosphate (PIP2).

Simultaneous force and fluorescence spectroscopy could enable to investigate this suggested activation mechanism as well as the kinetics of the activated enzymatic pathways. This may lead to a better understanding of cell force-sensing and, in a further perspective, reveal access-points for drug treatment [A8].

---

‡ The 2012 Nobel Prize in chemistry was awarded to R. Lefkowitz and B. Koblinka for their work on g-protein coupled receptors and their function in transmembrane cell signalling

Here, results from preliminary studies are presented, aiming at the investigation of the general affinity of FAK to PIP2 and on the question whether this system is suitable for AFM-based force and fluorescence spectroscopy: In a twofold approach, we used the method of continuous bleaching to determine whether FERM has an actual affinity to PIP2 and we also applied AFM-based force spectroscopy in an approach to quantify that affinity.

Methods

FAK (GeneBank AAA58469.1; amino acids 31-686) and sole FERM-domain (aa 31-405) used in this study were provided by the group of Daniel Lietha at the National Cancer Research Center (Madrid, Spain). Both protein constructs had been N-terminally fused with an ybbR-tag that was then used for CoenzymeA/Sfp-mediated linkage [A9, A10].

Fluid supported lipid bilayers (SLB) were made by vesicle fusion [A11] in different mixtures of: 1,2-dioleoyl-sn-glycero-3-phosphocholine (DOPC; Avanti Polar Lipids, United States), Texas-Red® labeled 1,2-Dihexadecanoyl-sn-Glycero-3-Phosphoethanolamine (TR-DHPE; Life Technologies, United States), 1,2-dioleoyl-sn-glycero-3-phospho-(1'-myo-inositol-4',5'-bisphosphate) (PI(4,5)P2; Avanti Polar Lipids) and 1,2-dioleoyl-sn-glycero-3-phospho-(1'-myo-inositol-3',4',5'-triphosphate) (PI(3,4,5)P3; Avanti Polar Lipids). Throughout the study, the quality of the SLBs was systematically checked by fluorescence microscopy. Here, 0.1% TR-DHPE added in control samples showed a homogeneous wafting fluorescence proving the continuity and homogeneity of the bilayers. Only SLBs containing significantly more than 5% PI(4,5)P2 or PI(3,4,5)P3 were sometimes discontinuous. This diffraction limited control method cannot exclude nanoscopic defects in the SLBs.

Continuous bleaching [A12, A13] is a convenient method to measure the lateral diffusion coefficient in SLBs as it requires only a standard fluorescence microscope with a circular field stop that restricts the illuminated area. Here, an Axiovert 25 (Carl Zeiss ; Germany) was used. Briefly, a fluorescently labeled fluid membrane is homogeneously bleached over a circular area given by the aperture of the field stop. As the area's radius r well exceeds the average distance a label will diffuse before it is bleached, the center will eventually be bleached to a background value, while unbleached labels diffusing into the illuminated area will form a bright halo on the edge of the aperture. Whereas the forming of a halo is already proof of lateral diffusion, the diffusion coefficient D can be extracted by fitting the halo profile with the following equation:

$$I(x) = I_r \cdot e^{-\sqrt{b/D}\cdot(r-x)} + B \qquad (A1)$$

Here, $I(x)$ is the measured intensity at distance x from the center, I_r is the intensity at the edge of the rim, b is the bleaching rate and B is the background fluorescence intensity. The bleaching rate b is determined beforehand by fitting the fluorescence decay over time at the aperture's center with

$$I(t) = I_0 \cdot e^{-b\cdot t} + B \qquad (A2)$$

where I_0 is the center's aperture at the beginning of the bleaching process.

For force spectroscopy we used the setup described in publication P2 and cantilevers with a rather large contact surface (MLCT, Bruker, USA) and spring constants between 11 and 14 pN/nm. The cantilevers were first silanized with 3-

Aminopropyldimethylethoxysilane, then the NHS group of a polyethylene glycol spacer, Malhex-CONH-PEG-NHS (PEG; Rapp, Germany), was covalently linked to the amino group. CoenzymeA was reacted to the PEG-Maleimide by its Thiol group and, finally, the FAK or FERM-domain were attached at their ybbR-tag via Coenzyme A/Sfp [A9]. Force-distance profiles were collected with alternating pulling speeds of 50 and 100 nm/s, and after each pulling curve the sample was moved by 50 nm resulting in an overall quadratic screening of the SLB surface.

Results and Discussion

For the continuous bleaching experiments, fluorescently labeled FERM domain was incubated on SLBs consisting of i) DOPC, ii) DOPC and 5% PIP2, and iii) DOPC and 5% PIP3. After 70 minutes, unbound FERM was gently washed away from the samples by buffer exchange.

In all three cases, several strongly fluorescent dots and a weakly fluorescent film were observed. Since the dots remained stationary and were of the same size as the SLB precursor vesicles, they cannot be part of the fluid membrane but are likely FERM-domains or loose labels bound to non-fused vesicles stuck underneath the SLBs. The weak fluorescent film did not recover from the aperture surrounding unbleached regions and, therefore, could be detached labels, small enough to penetrate through the SLB and to adhere on the supporting cover slip.

A third, much stronger fluorescence population was observed exclusively in case ii) (see fig. A1). It appeared as wafting mist of fluorescence homogeneously distributed over the SLB. After bleaching for 5 minutes, a fluorescent halo had formed on the edge of the illumination restricting aperture. As mentioned above, this is already qualitative proof that the fluorescence stems from two-dimensional diffusion on the sample surface. The lateral diffusion coefficient of the fluorescent labels was quantified by fitting the fluorescence profile according to equation A1. The resulting diffusion coefficient was 1.6 $\mu m^2 s^{-1}$ (see fig. A1). The overall error of this coefficient is not given from the error of the fitting algorithm, but is dominated by the approximations of continuous bleaching theory with regard to the geometry of the bleaching scenario [A13, A14]. Since the diffusion constant as such is not a subject of this study, we refrained from a thorough error analysis thereof.

Instead, the lateral diffusion coefficient of the membrane itself was measured for comparison: The resulting diffusion coefficient from an SLBs consisting of 95% DOPC, 5% PIP2 and 0,1% labeled DHPE was measured to be 4.2 $\mu m^2 s^{-1}$. Because of the relatively low bleaching rate of the DHPE label Texas Red® the center of the illuminated area could not be bleached to background level with the given aperture of the setup. Thus, the diffusion coefficient of the SLB is to be regarded as upper limit.

So, considering that the FERM-domain's relatively large size results in a somewhat slower diffusion, the measured diffusion coefficient roughly agrees with the DOPC control as well as with a literature value from ref. [A15]. Together with the fact that detaching FERM would mostly diffuse into the buffer without returning to the surface, our measurements thus proof a general affinity of FERM to PIP2. Furthermore, the off-rates of this binding must be in the range of the bleaching experiments lasting over several minutes. The absence of an observable diffusing fluorescence population in the case of PIP3 containing SLBs and those from pure DOPC is gives proof that this affinity is exclusive to PIP2 - at least at these off-rates.

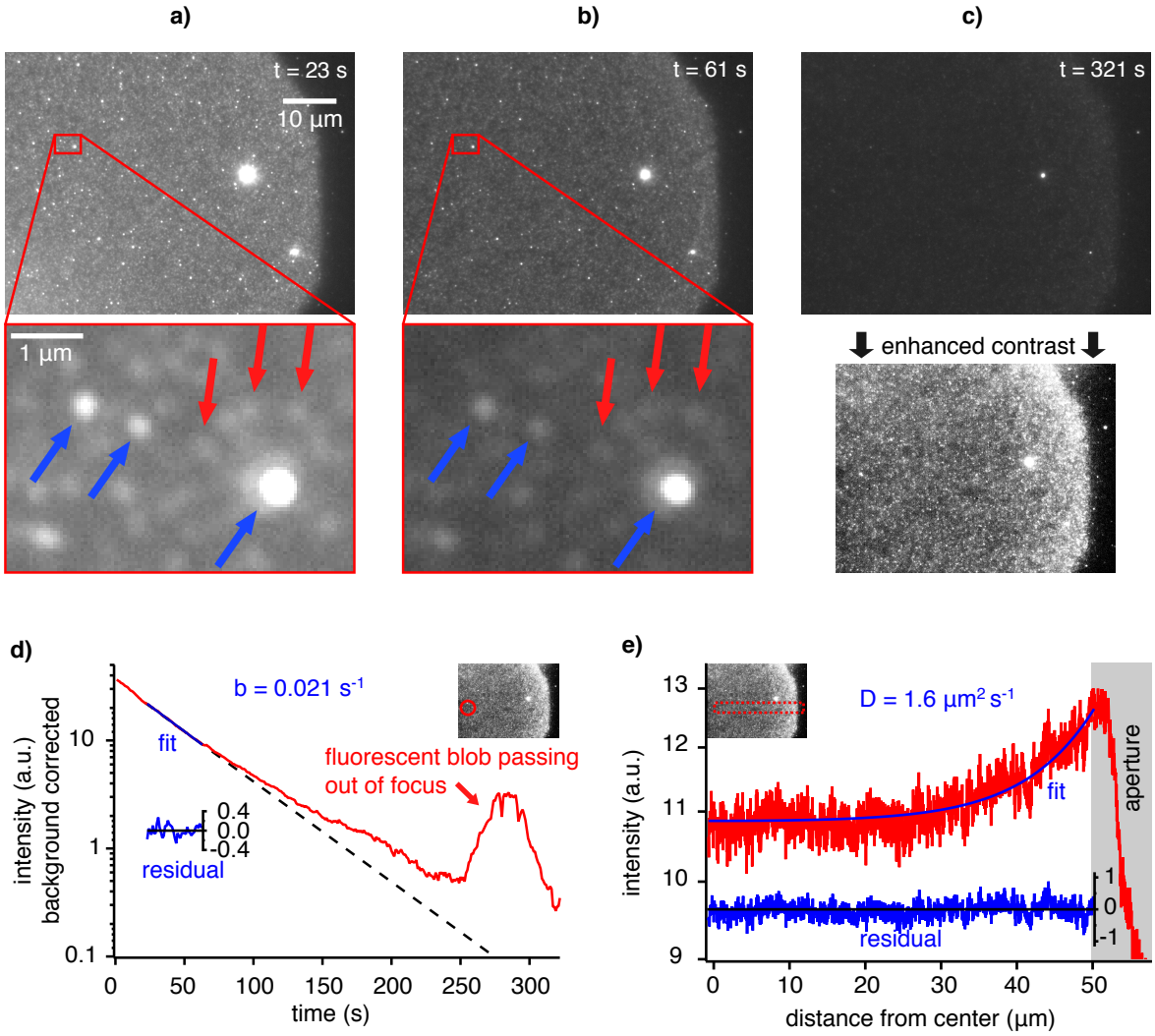

Figure A 1: Continuous bleaching of fluorescently labeled FERM bound to a PIP2 membrane. Figures **a)**, **b)** and **c)** show fluorescence micrographs of fluorescently labeled FERM on a non-fluorescent supported lipid bilayer (5% PI(4,5)P2, 95% DOPC) at different times during a continuous bleaching experiment. Prior to bleaching, FERM was incubated on the bilayer for 70 minutes, and unbound FERM was washed away by buffer exchange. Three different fluorescence populations can be observed: Weak fluorescent spots of similar intensity and highly fluorescent spots are best visible in a) and b) (red and blue arrows, respectively). As the images show, these spots loose fluorescence intensity but do not move over time. The third population, visible by eye as fluorescent wafting mist of homogeneous intensity bleaches over time and forms a fluorescent halo on the edge of the illuminated circular area. It is best observed at the end of the bleaching experiment (**c**). **d)** Fitting the fluorescence intensity decay spatially averaged over a central disk (red circle in the inset) according to equation (A2) yields the bleaching rate *b* of the label. **e)** The halo dominates the cross-sectional intensity profile extracted from c) by vertically averaging over the red rectangle in the inset. The bleaching rate and geometrical constants of the setup given, the halo was fit according to equation A1 and the diffusion constant *D* of the labeled FERM was determined to be 1.6 $\mu m^2 s^{-1}$.

In the conducted force spectroscopy experiments that probed FERM on SLBs containing 5% PI(4,5)P2 a splitting of rupture forces into tow-wormlike chain populations (marked red) is observed in the force-distance distributions displayed in fig. A.2. This can be interpreted as a FERM-specific binding with forces between 15 and 20 pN. The population with higher rupture forces would then correspond to a single FERM experiencing a double interaction with PI(4,5)P2. However, as these forces are at the lower limit of what AFM-based force spectroscopy can resolve, this interpretation must be seen as rather speculative. Additionally, these potential specific interactions are disguised by

several randomly distributed rupture events and by a significant population of short-distanced ruptures occurring at high forces (marked blue in fig. A2). We interpret these phenomena as direct tip-membrane interactions.

Unfortunately, these findings will have to be put further into perspective: In control experiments, we found an unexpected amount of worm-like chain events on SLBs containing only DOPC (see fig. A2) and DOPC with 5% PI(3,4,5)P3 (not shown). This supposes an additional affinity of FERM to DOPC and perhaps also to PIP3.

A quantitative analysis which could differentiate these interactions by characterizing e.g. their loading rate dependence or the interaction probability was hampered by the AFM's resolution and by the strong fluctuation in overall interaction probabilities of the individually functionalized cantilevers.

We did not see dependences on the loading-rates or differences in the experiments when the entire FAK was probed instead of only its FERM-domain.

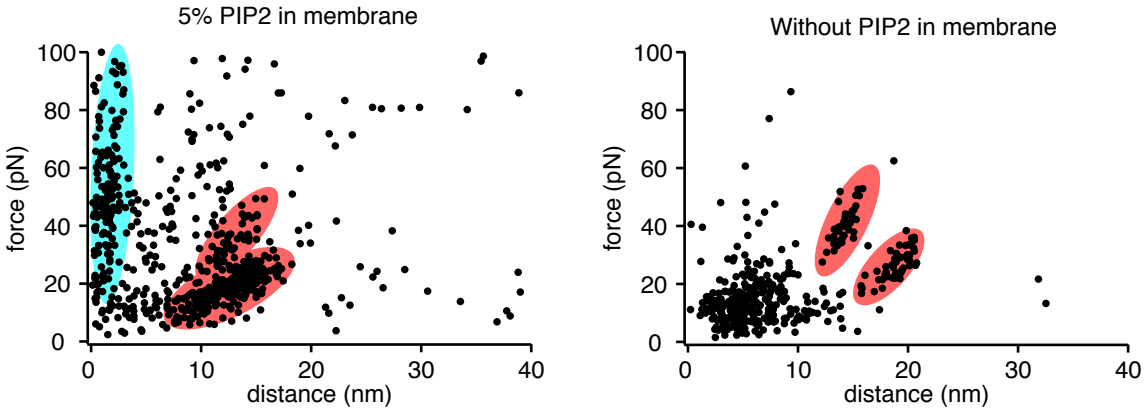

Figure A 2: Force spectroscopy results of FERM on PIP2 membranes. The two diagrams show rupture forces and distances of FERM functionalized cantilevers as they are retracted from supported lipid membranes (DOPC) containing 5% PIP2 (left) and no PIP2 (right). On the PIP2 membrane and the negative control, subpopulations of rupture events (marked with red ellipses) show worm-like chain characteristics as expected from stretching of the 20 nm PEG-linker upon FERM binding. In case of the PIP2 membranes, there exists an additional population of short distance rupture events occurring at high forces (blue ellipse). A multitude of unmarked rupture events cannot be attributed to a characteristic behavior. The overall interaction probabilities were 17% for the PIP2 membranes and 4% for the negative control.

Conclusion and Outlook

Our continuous bleaching experiments lead to the conclusion that FAK has a general affinity to membrane bound PIP2 through its FERM-domain. In this experimental scenario, the affinity was PIP2 specific as it showed a significantly higher strength here than to PIP3 or DOPC. The binding forces of PIP2 and FERM were estimated to 15-20 pN in force spectroscopy experiments.

The fact that we also observed interactions of FERM with PIP3 and DOPC in this latter setup could be explained by a non-linear mechanism raising the quality of the PIP2-FERM bond. One possible mechanism for this could be the PIP2 induced aggregation of FERM. This mechanism was proposed by D. Lietha [A6] and could lead to an increased binding strength in experiments that incubate FERM at high bulk concentrations, as it was the case in the bleaching experiments only. A force spectroscopy experiment with 1µM FERM in

the buffer did not give significant results; however, in this setup bulk FERM might also passivate the PIP2.

In summary, the binding forces of FERM to PIP2 showed to be too low for AFM-based force spectroscopy. An approach employing optical or magnetic tweezers on the system instead, may lead to quantitative results allowing a characterization of the involved affinities.

A setup combining ZMWs and magnetic tweezers generally seems possible, and enzymes at the bottom of a waveguide should be accessible via long enough handles. So, the ultimate goal of investigating the force-activation of FAK-signaling with fluorescence methods remains in reach.

Detailed methods and complete results are reported in the master's thesis of M. Hiermaier [A16].

References

[A1] Krauss, G.: Biochemistry of signal transduction and regulation. Wiley, **2003**.

[A2] Dennis, E. A. and R. A. Bradshaw: Intercellular signaling in development and disease. Academic Press, **2011**.

[A3] Mitra, S. K., D. A. Hanson and D. D. Schlaepfer: Focal adhesion kinase: In command and control of cell motility. Nature Reviews: Molecular Cell Biology, 6(1):56-68, **2005**.

[A4] Lietha, D., X. Cai, D. F. J. Ceccarelli, Y. Li, M. D. Schaller and M. J. Eck: Structural basis for the autoinhibition of focal adhesion kinase. Cell, 129(6):1177-1187, **2007**.

[A5] Wong, V. W., K. C. Rustad, S. Akaishi, M. Sorkin, J. P. Glotzbach, M. Januszyk, E. R. Nelson, K. Levi, J. Paterno and I. N. Vial: Focal adhesion kinase links mechanical force to skin fibrosis via inflammatory signaling. Nature Medicine, 18(1):148-152, **2012**.

[A6] Lietha, D. and F. Graeter, personal communication.

[A7] Puchner, E. M., A. Alexandrovich, A. L. Kho, U. Hensen, L. V. Schäfer, B. Brandmeier, F. Gräter, H. Grubmüller, H. E. Gaub and M. Gautel: Mechanoenzymatics of titin kinase. Proceedings of the National Academy of Sciences, 105(36):13385, **2008**.

[A8] McLean, G. W., N. O. Carragher, E. Avizienyte, J. Evans, V. G. Brunton and M. C. Frame: The role of focal-adhesion kinase in cancer — a new therapeutic opportunity. Nature Reviews Cancer, 5(7):505-515, **2005**.

[A9] Yin, J., A. J. Lin, D. E. Golan and C. T. Walsh: Site-specific protein labeling by sfp phosphopantetheinyl transferase. Nature Protocols, 1(1):280-285, **2006**.

[A10] Wong, L. S., J. Thirlway and J. Micklefield: Direct site-selective covalent protein immobilization catalyzed by a phosphopantetheinyl transferase. Journal of the American Chemical Society, 130(37):12456, **2008**.

[A11] Barenholz, Y., D. Gibbes, B. J. Litman, J. Goll, T. E. Thompson and F. D. Carlson: A simple method for the preparation of homogeneous phospholipid vesicles. Biochemistry, 16(12):2806-2810, **1977**.

[A12] Dietrich, C., R. Merkel and R. Tampé: Diffusion measurement of fluorescence-labeled amphiphilic molecules with a standard fluorescence microscope. Biophysical Journal, 72(4):1701-1710, **1997**.

[A13] Hochrein, M. B., C. Reich, B. Krause, J. O. Rädler and B. Nickel: Structure and mobility of lipid membranes on a thermoplastic substrate. Langmuir, 22(2):538-545, **2006**.

[A14] Horton, M. R., C. Reich, A. P. Gast, J. O. Rädler and B. Nickel: Structure and dynamics of crystalline protein layers bound to supported lipid bilayers. Langmuir, 23(11):6263-6269, **2007**.

[A15] Köchy, T. and T. Bayerl: Lateral diffusion coefficients of phospholipids in spherical bilayers on a solid support measured by 2h-nuclear-magnetic-resonance relaxation. Physical Review E, 47(3):2109-2116, **1993**.

[A16] Hiermaier, M. Investigation of focal adhesion kinase binding to phosphatidylinositol (4,5)-bisphosphate in lipid membranes with force spectroscopy, thesis, Ludwig Maximilians Universität München, Munich, **2012** (unpublished).

Acknowledgements

The reprinted author lists and acknowledgements recognize the individual scientific, technical or financial contributions of all published work. However, this thesis is the result of many more individuals and of contributions not mentioned in scientific journals. So, I would like to express my sincere thanks to everyone who has helped me in the course of my doctoral studies with support, advice and motivation.

In particular, I would like to thank:

- *Prof. Hermann E. Gaub* for his dedication to give young students the unique opportunity to do science in an institution of international reputation and with an infrastructure that offers all the equipment and contacts to the scientific community one could wish for. His expertise, goodwill, patience, encouragement and gut feeling were essential for the outcome of this thesis.

- *Prof. Philip Tinnefeld* for his guidance as second research supervisor, his expertise in single-molecule fluorescence techniques and especially for his personal leadership, motivation and encouragement.

- *Dr. Federico Buersgens, Dr. Guillermo Acuña, Dr. Stefan Stahl, Dr. Mathias Strackharn, Dr. Philip Severin, Dr. Ingo Stein Dr. Elias Puchner, Dr. Leopold Prechtel* and *Dr. Diana Pippig* for good advice, helpful discussions and experimental support at long and late hours.

- *Fabian Baumann, Stefan Schloegl, Andreas Meindl and Mathias Hiermaier* for supporting my research with dedication, patience and motivation as part of their diploma, master's and bachelor's theses.

- *Angelika Kardinal, Philipp Altpeter, Stefan Manus, Christian Holopirek*, *Thomas Nicolaus* and *Jürgen Aust and his team* for their technical advice and support.

- *Prof. Jochen Feldmann, Prof. Alexander Holleitner* and *Prof. Jörg Kotthaus* for providing their clean-room facilities. And *Profs. Zan* and *Klaus Schulten* for their generous hospitality and the impressive insights into their research at the University of Urbana-Champlain.

- *Dr. Marie-Christine Blüm, Marilena Pinto, Dr. Susanne Henning, Birgit Gebauer, Dr. Peter Sonntag* and *Chistoph Hohmann* of CeNS and NIM for their organizational support.

- *Everyone at the Department* for providing a fruitful working atmosphere and taking the time for discussions and mutual assistance, especially *Stefan Funk, Dr. Hubert Krammer, Dr. Dominik Ho, Dr. Matthias Erdmann, Christof Mast, Marcus Otten, Dr. Michael Nash, Dr. Martin Benoit, Andreas Gietl, Phil Holzmeister, Dr. Jan Vogelsang and Dr. Christian Steinhauer.*

Finally, I would like to thank *Sophie Borchmeyer, Dr. Carl Gerster* and especially my parents Brigitte and Dr. Christoph Heucke for their support and motivation.